Title

Investigation of Interfacial Flow Dynamics and Mass Transfer in Multi-String Heat and Mass Exchangers for Desalination and Cooling Applications

Author

Sedighi, Erfan

Publication Date

2023

Peer reviewed|Thesis/dissertation

UNIVERSITY OF CALIFORNIA

Los Angeles

Investigation of Interfacial Flow Dynamics and Mass Transfer in Multi-String Heat and Mass Exchangers for Desalination and Cooling Applications

A dissertation submitted in partial satisfaction of the

requirements for the degree

Doctor of Philosophy in Mechanical Engineering

by

Erfan Sedighi

2023

ABSTRACT OF THE DISSERTATION

Investigation of Interfacial Flow Dynamics and Mass Transfer in Multi-String Heat and Mass Exchangers for Desalination and Cooling Applications

by Erfan Sedighi

Doctor of Philosophy in Mechanical Engineering

University of California, Los Angeles, 2023

Professor Yongho Ju, Chair

The flow of liquid films down thin vertical fibers is of significant interest in various applications, such as fiber coating and string-based heat and mass exchangers. This unique configuration can provide an enhanced high rate of exchange in heat and mass. However, the fluid dynamics and interfacial heat and mass transfer mechanisms of these films are convoluted and depend on several parameters, including wettability, size of the nozzle and the fiber, and stream-wise liquid temperature/concentration change. This dissertation aims to develop a high-efficiency heat and mass exchanger utilizing a unique string-based configuration and presents a comprehensive investigation of the wetting interaction of liquids with nozzles and vertical fibers using experimental, numerical, and theoretical approaches. We conducted a systematic study on the capillary-driven rise of liquids on small cylindrical nozzles and the alteration of flow regimes of liquids flowing on a fiber as a result of stream-wise property change. Our proposed flow regime diagrams incorporate the effects of flow parameters to predict flow behavior under various conditions. We further developed simplified analytical and numerical models to simulate the transient liquid flow on the nozzle and the fiber at significantly lower computational costs. We considered liquids with a wide range of viscosity values in our studies and validated our solutions using extensive experimental and high-fidelity simulation data. Finally, we designed,

constructed, and operated a complete multi-string humidification-dehumidification (HDH) desalination setup, which produced ~60 L of fresh water per day while working at an *RR* and *GOR* of 7.5% and 2.9, respectively. Our exchanger's unique configuration enables high mass exchange rates per device volume, resulting in enhanced exchanger effectiveness, and allows for air circulation at low electrical consumption rates. Additionally, an intermediate bypass air-line reduced the stream-to-stream enthalpy difference, resulting in higher thermal efficiency. During our reliability study, we demonstrated that our system is capable of efficiently processing hypersaline brine streams with concentrations as high as 250 g/L. Given the relatively high thermal efficiency, low maintenance requirements, and low electrical consumption of the multi-string desalination device, these novel devices have demonstrated their potential to reduce the cost of producing fresh water.

The dissertation of Erfan Sedighi is approved.

Andrea Bertozzi

Eric M.V. Hoek

Richard E. Wirz

Yongho Ju, Committee Chair

University of California, Los Angeles

2023

I would like to dedicate this dissertation to my mother, my father, and my sister.

TABLE OF CONTENTS

LIST OF FIGURES

Acknowledgments

I would like to first express my appreciation and gratitude to my advisor, Professor Y. Sungtaek Ju, for his continuous guidance and support throughout my PhD research.

I also would like to thank my committee members, Professor Andrea Bertozzi, Professor Eric Hoek, and Professor Richard Wirz, for their presence in my PhD committee as well as their valuable suggestions and encouragement in the past four years.

Professor Andrea Bertozzi and Professor Hoek both have been great mentors and I sincerely appreciate their support and guidance. I would also like to thank Dr. Hangjie Ji, Dr. Claudia Falcon, Dr. Zezhi Zeng, Dr. Abolfazl Sadeghpour, and Mr. Yiming Liu for their collaboration and valuable insights in the projects that we worked on together.

I am especially thankful to my lab mate, Mr. Danny Ko, for all his support. We both joined the Multiscale Thermal Sciences Laboratory (MTSL) at UCLA almost at the same time and since then, he has been a great friend of mine and always available for help.

Dr. Zezhi Zeng, Dr. Abolfazl Sadeghpour, and Dr. Navid Dehdari Ebrahimi were PhD students in the group when I joined UCLA. They were all very supportive and helped me a lot to get on track and become a better researcher. I wish them all the best. I would like to extend my gratitude to the administrative staff at UCLA-Ms. Marla Cooper, Ms. Amanda Gordillo, Mr. Abel Lebon, Mr. Collin Llewellyn, and Mr. Lance Kono. I would like to thank Mr. Benjamin Tan and Mr. Miguel Lozano for their friendship and their contribution in device fabrication.

Last but not least, I would like to thank my mother, father, and my sister for always being there for me no matter what.

VITA

2011-2015	Bachelor of Science, Mechanical Engineering Shiraz University, Shiraz, Iran
2015-2018	Master of Science, Mechanical Engineering Sharif University of Technology, Tehran, Iran
2019-2023	Graduate Student Researcher/Teaching Assistant Mechanical and Aerospace Engineering Department University of California, Los Angeles

PUBLICATIONS

Sedighi, E., Zeng, Z., Sadeghpour, A., Ji, H., Ju, Y.S. and Bertozzi, A.L., 2021. Capillary-Driven Rise of Well-Wetting Liquid on the Outer Surface of Cylindrical Nozzles. *Langmuir*, *37*(35), pp.10413-10423.

Ji, H., Falcon, C., **Sedighi, E.**, Sadeghpour, A., Ju, Y.S. and Bertozzi, A.L., 2021. Thermally-driven coalescence in thin liquid film flowing down a fibre. *Journal of Fluid Mechanics*, *916*.

Liu, Y., Wang, J., Jung, B., Rao, U., **Sedighi, E.**, Hoek, E.M., Tilton, N., Cath, T.Y., Turchi, C.S., Heeley, M.B. and Ju, Y.S., 2022. Desalinating a real hyper-saline pre-treated produced water via direct-heat vacuum membrane distillation. *Water Research*, *218*, p.118503.

CHAPTER 1

Introduction

1.1 Motivation

Thin liquid films flowing down a vertical fiber subject to thermal and mass exchange effects have been previously studied due to their importance in a variety of industrial applications, including dry and wet cooling systems and heat and mass exchangers for vapor, CO2, and particle capture [1]–[4]. In addition to cooling and particle capturing applications, multi-string based exchangers that use such structure are a suitable candidate for desalinating hypersaline water using Humidification-Dehumidification (HDH) mechanism due to their extremely simple structure and offering high amount of vapor exchange per given volume [1], [4]. A multi-string exchanger for both heat/mass transfer purposes offer several advantages over the existing systems including lightweight and low-price structure, extremely low electricity consumption due to its highly porous structure, low maintenance demand, high thermal/mass exchange effectiveness, etc.

A systematic design approach and implementation is needed to build a highly efficient multi-string exchanger that can be used in desalination and cooling systems to maximize the performance. This includes investigating the effect of nozzle wettability on liquid flow in such devices [5]. Moreover, changes in liquid properties like surface tension and viscosity of thin films flowing on fibers due to the presence of a temperature and/or concentration gradient

influence the characteristics of these flows [6]. An improved understanding of the effect of the liquid property variation along fibers as a matter of heat and mass exchange is crucial for physics-based design and optimization of such heat and mass exchangers. This will eventually result in lowering the costs of desalination and industrial cooling.

1.2 Study of capillary-driven rise of liquids on small nozzles

Well-wetting liquids exiting small-diameter nozzles in the dripping regime can partially rise along the outer nozzle surfaces. This is problematic for fuel injectors and other devices such as direct-contact heat and mass exchangers that incorporate arrays of nozzles to distribute liquids. The associated flows are governed by complex interplay of surface tension, non-uniform pressure distribution within a pendant drop, gravity, and viscous forces. Ambravaneswaran et al. [7], [8] proposed flow regime diagrams that showed the transition between the dripping and jetting regimes as a function of the flow rate and viscosity for a Newtonian liquid. The transition was shown to be delayed at low viscosities where a buffer regime, called the complex dripping regime, occurs before the jetting regime. A later study [9] shows that the previous scaling laws do not apply for very large nozzles and proposes an alternative group of dimensionless numbers to capture flow regime transition in the limit of negligible viscous effects.

At sufficiently low flow rates, for nozzles with wettable outer surfaces, part of the liquid may rise up along the outer surfaces due to capillary effects. This is problematic for injection nozzles in combustion engines where residual fuel on the nozzle outer surface can lead to carbon contamination and increase the pollutant emission[10], [11]. Direct contact heat and mass exchanger devices[12], [13] that utilize liquid beads generated using nozzles are another example. If these nozzles are not sufficiently long, the liquid rising up the nozzle outer surface

may form liquid pools or otherwise interfere with the formation of well-defined liquid beads. An earlier study[14] investigated the capillary rising phenomenon on the outer surface of wettable nozzles using a fixed liquid for a very limited range of nozzle sizes and flow rates. Hence, the effect of liquid properties, nozzle size, and flow characteristics on the rising and their relative importance in this problem was not thoroughly discussed which calls for a more comprehensive study in order to give a better understanding for the physics behind such a complex flow.

We experimentally and numerically investigate the effects of liquid properties and flow parameters on the capillary rise of wetting liquids along the outer surface of a nozzle. The maximum height of the meniscus is reported as a function of the flow rate, nozzle diameter, and liquid viscosity. In the limit of low flow rates, quasi-static models based on the Young-Laplace equation capture the measured temporal variations in the meniscus height and its maximum values. We perform a parametric experimental and numerical simulation study to determine the critical flow rates in terms of the three main dimensionless parameters: the Bond number, the Weber number, and the Ohnesorge number.

Figure 1.1 graphically illustrates three different rising behaviors. The images are from different relative time points with respect to one dripping period, *T*, under each flow condition. The first case (a) is for very low flow rates and shows significant capillary rise. The bottom portion of the liquid meniscus (pendant droplet) is close to and nearly touches the bottom tip of the nozzle during the rising period. For this case, we can describe the liquid shape and temporal evolution of the meniscus height on the nozzle outer surface using static or quasi-static models. The second case (b) is for moderate flow rates where the pendant droplet does not stay pinned to the bottom tip of the nozzle during most of the dripping cycle and becomes elongated with time.

The bottom tip of the nozzle stays fully immersed in the liquid. The third case (c) is for either very high flow rates (*We* > 0.1) or for very viscous liquids (*Oh* > 1 for We as small as 0.001) where the flow is about to transition to jetting and there is no appreciable capillary rise along the nozzle outer surface. Numerical simulation of the Navier-Stokes equations can capture the capillary rise dynamics even under moderate and high flow rates, but it requires significant computational resources and time.

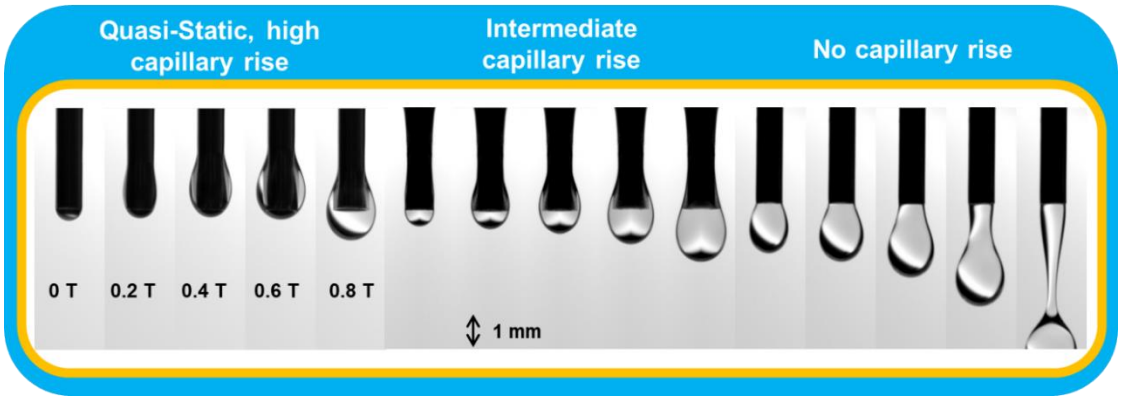

Figure 1.1: The three different capillary rise behaviors of silicone oil v50 on a stainless-steel nozzle under different conditions: a) at low flow rates, b) at moderate flow rates, and c) at high flow rates.

Hence, it is necessary to rigorously study the effect of solid-liquid interaction on the flow dynamics of capillary-driven liquid rise on cylindrical nozzles using experimental, numerical and analytical modeling approaches. This leads to a more efficient and optimized nozzle design in systems using wetting liquids by reducing both the risks of contamination and high pressure drop in such devices.

1.3 Study of the effect of liquid property change on flow dynamics of liquid film flow on thin fibers

It is generally known that when a liquid film with a thickness comparable to that of the fiber is used, liquid beads start to form due to the complex interplay of surface tension, gravitational, inertial, and viscous forces. Several research groups experimentally investigated and analyzed different flow regimes of these liquid beads flowing down a string. In an early study, a set of experiments was run to study the effect of the flow rate on the flow regime [15]. They qualitatively observed three different regimes of the interfacial patterns in the form of traveling liquid beads. At small flow rates, the isolated droplet regime occurs where widely spaced large droplets flow down the fiber separated by secondary small-amplitude wavy patterns. At higher flow rates, the Rayleigh-Plateau (RP) flow regime emerges where a stable train of droplets propagate at a constant speed. If the flow rate increases further, the convective instability regime emerges as collision of large droplets occurs in an irregular fashion. Figure 1.2 shows how these three flow regimes occur when the mass flow rate of silicone oil v50 flowing on a 0.2 mm monofilament changes from 0.006 g/s to 0.02 g/s to 0.1 g/s. Videos regarding the effect of physical parameters on the flow behavior are available at https://youtu.be/h64IAqrkYR8 and https://www.youtube.com/watch?v=ldlRN0CKYPc.

Figure 1.2: Silicone oil v50 flowing on a monofilament with 0.2 mm thickness. The mass flow rate increases from 0.006 g/s to 0.02 g/s to 0.1 g/s from left to right.

More recently, the effect of physical parameters, including liquid properties and the nozzle geometry, on the flow regime have been comprehensively investigated experimentally [16], [17]. The RP to convective flow regime transition can also be triggered by inducing a gradient to physical properties (i.e., surface tension/viscosity) of the liquid film along the fiber [6], [18].

Prior experimental works showed that the RP flow regime offers a higher overall transfer coefficient than the annular film flow on a fiber which proves maintaining a stable train of liquid beads is important for reliable heat and mass transfer performance in many applications [19]–[22]. Although many previous studies have focused on the dynamics of viscous thin films flowing down fibers, the thermal and mass exchange effects on the fiber coating dynamics have received less attention. We numerically, using commercial Navier-Stokes solver, and

experimentally explore the flow dynamics of train beads on fibers under thermal and mass exchange effects to provide more accurate predictions that accounts for the change in liquid properties. We further utilize Orr-Sommerfeld analysis to propose regime transition prediction lines for liquids with intermediate viscosity range such as Calcium Chloride aqueous solutions which are used in our string-based exchanges for dehumidification purposes.

Figure 1.3 shows a schematic of the setup we use to investigate the flow dynamics of the train of beads. Figure 1.4 shows a comparison between two experimental cases and CFD simulations where the train of beads have been captured accurately for both absolute RP regime and at the onset of absolute RP to convective instability induced by thermal effects.

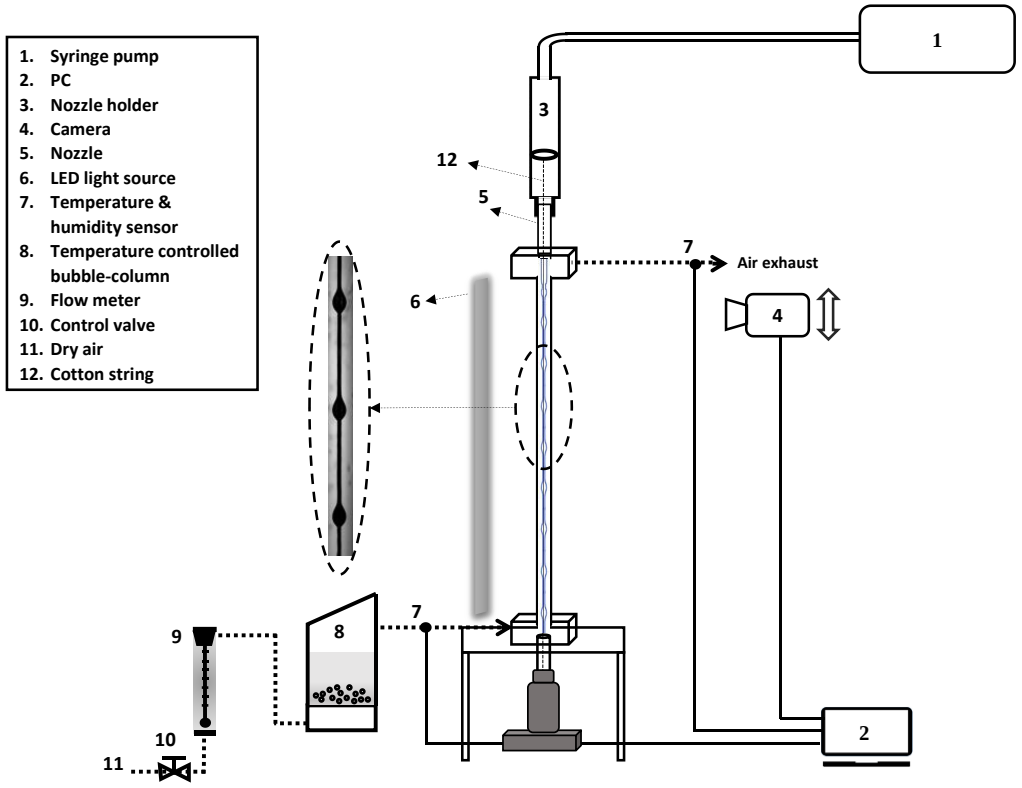

Figure 1.3: Schematic of the experimental setup for investigating the effects of thermal and mass exchange on the flow dynamics of liquid films on thin fibers.

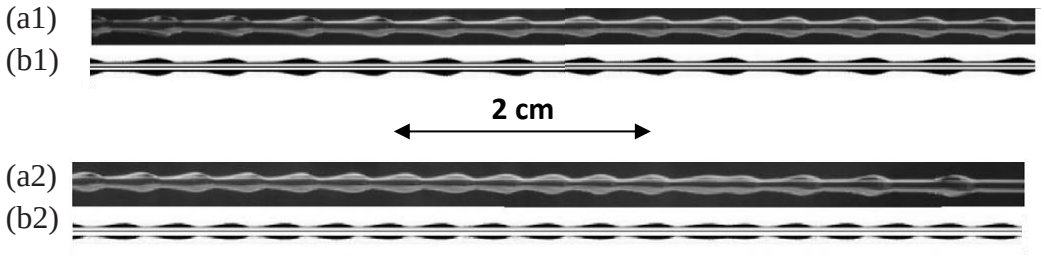

Figure 1.4: Profile comparison between (a) experiment and (b) incompressible Navier–Stokes simulation for the (1) RP flow regime and (2) onset of RP to convective induced by thermal effects for silicone oil v50.

1.4 Humidification-Dehumidification (HDH) desalination using multi-string exchangers

Fresh water is a precious and limited resource. Agriculture, drinking, sanitation, and thermoelectric power plant cooling all require significant amounts of fresh water. However, 97% of water on earth is saline water and not suitable for many of these applications. This has motivated intense research efforts in developing various technologies for desalination and treatments/reuse of industrial and municipal wastewater. The utilization of seawater for drinking purposes, however, is still limited by the high energy cost over production of present desalination technologies. This shows that still a lot of work needs to be done to further enhance the efficiency of desalination systems and make them affordable for a wider range of users.

Desalination systems can generally be divided into three groups: membrane-based systems, thermally driven systems, and desalination systems that use other innovations, e.g., electro-dialysis (ED) or mechanical vapor compression (MVC), for desalinating purposes [23]. The desalination systems that primarily rely on membrane filtration generally consist of, membrane distillation, reverse osmosis, and forward osmosis [1], [24], [25]. Thermally driven systems are mostly based on solar still, solar chimney, humidification-dehumidification (HDH), multi-stage

flash (MSF) evaporation, and multi-effect distillation (MED) [24], [26]–[28]. Reverse osmosis (RO)[29], [30], a membrane-based desalination technique, has been widely used for desalination of sea water, brackish groundwater and treatment of waste-water in large scales and it is considered the leading and the most optimized membrane-based desalination process [31]. Typical RO plants in a multi-stage design provide water recovery of 50%. However, the general performance and efficiency depends on the feed characteristics, feed salinity, pre-treatment, design configuration, and brine disposal considerations [32], [33]. Therefore, high consumption of electricity and increased pre-treatment and membrane maintenance cost due to membrane fouling, and their relatively low limits on the acceptable salinity of feed water are major drawbacks of this kind of desalination systems[30], [31], [34], [35]. In other words, system performance is highly dependent on its filtration parts, and therefore, demands a high degree of maintenance due to membrane fouling and scaling to keep its productivity at a reasonable level.

Thermal desalination techniques such as HDH have become an appealing technology for brine concentration during the past few decades as they are more fit to run with a renewable energy source (i.e., solar energy), can process brine having salinity much greater than seawater, and can be utilized in more compact and portable platforms compared to the desalination systems that are purely relied on membranes. MSF and MED processes are among the most reliable and very well-known thermal desalination techniques. MSF desalination plants, for instance, were being utilized by about 21% of the world's total installed or contracted desalination systems at 2015 [36]. However, MSF process is highly energy-intensive where the energy consumption easily exceeds 20 kWh per meter cubed of produced fresh water [37], [38].

There are performance parameters that are frequently used by researchers to quantify and compare the performance of thermal desalination systems. Here, we introduce two important factors. A parameter most widely used to quantify the performance of thermal desalination systems is the gained output ratio (*GOR*), defined as the ratio between the latent heat of condensation and the net thermal energy input (Eq.1). Where it indicates how much fresh water is being produced per unit heat applied to the system.

$$GOR = \frac{\dot{m}_{pw} h_{fg}}{\dot{Q}_{in}} \qquad (1.1)$$

$\dot{m}_{pw}$ is the rate of purified water production, h_{fg} is the latent heat of vaporization, and $\dot{Q}_{\text{in}}$ is the rate of heat being applied to the device. Another important parameter that is commonly used in the literature is the recovery ratio (*RR*). *RR*, as defined in Eq. (2), is the ratio of the amount of water produced ($\dot{m}_{\text{pw}}$) per kg of brine feed ($\dot{m}_{\text{b,in}}$). In a desalination system working with a closed air loop, once the steady-state condition is reached, evaporation and condensation happen at the same rate, hence *RR* can be calculated using the rate of either evaporation or condensation.

$$RR = \frac{\dot{m}_{pw}}{\dot{m}_{b.in}} \qquad (1.2)$$

Note that, since *GOR* depends on the rate of freshwater production, having a higher *RR* may also result in having higher *GOR*. However, *GOR* also depends on heat recovery and as more heat is recovered from the hot product, less energy (i.e., $\dot{Q}_{in}$) would be needed to run the system at the same water production level.

Humidification and dehumidification (HDH) thermal desalination technique is a better choice for small to medium scale and mobile desalination and water treatment applications [39]–[41] since it can operate under a wide variety of conditions using a low-grade heat source (e.g. a solar panel) and its simple construction needs. An HDH unit mimics our natural water cycle by first humidifying a carrier gas (i.e., air) and then condensing water vapor to produce distilled water (see Figure 1.5). Hence, the HDH system operates with evaporation and condensation cycles that consists of an air stream, being driven via either natural or forced convection, and a water stream [42]. It can be further classified based on the stream that is being heated in the system: air-heated or water-heated. For either heating scenario, four different approaches are available depending on whether each fluid stream is undergoing a closed cycle or an open cycle configuration [23]. Figure 1.5 qualitatively shows how a closed-air open-water (CAOW) water-heated HDH cycle works which have been investigated through many numerical and experimental research. The *RR* is, generally, found to be much lower for the HDH system than conventional systems. This might seem like a drawback for the overall performance of an HDH system. However, using a multi-stage or the so-called "feed-and-bleed" design can solve the problem and *RR* can be further improved until a limit set by the device's salinity tolerance. Another drawback for HDH systems is the need for dehumidifiers with very large surface areas. This is mostly due to the presence of non-condensable gases while working under atmospheric conditions which makes the condensation process less efficient. Hence, designing and utilizing an efficient dehumidifier is crucial for any HDH system to make them more affordable and reduce the final cost of freshwater production.

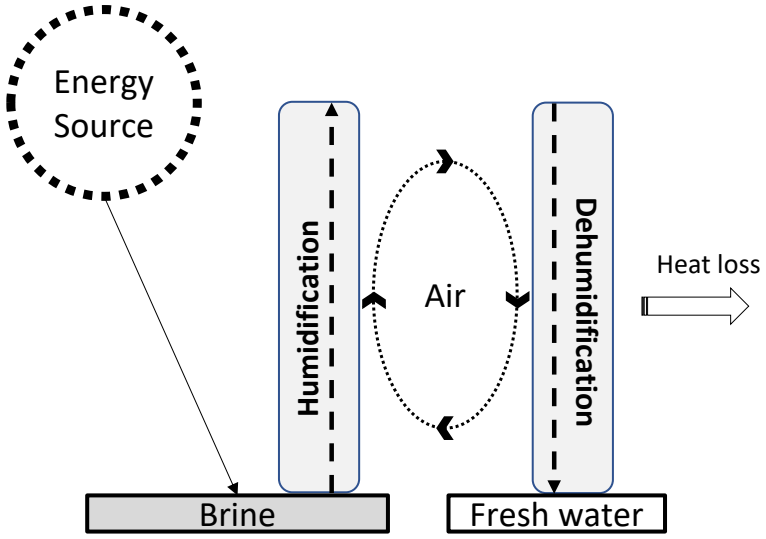

Figure 1.5: Closed-air open-water (CAOW), water-heated, humidification-dehumidification (HDH) inspired by the natural water cycle.

A primary issue with earlier versions of HDH systems is their relatively low effectiveness for dehumidification. Much higher surface areas are needed for condensation to compensate for the low mass transfer rates due to the abundant amount of non-condensable gases under atmospheric conditions [43]. This leads to a more critical challenge with HDH which is its low energy efficiency. To enhance thermal efficiency, past studies [44] proposed mass extractions/injections between a humidifier and a dehumidifier to thermodynamically balance the HDH system and maximize the thermal energy recovery by reducing entropy production. However, even with implementing the proposed scenario on the existing heat/mass exchanger technologies, a previous theoretical study projected that exchangers of very large sizes are still needed to give *GOR* values that are competitive among other highly efficient desalination devices [45].

We combined our understanding of thermodynamics of HDH desalination, heat and mass transfer in multi-string exchangers, and other related physical and practical constraints with an optimization algorithm to design, build, and run a highly efficient thermal desalination system that can reach high values of *GOR* and, at the same time, can tolerate high levels of brine salinity. The design shown in Figure 1.6 qualitatively illustrates the design that we propose after rigorous and comprehensive numerical and experimental studies on a complete HDH desalination system using multi-string exchangers.

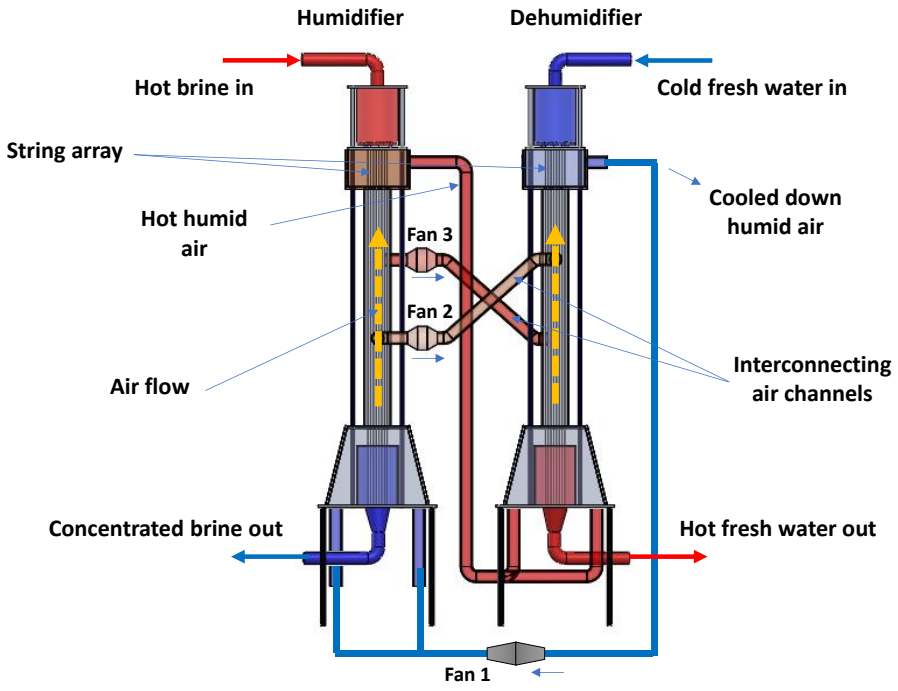

Figure 1.6: Schematic of overall project concept. Dashed lines with arrowheads show the direction of the airflow in the exchangers.

1.5 Objectives of the present study

The present study aims to (i) present a combined analytical, experimental, and numerical study to help identify the critical parameters governing the flow regime and the characteristics of capillary-driven rise of wetting liquids on outer surface of cylindrical nozzles such as nozzle size and liquid properties, (ii) experimentally and numerically, including incompressible Navier-Stokes CFD simulations, study the effect of heat/mass exchange on the flow regime of train of beads flowing down thin fibers, (iii) a first-ever experimental study of incorporating liquid desiccants in string-based exchangers for dehumidifying wet air streams at high dehumidification rates, (iv) conduct a comprehensive thermodynamical and heat transfer analysis on HDH systems and build a systematic numerical design framework that can find optimum working condition for a given HDH desalination system utilizing multi-string exchangers for humidification and dehumidification of the wet air stream, and (v) fully design and construct a complete HDH desalination system prototype for producing fresh water from hypersaline brine feeds at relatively high thermal efficiency and low maintenance level compared to similar existing devices .

1.6 Organization of the thesis

This dissertation studies the interaction of liquids and wettable nozzles and fibers, and applications of liquid flow on thin fibers for water treatment and air conditioning.

Chapter 2 presents a combined analytical, experimental, and numerical study to help identify the critical parameters governing the flow regime and the characteristics of capillary-driven rise of wetting liquids on outer surface of cylindrical nozzles. We perform a systematic experimental investigation by varying the nozzle outer diameter in the range of 0.7 to 3.2 mm. The

experimental results are recorded using a high-speed camera and analyzed to evaluate the characteristics of the capillary-driven flow, such as the meniscus rise with time, meniscus contact angle, and the maximum height the meniscus reaches for each individual case. We limited our study to the dripping regime, where no jetting occurs. To help interpret the experimental results and investigate the possibility of offering analytical solution to the problem, we conduct a set of transient Navier-Stokes CFD simulations by using appropriate geometry, grid structure, and accurate solvers.

Chapter 3 uses a similar approach but this time for investigating dynamics of thin liquid films flowing down on vertical fibers under non-uniform thermal effects. The proposed full lubrication model for numerically modeling the train of beads includes the slip boundary condition, various curvature terms, and a film stabilization term. We analyze the modeling results and compare them to our experimental and CFD simulation data for similar cases to first validate the model and then use it for flow regime predictions. We offer a more rigorous investigation compared to the recent works on the thermal effects on flow dynamics of train of liquid beads.

Chapter 4 conducts investigation on a single-string mass exchanger used for dehumidifying an air stream. We incorporate liquid desiccants (Calcium Chloride aqueous solutions) at different concentrations into the exchanger and study its dehumidification performance. This study also investigates the effect of liquid property change, as a matter of concentration change due to condensation, on the flow dynamics of the liquid desiccant film on cotton threads. We experimentally demonstrate that the flow regime of liquid desiccant can change from absolute RP to convective instability only by absorbing moisture from the wet air stream. We then use Orr-Sommerfeld analysis to give accurate predictions on the transition flow rates for liquids with intermediate viscosity such as $CaCl_2$ aqueous solutions.

Chapter 5 starts with giving a detailed thermodynamics analysis on HDH desalination systems in general. Then a systematic model that incorporates heat and mass transfer equations is built to predict the performance of a given multi-string HDH desalination system under various conditions. We then use those findings to design a desalination system that offers high thermal efficiency values while requiring low maintenance. We then construct a desalination system utilizing multi-string exchangers for both humidification and dehumidification. We perform a series of experimental study to validate our modeling and compare the performance with similar devices in the literature. Recovery Ratio (*RR*) and Gained Output Ratio (*GOR*) are experimentally measured as a function of water-to-air mass flow rate ratio using three different approaches. The effect of inlet brine salinity level and temperature is also studied.

CHAPTER 2

Capillary-Driven Rise of Well-Wetting Liquid on the Outer Surface of Cylindrical Nozzles

Well-wetting liquids exiting small-diameter nozzles in the dripping regime can partially rise up along the outer nozzle surfaces. This is problematic for fuel injectors and other devices such as direct-contact heat and mass exchangers that incorporate arrays of nozzles to distribute liquids. We report our experimental and numerical study of the rising phenomenon for wide ranges of parameters. Our study shows that the interplay of three dimensionless numbers (the Bond number, the Weber number, and the Ohnesorge number) governs the capillary-driven rise dynamics. In general, as the flow rate or the viscosity increases, the capillary-driven rise height over each dripping period becomes smaller. We identify liquid flow rates below which the temporal evolution of the meniscus positions can be well approximated by a quasi-static model based on the Young-Laplace equation. Our analysis reveals two critical Bond numbers that give nozzle sizes which correspond to the maximum meniscus rise and the onset of capillary-driven rise cessation. These critical Bond numbers are characterized as functions of the contact angle, regardless of fluid type. Our study leads to a more efficient and optimized nozzle design in systems using wetting liquids and introduces a more robust approach for surface tension measurement using pendant drop method.

2.1 Background

Liquid dripping from nozzles has been studied extensively in the literature[9], [46]–[50] as it is observed commonly in faucets[7], [51]–[53], and also in such diverse applications as printing[54]–[58], fiber coating[59], [60], microencapsulation[61]–[65], and fuel injection[10], [11]. The associated flows are governed by the complex interplay of surface tension, gravitational, inertial, and viscous forces. However, Eggers describes the slow dripping process as a case where surface tension forces are in balance with gravitational forces and the liquid undergoes a sequence of equilibrium conditions[46].

Some early theoretical and experimental studies examined dripping of highly viscous liquids at low flow rates to minimize the effects of inertia. In one study, breakup of a polymeric liquid filament into droplets was studied using a one-dimensional thin-filament analysis[66]. A viscoelastic liquid was shown to delay satellite droplet formation and maintain the thinnest point on the filament at the midpoint between droplets. In another study, Wilson[67] investigated the dripping of a viscous fluid from a nozzle and modeled the unsteady extension of a viscous thread under its own weight. Wetting of the outer nozzle surface was suggested as one of the major sources of errors in the previous model but no systematic experiments quantifying the phenomenon were reported.

A decade later, Eggers and Dupont[68] developed one-dimensional partial differential equations to describe the shape and internal flow fields of a thin axisymmetric column of a viscous fluid. They investigated the nature of singularities during necking and captured experimentally determined drop profiles close to the break-up point.

Zhang (X.) and Basaran[69] did a comprehensive experimental study, considering finite inertial effects, on droplet formation by examining the effects of both fluid properties and nozzle dimensions on the development, extension, and breakup of a liquid thread, and satellite droplet formation. They practically proved that, for cases where the inner to outer radius ratio is higher than 0.2, the wall thickness shows almost no effect on meniscus evolution and breakup volumes.

Richards et al.[70] conducted a direct numerical simulation study, using a combination of volume of fluid (VOF) and continuous surface force (CSF) methods, on drop formation from a liquid jet at relatively high inertial to viscous forces (Reynolds numbers >250). In the considered system, the liquid jet discharges into a tank that is filled with another immiscible liquid. The main purpose of the study was to relax a number of assumptions used in earlier studies in order to enhance the accuracy with respect to experimental results.

Zhang (D.) and Stone[71] numerically studied drop formation of a highly viscous liquid from capillary tubes in contact with a second immiscible phase. Due to the low contribution of inertial forces in the problem, they solved Stokes equations using boundary integral method to study the formation, extension, droplet breakup, and satellite drop formation. They assumed the droplet always remains pinned at the outer edge of the nozzle and, therefore, the effect of wall thickness was neglected.

Following the two previous works, in 1999 Wilkes et al.[72] experimentally and numerically studied droplet formation of a Newtonian liquid from a capillary tube into an ambient gas phase. Incompressible Navier-Stokes equations were implemented in a 3D (axisymmetric) geometry discretized by an evolving mesh structure that follows the droplet deformation with time. The problem was solved using finite element method and liquid-gas interface linear momentum balance

took care of the surface deformation at each interval. Concurrently, Zhang (X.) [73], [74] developed another 3D numerical model where a fixed mesh was used instead and the problem was solved using finite-difference. The surface, therefore, was tracked following a Eulerian approach by the VOF method. Using the extensive numerical approach used in the 3D cases, both microscopic and macroscopic features of droplet formation and breakup were addressed at the same time. In a more recent study[50], capillary-driven thinning and pinching off during dripping is studied using the same (VOF) method. The numerical method accurately captures large topological deformations during drop formation and necking.

Ambravaneswaran et al. [75] took advantage of the low computational cost of 1D Navier-Stokes equations to simulate the formation of hundreds of droplets into air in the dripping regime. All the cases were at relatively high values of inertial to surface tension forces (Weber number >0.12), where secondary (satellite) droplet formation is suppressed, and various nonlinear responses could arise. The system was observed to show different harmonic behaviors, for instance in terms of thread length at the onset of pinch off, depending on the range of non-dimensional parameters. Effect of hysteresis was also shown to affect the system's non-linear behavior.

A couple years later, Basaran [47] summarized important scaling parameters that knowing them helps produce monodisperse and repeatable droplets at high frequencies which is crucial in applications such as ink-jet printings. The physical parameters involved in dripping problem can be treated in a way such that the set of non-dimensional numbers that govern the dynamics of drop formation constitute of the Ohnesorge number, which captures interactions among the viscous, inertial and capillary forces, the Weber number, which shows the ratio between the inertial force and the capillary force, and the Bond number, which compares the gravitational force with the

surface tension force. The problem gets more complicated, and hence calls for additional non-dimensional parameters, if new physics, such as an electric field, is introduced.

Ambravaneswaran et al. [7], [8] proposed flow regime diagrams that showed the transition between the dripping and jetting regimes as a function of the flow rate and viscosity for a Newtonian liquid. The transition was shown to be delayed at low viscosities where a buffer regime, called the complex dripping regime, occurs before the jetting regime. A later study [9] shows that the previous scaling laws do not apply for very large nozzles and proposes an alternative group of dimensionless numbers to capture flow regime transition in the limit of negligible viscous effects. Some people, alternatively, developed mass-spring models for dripping faucets to explore chaotic dynamics [76].

Other previous studies of dripping phenomena investigated the impact of the inner and outer diameter, tip geometry, and wettability on the dynamics of droplet formation [77], [78]. These studies found that, for relatively large inner nozzle sizes, since the contact line pins at the inner diameter, the dripping dynamics is generally independent of the geometry (or shape) and dimension of the tip. Hence the dynamics is predominantly affected by drop contact line (i.e. the inner diameter) and the flow rate.

Droplet formation has also shown its important role in measuring liquids' properties such as surface tension using pendant drop method [79] and drop weight method [80]. Requiring a vanishingly small flow rate and the need for drop profile extractions are major drawbacks of the current pendant drop method. Likewise, studies have shown that the drop weight method can also become challenging since effects of flow rate and viscosity need to be carefully taken into account to reduce the measurement errors [80].

While exhaustive amount of work has been done in the past on droplet formation from capillary tubes, the three-phase contact line has been held fixed and the interaction between a wetting liquid and the outer surface of the nozzles, unlike its importance in certain applications, has surprisingly received minimal attention. At sufficiently low flow rates, for nozzles with wettable outer surfaces, part of the liquid may rise up along the outer surfaces due to capillary effects. This is problematic for injection nozzles in combustion engines where residual fuel on the nozzle outer surface can lead to carbon contamination and increase the pollutant emission [10], [11]. Direct contact heat and mass exchanger devices [12], [13] that utilize liquid beads generated using nozzles are another example. If these nozzles are not sufficiently long, the liquid rising up the nozzle outer surface may form liquid pools or otherwise interfere with the formation of well-defined liquid beads. An earlier study [14] investigated the capillary-driven rising phenomenon on the outer surface of wettable nozzles using a fixed liquid for a very limited range of nozzle sizes and flow rates. Hence, the effect of liquid properties, nozzle size, and flow characteristics on the rising and their relative importance in this problem was not thoroughly discussed which calls for a more comprehensive study in order to give a better understanding for the physics behind such a complex flow. Here, although we indeed experience some well-known droplet formation phenomena such as liquid filament breakups and satellite droplet formations, we are exclusively interested in the capillary-driven rising on the outer surface of wettable nozzles while a droplet is forming. Furthermore, our study can be applied for a new, very simple but highly precise, way to measure the liquid surface tension within the context of pendant drop method. Where droplet profile recording is no longer needed and high enough flow rates is used to overcome the problem with liquid evaporation.

In the following discussion, we first begin with presenting the physics governing the dripping and capillary-driven rising and the sets of equations to numerically solve the transient problem for a 3D (axisymmetric) general case. Then we introduce the experimental setup used in the present study to complete the data needed for fully analyzing the capillary-driven rising problem. The meniscus height is reported as a function of the flow rate, nozzle diameter, and liquid viscosity. In the final discussions, we introduce analytical modeling, based on Young-Laplace equation, which we use to predict the capillary-driven rising evolution and its maximum values. Critical flow rates limiting meniscus rise are also defined in terms of the three main dimensionless parameters: the Bond number, the Weber number, and the Ohnesorge number. Finally, taking advantage of the new physics explored here, an alternative approach to the existing pendant drop method for surface tension measurement is discussed.

2.2 Governing equations numerical simulation

We solve the transient problem for an incompressible Newtonian liquid discharging at a given constant rate (Q) from a cylindrical capillary nozzle with an outer diameter of D into the quiescent ambient air. The nozzle tip is modeled as rounded with a radius of curvature half the wall thickness. The axis of symmetry is coincident with the nozzle axis, along the direction of gravity. Both liquid and air properties are constant with time and uniform throughout the domain. A cylindrical coordinate system (shown in Fig. 2.1) defines the physical space.

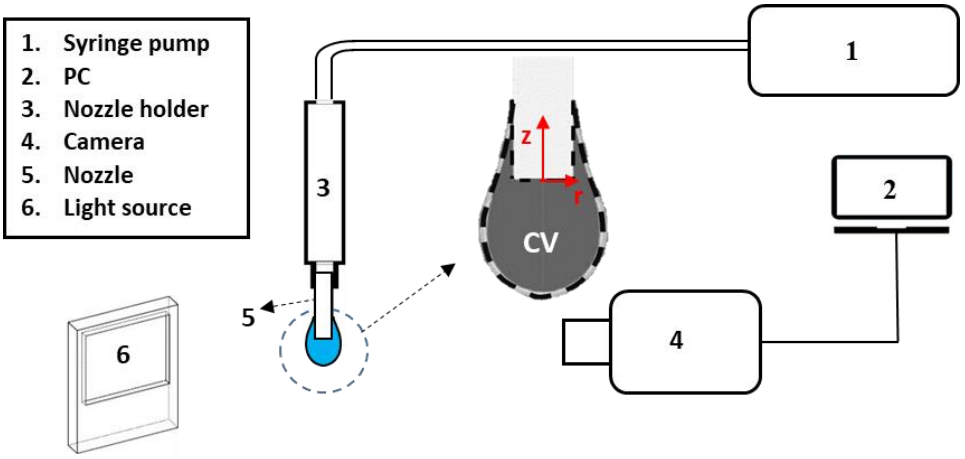

Figure 2.1: Schematic of the experimental setup. Also shown are the coordinate system and the control volume used for later (quasi-static) analyses.

Following Zhang's work[73], the system of Navier-Stokes equations governing the dripping problem are

$$\boldsymbol{\nabla} \cdot \mathbf{v} = 0, \qquad (2.1)$$

$$\frac{\partial \mathbf{v}}{\partial t} + \boldsymbol{\nabla} \cdot (\mathbf{v}\,\mathbf{v}) = -\frac{1}{\rho}\boldsymbol{\nabla} p + \frac{1}{\rho}\boldsymbol{\nabla} \cdot \boldsymbol{\tau} + \boldsymbol{g} + \frac{1}{\rho}\boldsymbol{F_b}, \qquad (2.2)$$

where $\boldsymbol{\nabla}$ is the gradient operator, $\mathbf{v}$ is velocity vector, t is time, ρ is density, p is pressure, $\boldsymbol{\tau}$ is stress tensor, and $\boldsymbol{F_b}$ represents the body forces. We use SIMPLE[81], [82] (semi-implicit method for pressure linked equations) algorithm to handle the pressure-velocity coupling and the second-order upwind scheme to discretize the momentum equations. The solver[83] follows finite volume formulation to extract velocity and pressure fields at each interval.

Further, we adopt the CSF model proposed by Brackbill et al.[84] where the effect of surface tension is introduced as an auxiliary body force in the momentum equations and the pressure staggering scheme (PRESTO) calculates the pressure on the faces (rather than the nodes). The

wettability of nozzle wall is applied by defining liquid-solid contact angle as a boundary condition. Note that, however, the defined contact angle is for a stationary case. When a non-zero velocity field exists, the contact angle changes following the layout of the pressure field close to the contact line. Previous works on nozzle dripping problem assumed a pinned three-phase contact line, either at the inner or outer nozzle edge, where no contact angle was needed to be specified. The VOF method is used to track the liquid-air interface on a stationary Eulerian mesh[73].

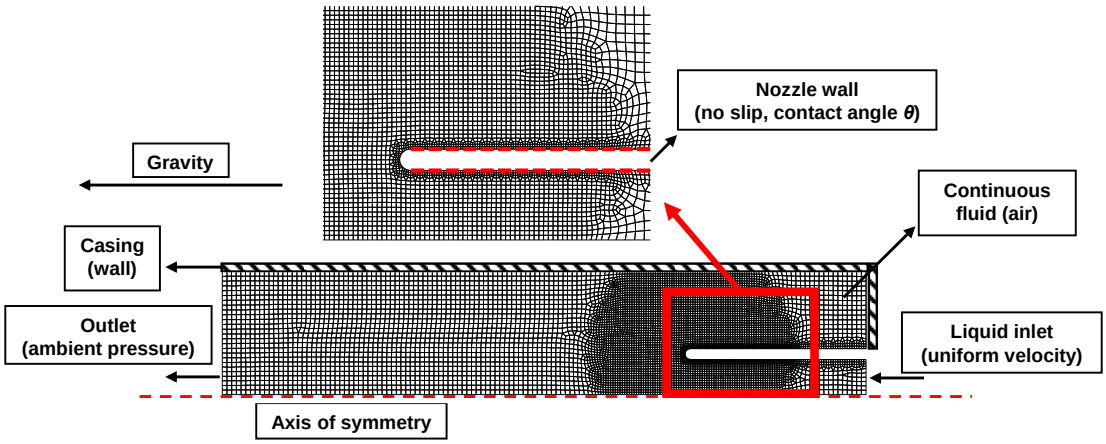

Figure 2.2: Numerical simulation domain and boundary conditions.

We use an unstructured quadrilateral mesh of approximately 7500 elements with a time step size of 20 μs in our simulations. We conduct a mesh-independence and time step-independence study to verify that reducing the mesh size or time step by a factor of two results in less than 5% change in the predicted maximum meniscus heights. To help capture the contact line, we locally refine the mesh near the nozzle wall (Fig. 2). The simulation time is long enough to cover at least three dripping periods, to accurately capture steady periodic behavior (Fig. 2.3). The results presented in the manuscript are from the third dripping period of each simulation.

We use three main dimensionless numbers to characterize the capillary-driven rise behavior. The Ohnesorge number ($Oh = \mu/(\rho\sigma D/2)^{1/2}$) captures interactions among the viscous, inertial and capillary forces, the Weber number ($We = 8\rho Q^2/(\sigma\pi^2 D^3)$) shows the ratio between the inertial force and the capillary force, and the Bond number ($Bo = D(g\Delta\rho/\sigma)^{1/2}$) compares the gravitational force with the surface tension force. Here, the viscosity is μ, the surface tension σ, and the gravity g. We also denote to the meniscus height by h in our hereafter discussions.

We conduct numerical simulations primarily considering Silicone oil as the working fluid. Due to excessive computational time necessary for liquids with very small and very large viscosity, the simulations are reported for an intermediate range of viscosities (silicone oils v20, v50, and v100). We, however, run additional simulations using fictitious liquids to verify the proposed flow regime presented in later discussions. Hence, considering the range of nozzle sizes (0.5 mm $< D <$ 3.2 mm), liquid flow rates (0.2 μL/s $< Q <$ 300 μL/s), densities (440 kg/m^3 $< \rho <$ 950 kg/m^3), surface tensions (18.7 mN/m $< \sigma <$ 45 mN/m), and viscosities (1.75 mPa.s $< \mu <$ 970 mPa.s), the combined numerical and experimental study in present work is for 0.33 $< Bo <$ 1.05, $10^{-7} < We <$ 10, and 0.01 $< Oh <$ 10.

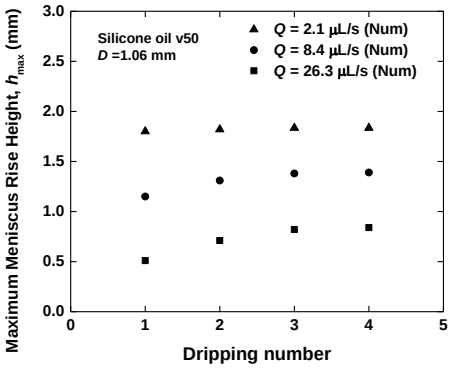

Figure 2.3: Change in the maximum meniscus height (h_{max}) of silicon oil v50 coming out of a 1.06 mm nozzle as a function of dripping number for three different flow rates.

2.3 Experimental setup

Figure 2.1 shows a schematic of the experimental setup. A syringe pump (KDS-410, KD Scientific) is used to pump liquid through a nozzle at a prescribed flow rate. We use stainless steel nozzles with outer diameters D ranging from 0.7 to 3.2 mm. A set of two X–Y stages aligns the nozzle and ensures its verticality. Silicone oils of different viscosities and gasoline (Chevron 87 Octane) are used as the liquids. The liquid volume flow rate Q varies from 0.2 to 300 μL/s at a precision of 0.01 μL/s. The liquid is collected and weighed using precision scale to verify the applied flow rates. The properties of the liquids at 25˚ C are listed in Table 2.1 [85], [86].

A high-speed camera (VR-Phantom, AMETEK) mounted on an X–Y stage captures liquid droplets and the motion of a meniscus at 1000 frames/s. A light source and a light diffuser are used to improve image contrast. The uncertainty in the rising heights and the contact angle are estimated to be ±0.03 mm and ±0.4°, respectively. The videos are analyzed using ImageJ[87] to extract the droplet shapes, meniscus positions, and contact angles. The meniscus height (h) is defined as the distance between the bottom tip of the nozzle and the three-phase contact line on the outer nozzle surface.

Each experimental case resumes for 5 minutes to ensure the system is operating well beyond its transient state. Moreover, three consecutive drippings are recorded for each case. The results show no appreciable difference in the meniscus rise between periods.

Table 2.1: Physical properties of the liquids used in the experiments at 25˚ C.

Liquid	Density (kg/m^3)	Dynamic viscosity (mPa s)	Kinematic viscosity (10^{-6} m^2/s)	Surface tension (mN/m)
silicone v2	873	1.75	2	18.7
silicone v5	918	4.59	5	19.7
silicone v10	935	9.35	10	20.1
silicone v20	950	19.0	20	20.6
silicone v50	960	48.0	50	20.7
silicone v100	965	96.5	100	20.9
silicone v350	968	338.8	350	21.0
silicone v500	970	485	500	21.1
silicone v1000	970	970	1000	21.1
gasoline	718	———	———	21.2

2.4 Results and discussion

2.4.1 Meniscus rise and fall

Figure 2.4 shows one representative set of experimental, and simulation results over one dripping period. The predicted liquid shapes agree reasonably well with the experimental results (Fig. 2.4a). We note that the bottom part of the nozzle remains wetted by the liquid throughout the dripping process. Figure 2.4b shows the temporal evolution of the meniscus rise height on the nozzle outer surface. The meniscus rises rapidly until it reaches a near plateau around the maximum meniscus height, h_{max}. The meniscus then falls as the pendant portion of the droplet elongates substantially until it is detached from the nozzle. Dripping periods for a range of different flow rates are also compared between experimental and numerical cases where the discrepancy is appeared to be less than 3% (Figure 2.5).

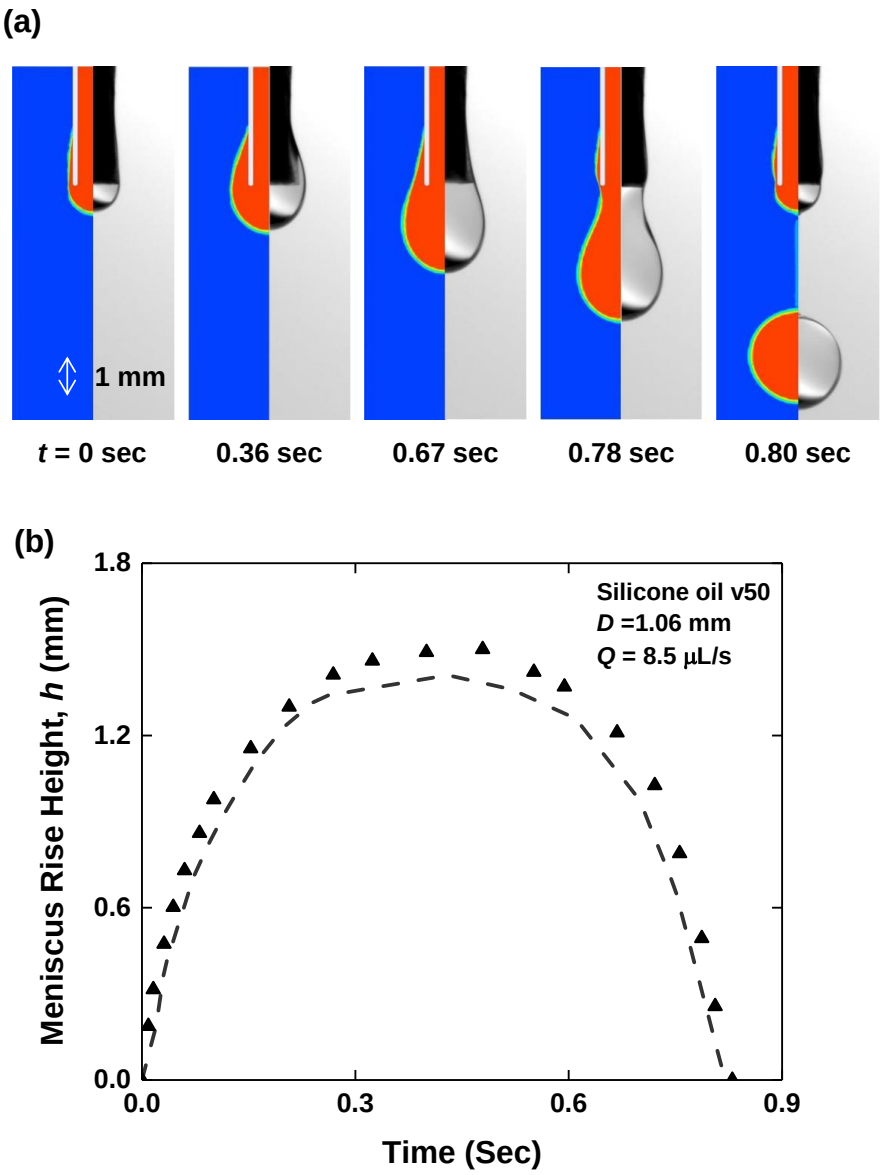

Figure 2.4: (a) Temporal evolution of a silicone oil v50 droplet exiting from a 1.06 mm outer diameter nozzle at Q = 8.5 µL/s. The images in grayscale show experimental results (right), and the images in color show numerical simulation results (left). (b) Temporal evolution of the meniscus rise height for the case shown in (a). The symbols correspond to the experimental results, and the dashed line shows the numerical simulation results. The uncertainties are smaller than the plotted symbols.

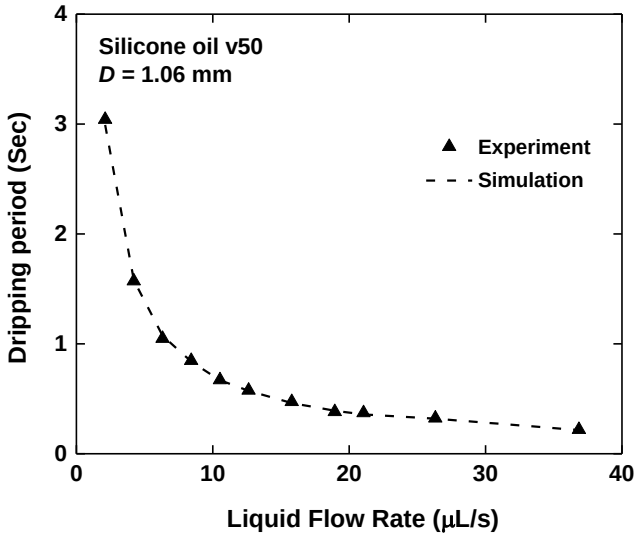

Figure 2.5: Dripping period as a function of flowrate from simulations and experiments for silicone oil v50 and 1.06 mm outer diameter nozzle.

Figure 2.6(a) shows h_{max} for a nozzle with outer diameter D = 1.06 mm. h_{max} decreases with increasing volume flow rates and liquid viscosities. The predictions from our numerical simulation are shown as the hollow symbols and they agree with the experimental data to within 15%. For the silicone oil with the highest viscosity (v1000), h_{max} approaches zero even at moderate flow rates. However, the viscosity has a smaller effect on h_{max} as the flow rate approaches zero. We refer to this zero-flow rate limit of h_{max} as the limiting meniscus height, or h_{max}^0.

Figure 2.6(b) shows that, under conditions examined in the present study, at low and intermediate flow rates, h_{max} generally increases with decreasing nozzle diameters. This is consistent with smaller gravitation force relative to surface tension force for liquid menisci rising along smaller nozzles. At very low flow rates, however, decreasing nozzle diameters can lead to smaller limiting meniscus heights, h_{max}^0. Further discussion of how the nozzle outer diameter and the liquid properties affect h_{max}^0 is provided in a later section. Moreover, since inertia becomes

dominant earlier for cases using smaller nozzles, h_{max} decreases more rapidly with flow rate as the nozzle diameter decreases which eventually might result in smaller h_{max} at high flow rates for smaller nozzles.

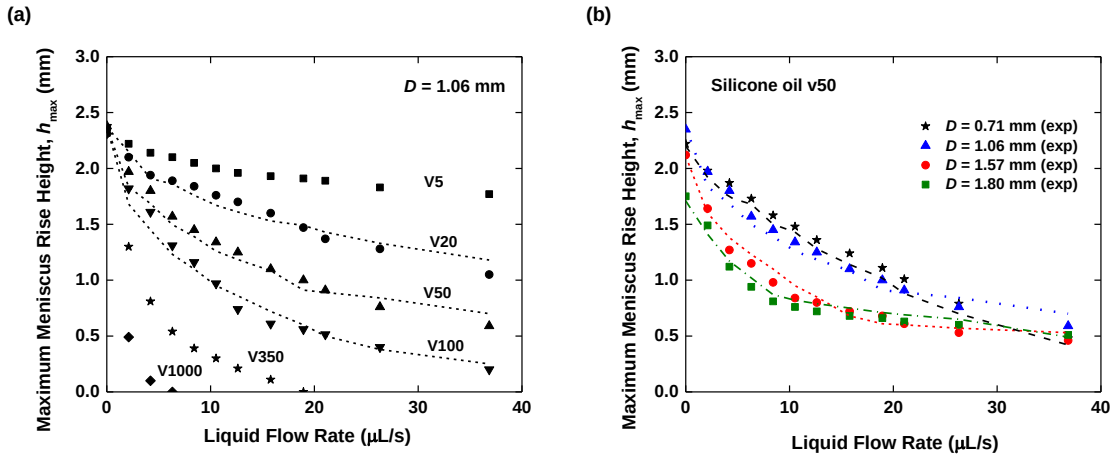

Figure 2.6: Maximum meniscus height h_{max} as a function of the volume flow rate for (a) silicone oils with different viscosities and a fixed nozzle outer diameter (D = 1.06 mm) and (b) different nozzle diameters for a given liquid (silicone oil v50). The dashed lines show the results obtained from numerical simulation of the Navier-Stokes equations for the liquids with intermediate viscosities (v20, v50, and v100).

Figure 2.7 graphically illustrates three different rising behaviors. The images are from different relative time points with respect to one dripping period, T, under each flow condition. The first case (a) is for very low flow rates and shows significant capillary-driven rise. The bottom portion of the liquid meniscus (pendant droplet) is close to and nearly touches the bottom tip of the nozzle during the rising period. For this case, we can describe the liquid shape and temporal evolution of the meniscus height on the nozzle outer surface using static or quasi-static models. The second case (b) is for moderate flow rates where the pendant droplet does not stay pinned to the bottom tip of the nozzle during most of the dripping cycle and becomes elongated with time. The bottom tip of the nozzle stays fully immersed in the liquid. The third case (c) is for either very high flow rates (We > 0.1) or for very viscous liquids (Oh > 1 for We as small as

0.001) where the flow is about to transition to jetting and there is no appreciable capillary-driven rise along the nozzle outer surface. Numerical simulation of the incompressible Navier-Stokes equations can capture the capillary-driven rise dynamics even under moderate and high flow rates (Figs. 2.5 and 2.6), but it requires significant computational resources and time.

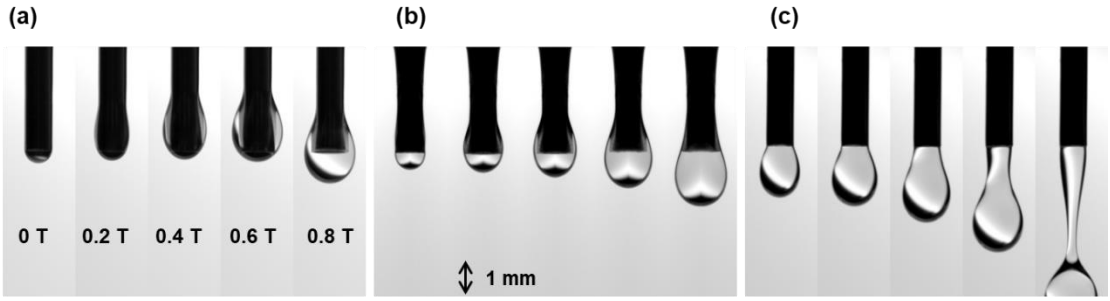

Figure 2.7: The three different capillary-driven rise behaviors under different conditions: a) at low flow rates with significant meniscus rise (silicone oil v50, Q = 0.2 μL/s), b) at moderate flow rates with moderate capillary-driven rise (silicone oil v50, Q = 8.5 μL/s), and c) at high flow rates or highly viscous liquids with no appreciable capillary-driven rise (silicone oil v100, Q = 61.5 μL/s).

2.4.2 Quasi-static models for capillary-driven rise

In the subsequent sections, we develop simplified models under quasi-static conditions and establish conditions for the validity of these models in terms of the three dimensionless numbers.

2.4.3 Static model for the limiting meniscus height, h_{max}^0

We first consider the zero-flow rate limit of h_{max}, or the limiting meniscus height h_{max}^0. We solve the Young-Laplace equation following an approach similar to one adopted in the pendant drop method for measuring surface tension [88], [89]. To establish that this static model is a good approximation for low flow rates used in our experiments, we show in Figure 2.8 our numerical simulation results for a very low flow rate of 0.2 μL/s. The nozzle outer diameter is

1.06 mm, and the liquid is silicone oil v50. Figure 2.8(a) shows that the predicted pressure variation along the centerline of the droplet match the hydrostatic distribution reasonably well. The pressure at z = 0 is obtained from the radii of curvature of the droplet bottom and the surface tension. Figure 2.8 (b) shows the pressure variation at three heights (z = 0.5, 0.9, and 1.5 mm). There is less than 6% change across the nozzle wall.

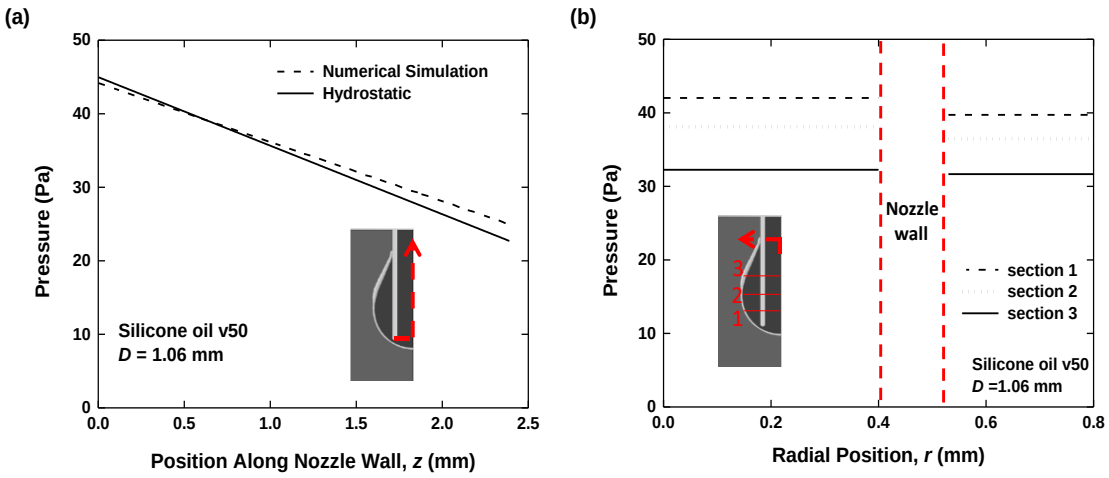

Figure 2.8: (a) Pressure variation along the centerline of a pendant droplet when the meniscus is at the highest point during a dripping process with a very low flow rate of 0.2 μL/s. (b) Pressure variation inside the droplet at three different heights (z = 0.5, 0.9, and 1.5 mm).

Equation (2.3) shows the Young-Laplace equation we solve in a parametric form:

$$\frac{d\varphi}{ds} = -\frac{sin\varphi}{r} + \frac{\triangle \rho g z}{\sigma} + C, \qquad (2.3a)$$

$$\frac{dr}{ds} = cos\varphi, \quad (2.3b)$$

$$\frac{dz}{ds} = sin\varphi. \quad (2.3c)$$

Here, C is a parameter that correlates with the excess pressure inside the liquid (pressure at the bottom of the droplet) and is determined as part of the solution process for the boundary value problem. r and z are the spatial coordinates (see Fig. 2.9a), φ is the angle between the tangent

line at the meniscus and the r axis, and s is the curvilinear variable ($ds = (dr^2 + dz^2)^{1/2}$). The boundary conditions are:

$$r\,(z = z_{bottom}) = 0, \qquad (2.4a)$$

$$r\,(z = h_{max}) = D/2, \qquad (2.4b)$$

$$r\,(z = 0) = D/2, \qquad (2.4c)$$

$$\varphi\,(z = h_{max}) = \pi/2 + \theta. \qquad (2.4d)$$

The third boundary condition corresponds to our approximation that the liquid meniscus touches the bottom tip of the nozzle. Here, θ is the contact angle, which is about 15 degree for the silicone oils and 10 degree for the gasoline used in our experiments. Data reported from earlier studies on contact angle between silicone oils and stainless steel surfaces at very low capillary numbers is consistent with our measurements[90]. Note that the nozzle inner diameter does not play a role because the liquid droplet always hangs from the outer surface of the nozzle.

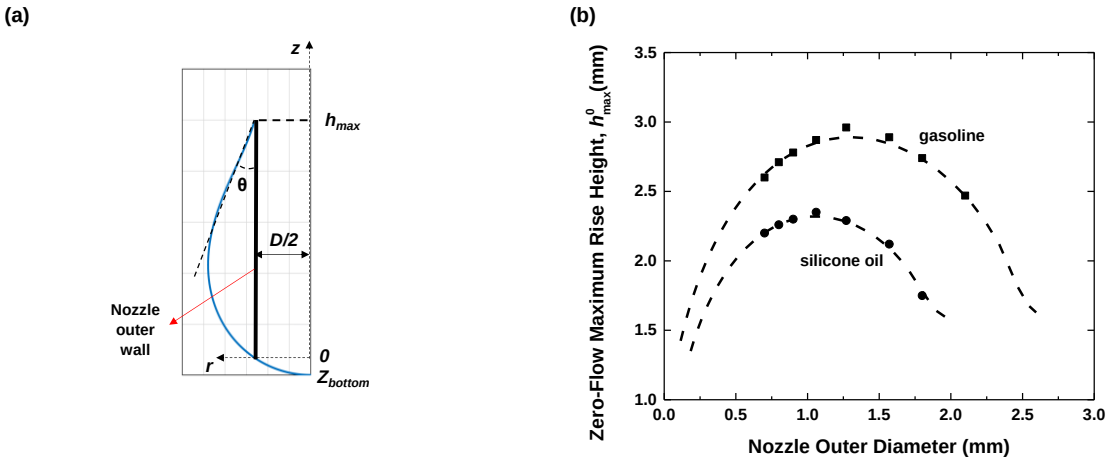

Figure 2.9: (a) A static droplet hanging from a wettable nozzle. (b) The zero-flow rate limit of the maximum meniscus height h_{max}^0 as a function of the nozzle outer diameter for two different liquids, silicone oil and gasoline. The experimentally measured contact angles are used for the predictions, $\theta = 15^\circ$ for silicone oil and $\theta = 10^\circ$ for gasoline. The symbols show our experimental data and the dashed lines show the results from the Young-Laplace equation.

Figure 2.9b compares the values of h_{max}^0 predicted using the Young-Laplace equation (dashed lines) with our experimental results (solid lines with symbols). The two results agree to within 5%. As the nozzle outer diameter D increases, so does the capillary force, which scales as D. As a result, h_{max}^0 first increases with D. This is consistent with the case of a static meniscus that forms on the outside of a cylinder in contact with a pool of liquid[91]. Once the nozzle outer diameter exceeds a certain value, however, the gravitational force, which scales approximately as D^3 and is balancing with the capillary force, hinders the hanging droplet from growing appreciably with respect to the nozzle size. Hence, further increase in D results in decrease in h_{max}^0. There is a nozzle outer diameter for which h_{max}^0 reaches a peak value for a given fluid and contact angle.

Figure 2.9b also suggests that there is no capillary-driven rise of the liquid meniscus when the nozzle outer diameter exceeds a threshold value for each liquid (and contact angle). This limit again is a result of competition between the gravitational force and the surface tension force and can be characterized using the Bond number. For example, the gasoline has almost the same surface tension as the silicone oil but its density is smaller. As a result, it can produce bigger droplets and it can climb up nozzles with larger outer diameters.

Following similar procedure, we show in Figure 10(a) results obtained for a wide variety of fictitious liquids that have different values of $\rho g/\sigma$ but the same contact angle of 15 degree. Figure 10(b) shows that for all these different liquids, the Bond numbers corresponding to the maximum nozzle diameter for capillary rise are essentially the same. The Bond numbers where the peaks in h_{max}^0 occur are also constant. Note that nozzle diameter (D) is used as the length scale in computing Bond numbers throughout the present work.

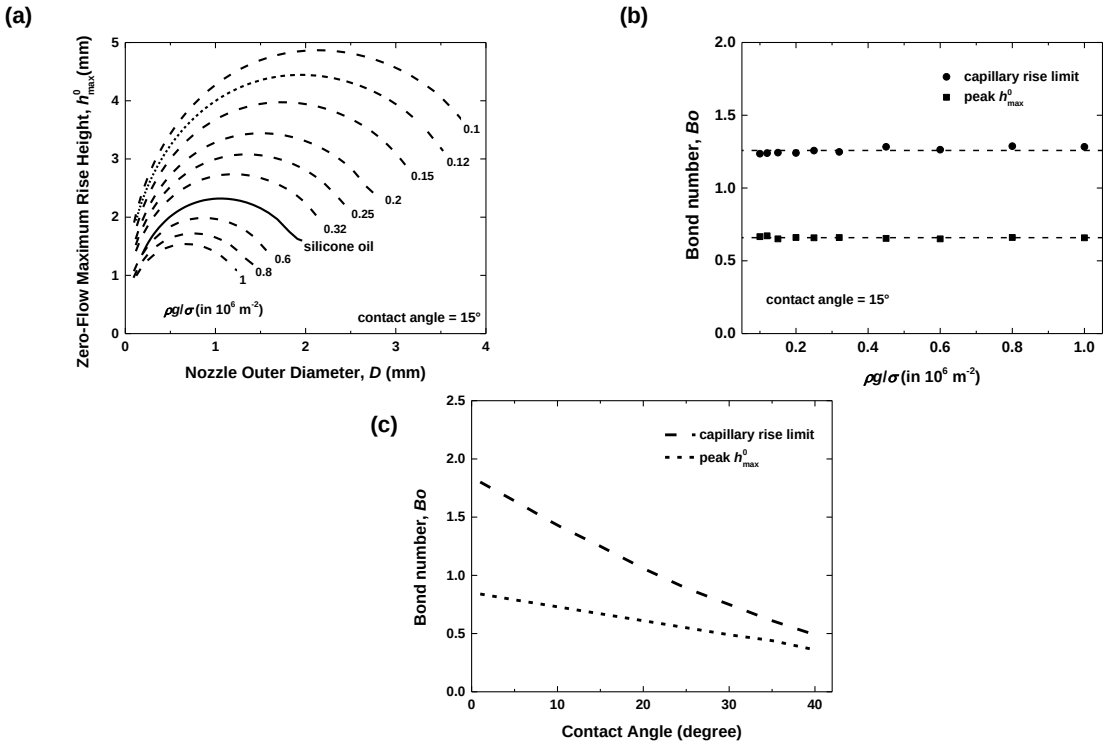

Figure 2.10: (a) Using the same method in Figure 7b, the zero-flow rate limit of the maximum meniscus height h_{max}^0 as a function of the nozzle outer diameter for a wide variety of liquids. (b) The Bond numbers corresponding to the maximum nozzle diameter for capillary-driven rise (circles) and the Bond numbers corresponding to the peak in h_{max}^0 (squares). Dashed lines show the averaged values. (c) The two critical Bond numbers predicted as a function of the contact angle.

We repeat the same analysis for different contact angles and observe the same trend. Figure 10c shows how the two critical Bond numbers change with the contact angle. As the contact angle increases, the two critical Bond numbers decrease and approach each other.

2.4.4 Quasi-Static model for temporal variation in the meniscus height, *h*

We next extend the (near) static model from the previous section to describe the time evolution of the meniscus height on the outer surface of a nozzle at small but finite flow rates. The conditions we consider are relevant for the capillary-driven rise of a working fluid for direct contact heat and mass exchangers. At low flow rates, we observe that the meniscus of the pendant droplet stays very close to the nozzle bottom tip (Fig. 2.7a). This suggests that most of the liquid exiting the nozzle is redirected to support the capillary-driven rise along the outer wall of the nozzle. At finite flow rates, the non-uniform pressure distribution within the pendant droplet may not be accurately described by the hydrostatic distribution. But the pressure along the nozzle outer wall may still follow a nearly hydrostatic distribution at sufficiently low flow rates (Fig. 2.11).

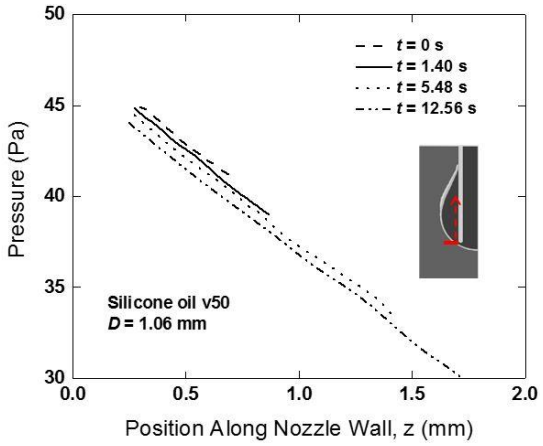

Figure 2.11: Pressure variation with time along the nozzle outer wall during meniscus rise at a very low flow rate of 0.2 μL/s.

Our quasi-static model approximates the portion of the liquid on the nozzle outer wall as a continuous set of static liquid beads on a cylinder. We further assume that all the liquid exiting the nozzle is redirected to the side and therefore the rate of increase in the bead volume is set

equal to the liquid flow rate. For each liquid bead, we solve the same Young-Laplace equation (Eq.(2.3)) as in the previous section. But we exclude the pendant droplet portion of the liquid and solve for $0 < z < h_{max}$. The boundary conditions are

$$r\,(z = h_{max}) = D/2, \tag{2.5a}$$

$$r\,(z = 0) = D/2, \tag{2.5b}$$

$$\varphi\,(z = h_{max}) = \pi/2 + \theta. \tag{2.5c}$$

The parameter C in Eq. (2.3) is set at each time step such that the bead volume matches the pre-scribed value based on the fixed volume flow rate. Figure 2.12a shows reasonable agreement between the predicted meniscus profiles and the experimental results for a representative low-flow rate case (Q = 0.5 mL/s, D = 1.06 mm, silicone oil v50).

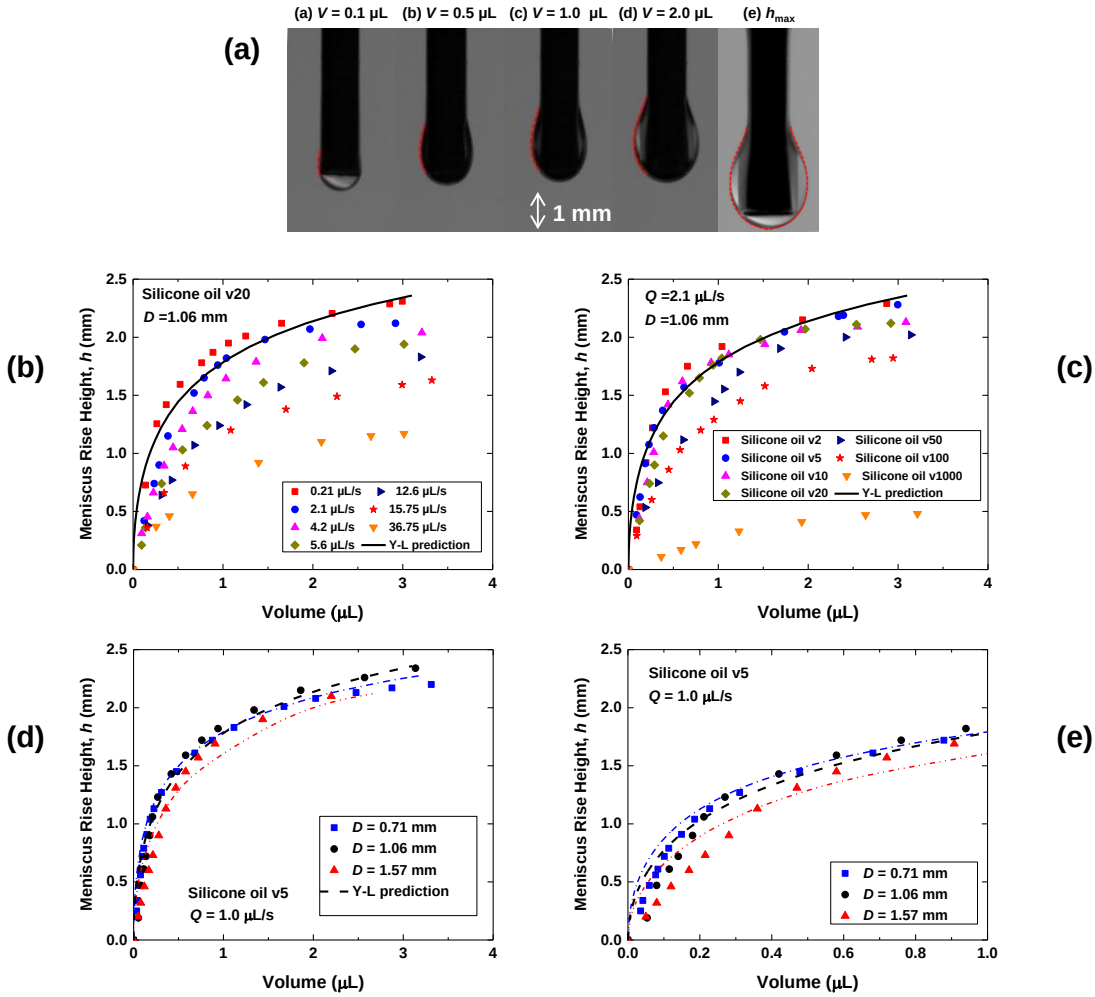

Figure 2.12: (a) Meniscus profiles of the silicone oil v50 on the nozzle outer wall at different times over one dripping period. The red dashed-lines show the meniscus profiles predicted using the Young-Laplace equation. Q = 0.5 µL/s, and D = 1.06 mm. (b) Variation in the rising meniscus height with accumulated volume for different volume flow rates at a fixed viscosity (silicone oil v20), and (c) for different viscosities at a fixed flow rate (Q = 2.1 µL/s). The nozzle diameter is fixed at D = 1.06 mm. (d) Variation in the rising meniscus height with accumulated volume for different nozzle outer diameters. (e) Shows the same results at an expanded volume scale. The results are for silicone oil v20 and at a fixed flow rate (Q = 1.0 µL/s).

Figure 2.12 also shows the variation in the height of the rising meniscus with accumulated volume for the silicone oils for a wide range of volume flow rates (Fig. 2.12b) and viscosities (Fig. 2.12c). The predictions from the Young-Laplace equation are shown as a solid line. The nozzle outer diameter is fixed at D = 1.06 mm. At sufficiently low flow rates, the predicted

evolutions agree with the experimental results from liquids with low viscosities. At higher flow rates and/or higher viscosities, the experimental results deviate from the predictions.

Figure 2.12d shows the variation in the height of the rising meniscus with accumulated volume for nozzles with different outer diameters. The flow rate is 1.0 μL/s and the liquid is silicone oil v5. For this low viscosity and low flow rate, the predictions generally agree well with the experimental results for the entire range of nozzle diameters used in the present study. When we zoom in (Fig. 2.12e), however, there is appreciable deviation at small volumes. This deviation arises in part from the limits of our assumption that the liquid meniscus is pinned at the bottom tip of the nozzle over the entire rising period.

We perform additional parametric numerical simulation runs for fictitious liquids with different physical properties (ρ = 440 ~ 950 kg/m^3, σ = 0.020~0.045 mN/m, μ = 4.6~48 mPa.s) to help establish quantitative limits on the flow rate where the quasi-static model for capillary-driven rising is valid as a function of the liquid properties and nozzle outer diameter. We use the predicted values of h_{max}^0 as our main parameter. We consider the dripping flows to be in the quasi-static regime when the experimentally measured or predicted h_{max} is within 15% of h_{max}^0 for the same nozzle diameter and liquid properties.

Figure 2.13 shows our flow regime map for *Bo* = 0.49, 0.71, and 1.05. The dashed line marks the boundary for the quasi-static regime. Figure 2.13d shows the results for a range of the Bond numbers examined in our simulations and/or experiments. As the viscosity (or the Ohnesorge number) increases, the flow rate and hence the Weber number needs to decrease to remain in the quasi-static regime. The Bond number has an even stronger effect on the rising behavior, which is understandable as the capillary-driven rise is governed primarily by the competition between the gravitational and surface tension force. The following correlation

captures the dependence of the threshold Weber number on the Bond number and the Ohnesorge number,

$$We_{quasi-static} = 2.37 \times 10^{-6} \times \frac{1}{Bo^8 Oh^2}.$$

As the flow rate increases, the inertia force becomes increasingly important and eventually dominant. A limiting value of We = 0.1, above which complex dripping or jetting occurs[7], is also shown.

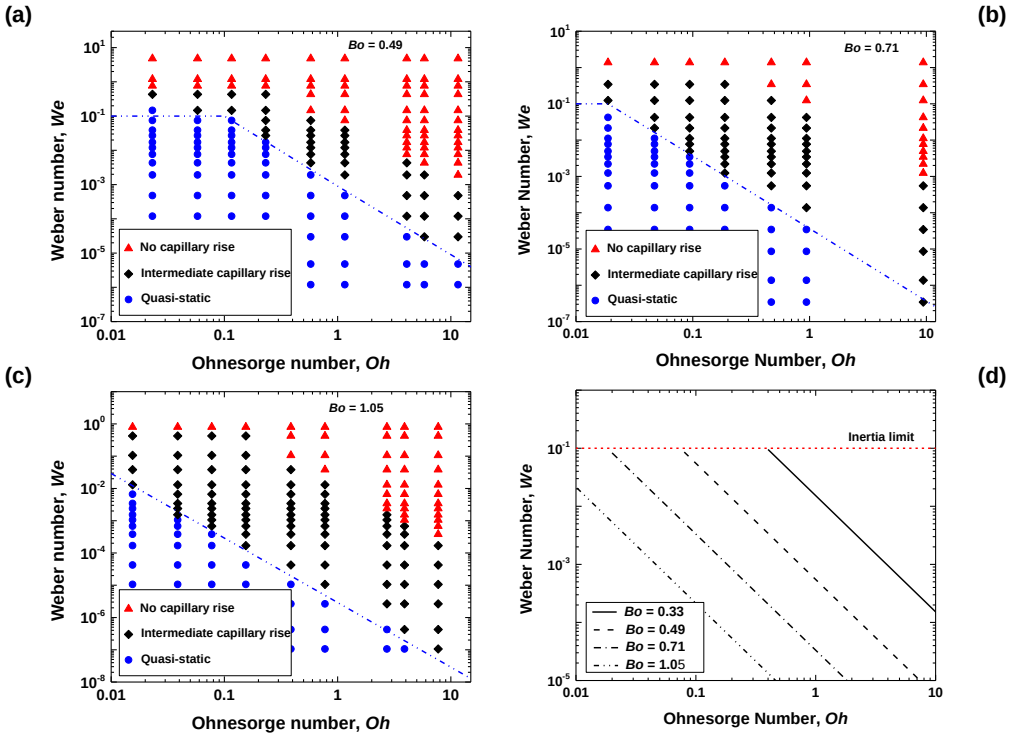

Figure 2.13: Proposed flow regime diagram for: (a) Bo = 0.49, (b) Bo = 0.71, and, (c) Bo = 1.06. (d) Proposed boundaries for the quasi-static regime for a range of Bond numbers. Data represent results from both experiments and simulations.

There is no noticeable capillary-driven rise of the liquid meniscus on the outer nozzle wall when the flow is in or in the immediate vicinity of the jetting regime. For liquids with low or moderate viscosities (Oh < 1), the transition between the dripping and jetting regime occurs at

high Weber numbers ($We > 0.1$), as alluded to earlier. In contrast, at high Ohnesorge numbers (*Oh* of the order of 1 or larger), the transition Weber number decreases with increasing *Oh*. Further discussion of the dripping-jetting transition in small nozzles can be found in the literature[7], [8].

2.4.5 Pendant drop method with wettable nozzles

In addition to using findings from present study as a guideline for nozzle design, the physics discussed can also help enhance the accuracy of surface tension measurement techniques such as pendant drop method. Considering the quasi-static case, by implementing the nozzle outer diameter (D), the maximum wetting length (h_{max}^{0}), and the contact angle (θ), in Young-Laplace equating, one can easily find the surface tension of the liquid. This means extracting the droplet profile is no longer needed, which is a huge step towards simplifying and reducing the errors in the pendant drop measurement method.

More importantly, we no longer need to apply extremely low flow rates to maintain the droplet shape and experience the risk of liquid evaporation, which gets more critical for low viscosity, and hence highly volatile liquids. We indeed use relatively high flow rates, still within quasi-static regime with respect to the regime transition criteria presented here, for our study on gasoline to avoid the trouble which, also, verifies the point.

Although researchers have already tried to address the problem with evaporation by using drop weight method, the need of using a correction curve[80] to take into account the inevitable role of secondary (i.e. satellite) droplets makes the process more complicated with respect to the old-fashioned pendant drop method.

2.5 Summary

We conduct a comprehensive experimental and numerical study on the capillary-driven rise of wetting liquids on the outer surface of small-sized cylindrical nozzles in the dripping regime. We perform the study over a wide range of nozzle outer diameter (0.5 to 3.2 mm), flow rate (0.2 to 300 μL/s), viscosity (1.75 to 970 mPa s), density (440 to 950 kg/m^3), and surface tension (18.7 to 45 mN/m). Hence, the combined numerical and experimental study in present work is for 0.33 $<Bo<$ 1.05, 10^{-7} $<We<$ 10, and 0.01 $<Oh<$ 10. In general, as the flow rate or the viscosity increases, the capillary rise height over each dripping period becomes smaller. Further, we define criteria based on three non-dimensional numbers (Weber, Bond, and Ohnesorge numbers) presenting the interaction between viscous, gravitational, capillary, and inertial forces to distinguish different rising behaviors. For capillary rise with quasi-static behavior, we use Young-Laplace equation along with mass conservation to predict the meniscus evolution with volume. Similarly, the limiting meniscus height for a given liquid and contact angle can be precisely predicted with Young-Laplace equation. The Bond numbers addressing the nozzle sizes that give the maximum meniscus rise and the onset of capillary rise cessation are characterized as a function of the contact angle and are irrespective to the liquid properties.

The present study helps improve our understanding of a complex interfacial phenomenon and leads to a more efficient and optimized nozzle design in systems using wetting liquids by reducing the risks of both contamination and high pressure drop in such devices. Nevertheless, physics studied here helps enhancing the accuracy of pendant drop surface tension measurement method.

CHAPTER 3

Thermally driven coalescence in thin liquid film flowing down a fiber

This chapter presents a study on the dynamics of a thin liquid film flowing down a vertical cylindrical fiber under a streamwise thermal gradient. Previous works on isothermal flows have shown that the inlet flow and fiber geometry are the main factors that determine a transition from the absolute to the convective instability flow regimes. Our experiments demonstrate that an irregular wavy pattern and bead coalescence, which are commonly seen in the convective regime, can also be triggered by applying a thermal gradient along the fiber. We develop a lubrication model that accounts for gravity, temperature-dependent viscosity and surface tension to describe the thermal effects on downstream bead dynamics. Numerical simulations of the model show good agreement between the predicted droplet coalescence dynamics and the experimental data.

3.1 Background

Thin liquid films flowing down a vertical fiber subject to thermal effects have been previously studied owing to their importance in a variety of industrial applications, which include dry cooling systems [12], [13], and heat and mass exchangers for vapor, CO2 and particle capture [1], [2], [4]. In addition to gravity and bulk surface tension, changes in liquid properties like surface tension and viscosity, which arise from the presence of a temperature gradient, influence the characteristics of these thin film flows. An improved understanding of the thermally driven bead coalescence is crucial for the systematic design of these systems [13].

Several research groups have experimentally investigated and analyzed different flow regimes of liquid films flowing down a string [15], [92]–[94]. Kliakhandler *et al.* [15] ran a set of experiments using a fiber with a size that is comparable to the liquid film thickness to study the effect of the flow rate on the flow regime. They qualitatively observed three different regimes of the interfacial patterns in the form of the travelling liquid beads. At low flow rates, the isolated droplet regime occurs where widely spaced large droplets flow down the fiber separated by secondary small-amplitude wavy patterns. At higher flow rates, the Rayleigh–Plateau (RP) flow regime emerges where a stable train of droplets propagate at a constant speed. If the flow rate is increased further, the convective instability regime emerges as collisions of large droplets occur in an irregular fashion. This instability can also be triggered by applying a gradient to the physical properties (i.e., surface tension/viscosity) of the liquid film along the fiber [18].

Prior experimental works have shown that maintaining a stable train of liquid beads is important for the reliable heat and mass transfer performance in many applications [19]–[21]. For example, Nozaki, Kaji & Mod in 1998 [95] investigated the cooling of thin films of a heated

silicone oil flowing down a string. They demonstrated that at the same liquid flow rate, the string-of-beads flow exhibits a higher overall heat transfer coefficient than the annular film flow.

In our earlier work [96] we experimentally studied the relationship between flow characteristics and the overall effectiveness of heat exchange for thin liquid films flowing along a single string against a counterflowing air stream. The experiments showed that for very high liquid inlet temperatures, the flow no longer remains in the desired RP regime and can undergo a regime transition along the fiber. After travelling a certain distance away from the nozzle, the liquid droplets collide with each other, which causes cascade coalescence further downstream. This type of thermally driven coalescence will be the focus of the present study.

For low flow rates where the inertial effects are negligible, the classical lubrication theory may be applied to model the dynamics of viscous films flowing down vertical cylinders. Under the small-interface-slope assumption, weakly nonlinear lubrication equations for the film thickness have been acquired in the works of Frenkel [97], Chang & Demekhin [98] and Kalliadasis & Chang [99]. Both stabilizing and destabilizing effects of the surface tension are incorporated into the model, which characterizes the axial and azimuthal curvatures of the free interface. In the work of Craster & Matar [100], an asymptotic model was derived using a low Bond number, surface-tension-dominated theory. Full curvature terms were introduced in the work of Kliakhandler *et al.* [15], and the existence of non-negative solutions to their model is shown in Ji, Taranets & Chugunova [101]. Recently, Ji *et al.* [94] investigated a full lubrication model that incorporates fully nonlinear curvature terms, slip boundary conditions and a film stabilization mechanism.

For higher flow rates where inertial effects are no longer negligible, Trifonov [102], Ruyer-Quil *et al.* [103] and Duprat, Ruyer-Quil & Giorgiutti-Dauphiné [104] investigated systems of coupled equations for the film thickness and the flow rate based on the integral boundary layer approach. This approach was further extended by Ji *et al.* [105] through introduction of the film stabilization mechanism to address the influence of nozzle geometry on the downstream droplet dynamics.

Although many previous studies have focused on the dynamics of viscous thin films flowing down fibers, the thermal effects on the fiber coating dynamics have received less attention. For non-isothermal liquid films flowing along an inclined substrate, Kabova, Kuznetsov & Kabov [106] derived a thin film equation that incorporates the influence of temperature-dependent viscosity and surface tension. This problem was also investigated by Ruyer-Quil *et al.* [107] using a weighted residuals approach. Haimovich & Oron [108] studied the dynamics of a non-isothermal liquid film on an axially oscillating horizontal cylinder. More recently, Liu, Ding & Zhu [109], Liu *et al.*[18], Ding & Wong [110] and Ding *et al.* [111] used lubrication models to study the influence of thermocapillary on the coating flow down a vertical fiber subject to a temperature gradient. Their work focused on the Marangoni effects that originate from the linear dependence of the variation of surface tension with temperature. The works of Liu, Chen & Wang [112] and Dong, Li & Liu [113] extended this result by considering a self-rewetting fluid [114] with the surface tension modelled as a quadratic function of temperature. Ding *et al.* [115] also investigated the influence of thermally induced Marangoni effects and van der Waals attractions on the break-up of ultra-thin liquid films [116].

In this study, we experimentally and theoretically investigate the thermal effects on the dynamics of thin viscous films flowing down a vertical fiber. We propose a lubrication model that incorporates both temperature-dependent viscosity and surface tension. Using this model, we numerically explore the downstream flow dynamics that form bead coalescence and obtain a good agreement with experimental results. A simplified ordinary differential equation (ODE) model is also developed to capture the influence of thermal effects on liquid bead dynamics.

The rest of this chapter is organized as follows. In the following section, we describe the experimental set-up. Next, we introduce the incompressible Navier-Stokes approach and derive the lubrication model for the film thickness by accounting for the presence of a temperature field. In the subsequent section we provide a discussion on the stability of the lubrication model for both isothermal and weakly non-isothermal cases. Finally, we present the numerical study of thermally-driven bead coalescence using lubrication theory followed by a comparison between the results from the theory, incompressible Navier-Stokes simulations, and experimental observations.

3.2 Experimental setup

Figure 3.1 shows a schematic of the experimental set-up used in this study to investigate the characteristics of a liquid film flowing down a vertical string under a streamwise temperature gradient. The main parts of this set-up are: (1) a programmable syringe pump to pump the liquid through the nozzle at a fixed flow rate, (2) an in-line heater that controls the liquid temperature to a prescribed value at the nozzle inlet, (3) a stainless steel nozzle with an inner diameter of 1.2 mm and outer diameter of 1.55 mm, (4) a thermocouple to record the liquid temperature at the

tip of the nozzle outlet (additional thermocouples are used to measure the axial temperature distribution of the liquid along the fiber), (5) a high-speed camera (frame rate of 1000 frames s−1) mounted on a translation stage, (6) a weight connected to the fiber to ensure the fiber stays vertical, (7) a liquid reservoir, (8) a weight scale to measure the liquid mass flow rate and (9) a computer for data acquisition.

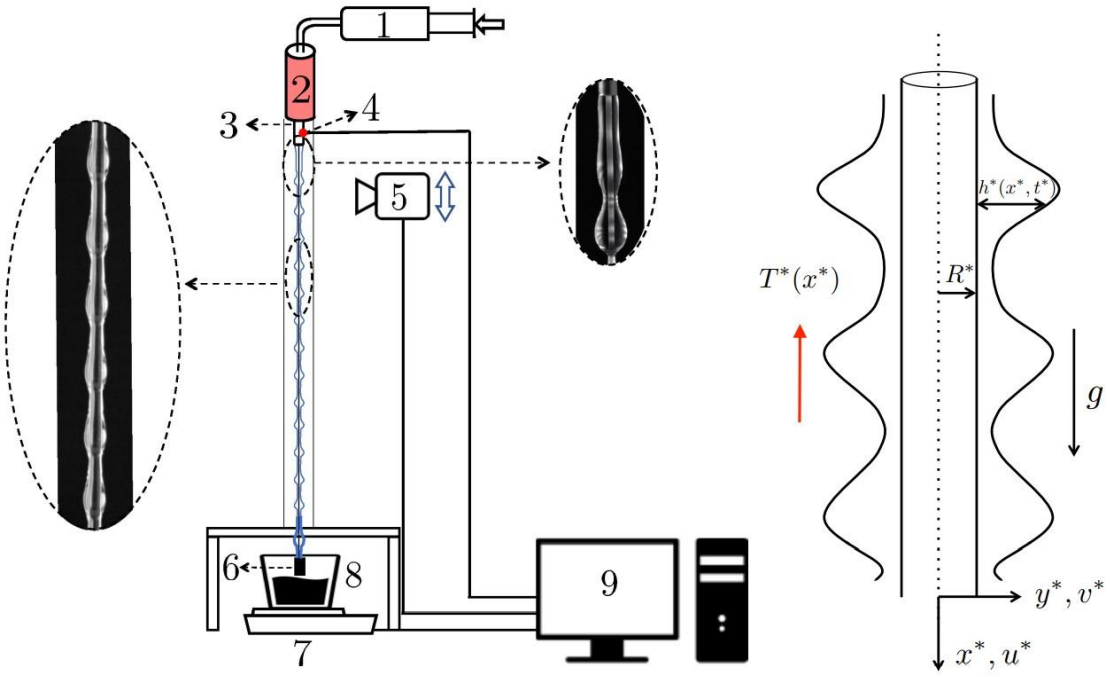

Figure 3.1: (a) Schematic of the experimental set-up. An inline heater is integrated into the inlet of the nozzle to create a temperature gradient along the fiber. (b) Schematic of a thin liquid film flowing down a vertical cylindrical fiber under a streamwise temperature gradient.

The experiments were performed using polymer-based fibers with a diameter of 0.61 mm. The liquid mass flow rate was varied in the range of 0.0013–0.016 g s−1. The nozzle outer diameter was OD 1.55 mm. We used Rhodorsil silicone oils (v20, v50 and v100) as well-wetting liquids with a low surface energy. The inlet temperature of the liquid was changed in the range of 30–70 ˚C. A summary of the experimental conditions is presented in Table 3.1.

Table 3.1: Experimental cases of different Rhodorsil silicone oils (v20, v50 and v100), inlet temperatures, mass flow rates and liquid properties at 20 ˚C.

Liquid	Density ρ (kg/m^3)	Surface Tension σ_0 (mN/m)	Viscosity ν_0 (mm^2/s)	Inlet Temperature T^*_{IN} ($^\circ C$)	Mass flow rate Q^* (g/s)
v20	950	20.3	22.1	30 – 70	0.008, 0.016
v50	963	20.4	55.2	30 – 70	0.0053, 0.008
v100	965	20.6	110.4	30 – 60	0.0013, 0.0027

3.3 Incompressible Navier-Stokes numerical simulation

To compare the computational effort needed for the flow simulation and partially validate the lubrication modelling work, we implement the volume of fluid (VOF) method using a commercial computational fluid dynamics package to model the two-phase flow and track the liquid–air interface. We consider a two-dimensional and axisymmetric flow domain for solving incompressible Navier–Stokes equations for the unsteady problem.

Figure 3.2 shows the numerical simulation domain and the boundary conditions we use for our Navier–Stokes numerical simulation. We use the pressure implicit with splitting of operators (PISO) algorithm to handle the pressure-velocity coupling [117]. We use the pressure staggering scheme (PRESTO) to calculate the pressure on the faces (rather than the nodes), and the second-order upwind scheme to discretize the momentum equations. We adopt the continuum surface force (CSF) model proposed by Brackbill, Kothe & Zemach [84], where the effect of surface tension is represented as a source term in the momentum equations. We do not introduce any artificial perturbation in our simulation but rely instead on noise inherent in the numerical simulation to initiate instability.

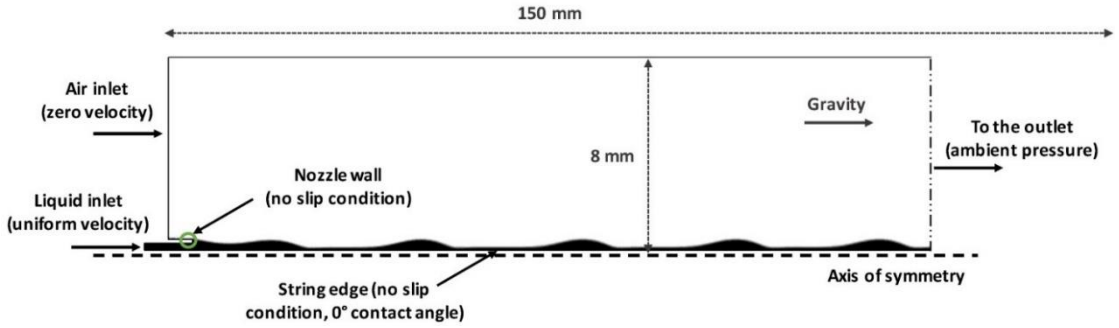

Figure 3.2 : Navier–Stokes numerical simulation domain and boundary conditions.

We include the effect of a temperature gradient using user-defined functions for surface tension and viscosity from Figure 3.3. The computational domain (150 mm × 8 mm) is discretized using an unstructured quadrilateral mesh with a minimum element size of approximately 0.02 mm. The mesh was refined locally near the nozzle wall and the string and was coarsened far away from the string. The total number of mesh elements was approximately 200 000 and the time step size was 10−4 s. We use a workstation with a CPU with 24 cores, each running at 3 GHz, and 64 GB of RAM.

3.4 Temperature distribution along the fiber

Previous studies [18] of the thermal effects on liquid films typically assume a constant temperature gradient. In this work, we instead represent the streamwise temperature variations under our experimental conditions using a solution to a lumped capacitance model:

$$\Theta = exp\left[-\left(\frac{h_b A_s}{m_b v_b c}\right) x^*\right]. \qquad (3.1)$$

The works in [19], [96] showed that radial temperature variation within each liquid bead is negligible due to efficient mixing associated with internal circulation within the bead. Axial heat

conduction is neglected. In the model (3.1), $\Theta = (T^* - T_0^*)/\Delta T$ is the dimensionless temperature, where $\Delta T = T_{IN}{}^* - T_0^*$ is the temperature scale set by the difference between the inlet temperature $T_{IN}{}^*$ and the room temperature T_0^*. A_s represents the surface area of the liquid beads, c the specific heat of the liquid, v_b the liquid bead velocity, m_b the mass of each bead, x^* the distance from the inlet, and h_b the liquid bead-to-air heat transfer coefficient. We use the empirical relationship for the heat transfer coefficient of flow around a sphere [118], [119] to obtain the value of h_b,

$$\frac{h_b D_b}{k_{air}} = 2 + \left(0.4 Re_b^{1/2} + 0.06 Re_b^{2/3}\right) Pr_{air}^{0.4}. \qquad (3.2)$$

Here, $Re_b = \rho_{air} v_b D_b/\mu_{air}$ is the bead Reynolds number, D_b is the bead diameter, and Pr_{air} is the Prandtl number of air. μ_{air}, ρ_{air} and k_{air} are the viscosity, density, and thermal conductivity of air, respectively. The temperature profiles obtained from the lumped capacitance model (3.1) are later used in the lubrication model to represent the axial variations in the surface tension and viscosity along the fiber.

As shown in Figure 3.3, the model captures the experimentally measured liquid temperature profiles well. For later convenience, we rewrite the dimensionless temperature distribution in a rescaled form

$$\Theta_I(x) = 1 - \frac{1 - exp(-\chi x)}{1 - exp(-\chi L_0)}. \qquad (3.3)$$

where x is the dimensionless streamwise spatial variable, L_0 is the dimensionless downstream position where the room temperature T_0^* is nominally reached. The temperature profile (3.3) satisfies $\Theta_I(0) = 1$ and $\Theta_I(L_0) = 0$, and the dimensionless parameter χ specifies the temperature gradient. In all simulations, we set $L_0 = L_0^*/\ell$, where $L_0^* = 0.5$ m and ℓ is the length scale in the streamwise direction, which will be defined in subsequent sections.

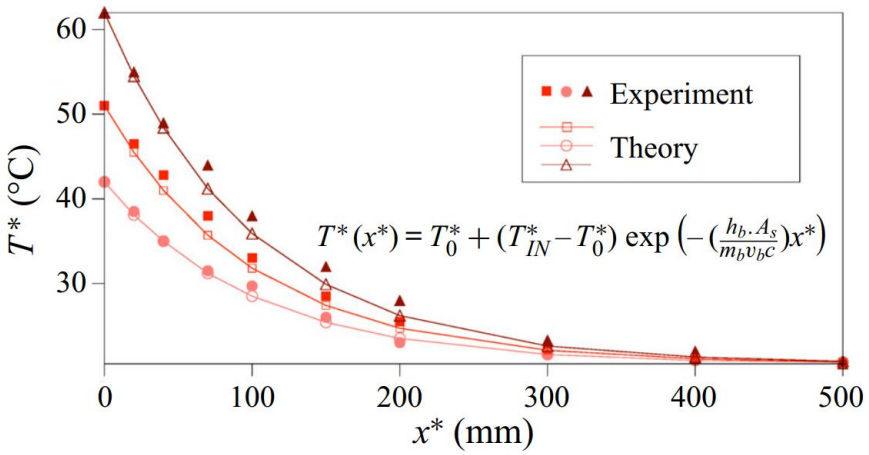

Figure 3.3 : Temperature profiles measured in experiments along the fiber for silicone oil v50 with different inlet temperatures compared with the prediction based on the model (3.1). The parameters are h_b = 44 W (m^2 K)$^{-1}$, A_s = 13.2 mm^2, c = 1510 J(kg K)$^{-1}$, m_b = 2.04 × 10^{-6} kg and v_b = 19.2 mm s^{-1}.

3.5 Temperature dependent liquid properties

Liquid properties can change significantly as the temperature is varied. In this work, we focus on the influence of temperature on the surface tension and viscosity of the liquid.

To characterize the temperature dependence of the surface tension of our liquid, we measured the rising height, h_{rise}, in a capillary tube with an inner diameter, r_{tube}, of 0.5 mm at various temperatures (20–110 ˚C). We then used $\sigma = (r_{tube} h_{rise} \rho g) / (2 \cos \theta)$ to estimate the surface tension at each temperature [120]. Here, θ is the contact angle on the capillary tube wall that we measured independently. All the experiments were performed in an isothermal container.

Figure 3.4(a) shows the experimental results for the surface tension, σ (mN m^{-1}), of silicone oil v50. The experimental uncertainty in the measured surface tension is estimated to be 0.3 mN m^{-1} and the uncertainty in the measured temperatures is estimated to be ±0.5 ˚C.

The kinematic viscosity $\nu(T^*)$ (mm^2 s^{-1}) of silicone oil v50 as a function of the temperature

T^* (˚C) was provided by the manufacturer (see Shin-etsu 2005 [121]). A plot of the relation between viscosity and temperature is included in Figure 3.4(b).

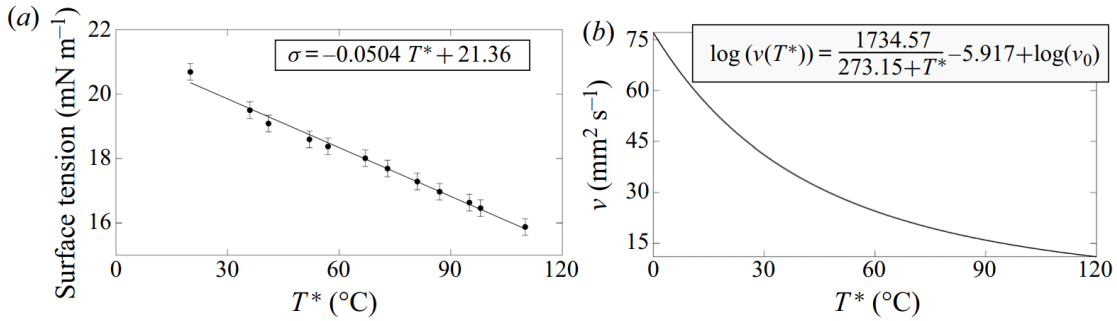

Figure 3.4 : (a) Surface tension and (b) viscosity of silicone oil v50 as functions of temperature T^*.

For simplicity, in the model derived here, we make an approximation that the kinematic viscosity ν and the surface tension σ of the liquid are linearly dependent on temperature,

$$\nu(T^*) = \nu_0 - \nu_T(T^* - T_0^*), \sigma(T^*) = \sigma_0 - \sigma_T(T^* - T_0^*), \qquad (3.4a,b)$$

where ν_0, ν_T, σ_0, $\sigma_T > 0$ are constants. Using the dimensionless temperature variable, one can also write $\nu = \nu_0 - \nu_T \Delta T\Theta$ and $\sigma = \sigma_0 - \sigma_T \Delta T\Theta$.

In this chapter, we have the reference room temperature T_0^* = 20˚C, σ_T = 0.0504 mN (m˚C)$^{-1}$ and $\nu_T = (\nu_0 - \nu(T_{IN}^*)) / \Delta T$. The density of the liquid is assumed to be constant.

3.6 Lubrication model

Next, we derive the governing equations following the works of Craster & Matar [100], Ruyer-Quil et al. [103] and Ji et al. [94]. We choose the length scale in the radial direction y as H and the length scale in the streamwise direction x as $\ell = H/\varepsilon$. The scale ratio ε is set by the

balance between the surface tension and the gravity g and is given by $\varepsilon = (\rho g H^2/\sigma_0)^{1/3}$. This scale ratio is small (approximately 0.35) in typical experiments and can also be rewritten as $\varepsilon = We^{-1/3}$, where the Weber number $We = (l_c/H)^2$ compares the capillary length $l_c = \sqrt{\sigma_0/(\rho g)}$ with the radial length scale H. The characteristic streamwise velocity is $U = (gH^2)/v_0$, and the pressure and time scales are given by $\rho g \ell$ and $(v_0 \ell)/(gH^2)$, respectively. Following the approach in Ji et al. [94], [105], we include a film stabilization term $\Pi(h)$,

$$\Pi(h) = -\frac{A}{h^3}, \qquad (3.5)$$

where $A > 0$ is a stabilization parameter. This term takes the functional form of the long-range disjoining pressure of the van der Waals model that characterizes the microscopic quantities for wetting liquids, and A is typically referred as a Hamaker constant [122].

The dynamics of the axisymmetric flows is governed by the Navier–Stokes equations, the continuity equation, and the energy equation. This system is coupled with the temperature-dependent viscosity and surface tension given by (3.4a,b). With these scales, we write the non-dimensional Navier–Stokes equations using dimensionless variables as

$$\varepsilon^2 Re\left(u_t + uu_x + vu_y\right) = -p_x - \Pi_x + 1 + (1-\kappa\Theta)\left(\frac{u_y}{y} + u_{yy} + \varepsilon^2 u_{xx}\right), \quad (3.6a)$$

$$\varepsilon^4 Re\left(v_t + vv_y + uv_x\right) = -p_y + \varepsilon^2(1-\kappa\Theta)\left(\frac{u_y}{y} + u_{yy} + \varepsilon^2 u_{xx}\right), \quad (3.6b)$$

$$v_y + \frac{v}{y} + u_x = 0, \qquad (3.6c)$$

where the Reynolds number $Re = U\ell/v_0$, and the constants $\kappa = v_T \Delta T/v_0$ and $\omega = \sigma_T \Delta T/\sigma_0$ scale the relative change in viscosity and surface tension as the temperature is varied.

The balances of normal and tangential stresses at $y = h + R$ are expressed as

$$\left(1-\varepsilon^2 h_x^2\right)\left(\varepsilon^2 v_x + u_y\right) + 2\varepsilon^2 h_x\left(v_y - u_x\right) = -Ma\,\frac{\left(1+\varepsilon^2 h_x^2\right)^{1/2}}{1-\kappa\Theta} + \left(h_x\Theta_y + \Theta_x\right), \quad (3.6d)$$

$$p + \Pi = \varepsilon^4 Re\left(\frac{\alpha}{\varepsilon^2(1+\alpha h)\left(1+\varepsilon^2 h_x^2\right)^{\frac{1}{2}}} - \frac{h_{xx}}{\left(1+\varepsilon^2 h_x^2\right)^{\frac{3}{2}}} - \frac{A}{h^3}\right)(1-\omega\Theta)$$
$$+\frac{2\varepsilon^2(1-\kappa\Theta)}{1+\varepsilon^2 h_x^2}\left[\varepsilon^2(h_x^2 u_x - h_x v_x) - h_x u_y + v_y\right], \quad (3.6e)$$

where $Ma = (\sigma_T \Delta T)/(\rho g H l)$ is the Marangoni parameter, $\alpha = H/R^*$ is the aspect ratio of the characteristic radial length scale and the fiber radius, and the dimensionless fiber radius is $R = R^*/H$. At the interface between the solid substrate and the liquid, $y = R$, we impose the no slip and no penetration boundary conditions,

$$u = v = 0, \text{ at } y = R. \quad (3.6f)$$

The kinematic boundary condition at $y = R + h$ is given by

$$h_t + u h_x = v, \text{ at } y = R + h. \quad (3.6g)$$

Next, we simplify the above set of governing equations following Ruyer-Quil et al. [103]. Under the lubrication approximation, we neglect the inertial contributions by assuming that $Re = O(1)$ and $\varepsilon << 1$. Omitting the terms of order $O(\varepsilon^2)$, we rewrite the leading order non-dimensional reduced momentum and continuity equations for the velocity field (u, v) and the dynamic pressure p as

$$1 - \frac{\partial p}{\partial x} - \frac{\partial \Pi}{\partial x} + (1-\kappa\Theta)\left(\frac{\partial^2 u}{\partial y^2} + \frac{u_y}{y}\right) = 0, \quad (3.7a)$$

$$-\frac{\partial p}{\partial y} = 0, \quad (3.7b)$$

$$\frac{\partial u}{\partial x} + \frac{\partial v}{\partial y} + \frac{v}{y} = 0. \quad (3.7c)$$

Based on our previous discussion, the radial temperature variations within liquid droplets and across the inter-bead precursor layer are negligible compared with the streamwise temperature variations. Therefore, we assume that the temperature is constant in the radial direction and only varies in the axial direction in the leading order, $\Theta = \Theta_l(x)$. The balance of tangential stresses at the free surface $y = h + R$ reduces to

$$u_y = -\frac{Ma}{1-\kappa\Theta}\left(h_x\Theta_y + \Theta_x\right) = -\frac{Ma\Theta_x}{1-\kappa\Theta}. \quad (3.7d)$$

The balance of normal stresses at the free surface $y = h + R$ becomes

$$p + \Pi = \left(\frac{\alpha}{\varepsilon^2(1+\alpha h)} - \frac{\partial^2 h}{\partial x^2} - \frac{A}{h^3}\right)(1 - \omega\Theta). \quad (3.7e)$$

The two terms on the right-hand side of (3.7e), $\alpha/(\varepsilon^2(1 + \alpha h))$ and $\partial^2 h/\partial x^2$, describe both the destabilizing and stabilizing roles of the surface tension that originate from the azimuthal and axial curvature of the free surface, respectively. The balance between the azimuthal and axial scales is characterized by α and ε. Here we use linear forms for both curvature terms; a discussion of other appropriate forms for the curvature terms can be found in Ji et al. [94].

Combining the kinematic boundary condition (3.6g), the no slip and no penetration boundary conditions (3.6f) and the continuity equation (3.7c) lead to the mass conservation equation

$$(1 + \alpha h)\frac{\partial h}{\partial t} + \frac{\partial q}{\partial x} = 0, \text{ where } q = \frac{1}{R}\int_R^{h+R} uy\, dy. \quad (3.8)$$

Equation (3.7b) indicates that the pressure p is a function of x only. Integrating (3.7a) twice and using (3.7d) yields

$$u = \frac{1}{1-\kappa\Theta(x)}\left[\frac{1 - p_x - \Pi_x}{2}\left(-\frac{1}{2}(y^2 - R^2) + (h+R)^2 \ln\left(\frac{y}{R}\right)\right)\right.$$
$$\left. -Ma\Theta_x(R+h)\ln\left(\frac{y}{R}\right)\right]. \quad (3.9)$$

Because $\alpha = H/R^* = 1/R$, by using (3.8), we obtain the form of flux q

$$q = \frac{1}{1-\kappa\Theta}\left(\frac{h^3}{3}\phi(\alpha h)(1 - p_x - \Pi_x) -\right) - Ma\Theta_x h^2\psi(\alpha h), \quad (3.10)$$

where the shape factors ϕ and ψ are functions defined by

$$\phi(X) = \frac{3}{16X^3}((1+X)^4(4\ln(1+X) - 3) + 4(1+X)^2 - 1), \quad (3.11)$$

$$\psi(X) = \frac{1+X}{X^2}\left((1+X)^2\ln(1+X) - X\left(\frac{1}{2}X + 1\right)\right). \quad (3.12)$$

In the limit of $X \to 0$, we have

$$\phi(X) = 1 + X + \frac{3}{20}X^2 + O(X^3),\ \psi(X) = 1 + \frac{4}{3}X + \frac{1}{4}X^2 + O(X^3). \quad (3.13a,b)$$

Given a dimensional volumetric flow rate Q_m and fiber radius R^*, we define the volumetric flow rate per circumference unit q_0^* as $q_0^* = Q_m/(2\pi\rho R^*)$. We set the characteristic axial length scale H by solving (3.10) for h with $q = q_0^*$, $\Theta \equiv 0$, $\Pi_x \equiv 0$ and $p_x \equiv 0$. That is, we set the length scale H by the film thickness h_N^* of a uniform Nusselt flow at room temperature T_0^* with constant dynamic viscosity v_0 [103], [104].

Finally, by rescaling the time scale $t \to t/\varphi(\alpha)$, and combining (3.8), (3.10) and (3.7e), we obtain the dimensionless governing equation for $0 \le x \le L$,

$$\frac{\partial}{\partial x}\left(h + \frac{\alpha}{2}h^2\right) + \frac{\partial q}{\partial x} = 0, \quad (3.14a)$$

where the flux takes the form

$$q = M(h)\left(1 - \frac{\partial}{\partial x}[(1-\omega\Theta)(\zeta(h) - h_{xx})]\right) - \frac{h^2}{2}\frac{\Theta_x Ma}{1-k\Theta}\frac{\psi(\alpha h)}{\phi(\alpha)}, \quad (3.14b)$$

where the mobility function is

$$M(h) = \frac{h^3}{3(1-k\Theta)}\frac{\phi(\alpha h)}{\phi(\alpha)}, \quad (3.14c)$$

and the function $\zeta(h)$ consists of the destabilizing azimuthal curvature term $\alpha/(\eta(1+\alpha h))$ and the film stabilization term $\Pi(h)$,

$$\zeta(h) = \frac{\alpha}{\eta(1+\alpha h)} + \Pi(h), \quad \Pi(h) = -\frac{A}{h^3}, \qquad (3.14d)$$

where the scaling parameter $\eta = \varepsilon^2$.

This choice of time scale leads to a normalized mobility function that satisfies $M = 1/3$ for $h = 1$ and $\Theta \equiv 0$. The model (3.14) can be written as a fourth-order nonlinear partial differential equation (PDE) for the thickness $h(x, t)$. It accounts for temperature-dependent viscosity and surface tension gradients, gravity and azimuthal instabilities, but neglects the inertia and streamwise viscous dissipation that are included in the work of Ruyer-Quil et al. [104]. We note that because $0 \le \kappa < 1$ and $0 \le \Theta \le 1$, we have $0 < 1 - \kappa\Theta \le 1$ in (3.14b) and (3.14c).

Compared with the prior work in Liu et al. [18] that focuses on the thermocapillarity effects in similar dynamics, this new model includes additional physics through the temperature-dependent viscosity and does not require the aspect ratio α to satisfy $\alpha << 1$. Our model with $\kappa = Ma = \omega = A = 0$ is also consistent with the model derived in the work of Craster & Matar [100] except for a scaling difference.

In the limit $\alpha \to 0$, the model (3.14) describes the dynamics of a draining film flowing down an incline under thermal effects. If we assume that the viscosity is constant and set $\kappa = Ma = \omega = A = 0$, (3.14) reduces to (3.15), which describes thin film dynamics driven by the gravity and a surface tension gradient owing to a temperature gradient,

$$h_t + \left(\frac{1}{3}h^3 - \frac{1}{2}h^2\Theta_x Ma\right)_x = -\frac{1}{3}(h^3 h_{xxx})_x . \quad (3.15)$$

The cubic term and quadratic term on the left-hand side of (3.15) originate from gravity and the Marangoni stress, respectively. In this study, we consider a decreasing temperature field,

$\Theta_x<0$, and the surface tension gradient is expected to promote the downward movement of the film.

3.7 Stability analysis

In this section, we investigate the instability of the model by considering two cases, (a) the isothermal case where the fiber is uniformly heated and (b) the weakly non-isothermal case, where a temperature gradient is imposed along the fiber. We will discuss the influence of the temperature-dependent liquid properties on both the temporal instability and absolute/convective instability transition of the system.

3.7.1 Isothermal films

We begin by considering the flow instability of a uniformly heated thin fluid film flowing down a vertical fiber. Specifically, we study an isothermal film with spatially constant surface tension and viscosity at a temperature $\Theta(x) \equiv \Theta_0$ and $d\Theta/dx = 0$, where $0 \leq \Theta_0 \leq 1$. Then the governing equation (3.14) reduces to

$$\frac{\partial}{\partial x}\left(h + \frac{\alpha}{2}h^2\right) + \frac{\partial}{\partial x}\left[M(h)\left(1 - (1 - \omega\Theta_0)\frac{\partial}{\partial x}\left(\frac{\alpha}{\eta(1+\alpha h)} - h_{xx} + \Pi(h)\right)\right)\right] = 0, \quad (3.16)$$

where the mobility function takes the form $M(h) = [h^3\ \phi\ (\alpha h)]/[3(1 - \kappa\Theta_0)\phi(\alpha)]$. We perturb the uniform base state $\bar{h} = 1$ by an infinitesimal Fourier mode,

$$h = \bar{h} + \bar{\psi}e^{i(kx - \Lambda t)}, \quad (3.17)$$

where k is the wavenumber, Λ is the wave frequency and $\bar{\psi}$ ($<< 1$) is the initial amplitude.

Expanding the PDE (3.16) then gives the dispersion relation

$$\Lambda = C(\alpha, \kappa, \Theta_0)k + ik^2 D(\alpha, \kappa, \omega, \Theta_0)\left[-k^2 + \frac{\alpha^2}{\eta(1+\alpha)^2} - 3A\right], \quad (3.18)$$

where

$$C(\alpha, \kappa, \Theta_0) = \frac{\alpha\phi'(\alpha)+3\phi(\alpha)}{3(1-\kappa\Theta_0)(1+\alpha)\phi(\alpha)}, \qquad D(\alpha, \kappa, \omega, \Theta_0) = \frac{1-\omega\Theta_0}{3(1-\kappa\Theta_0)(1+\alpha)}. \quad (3.19)$$

The relation (3.18) indicates that the azimuthal curvature term $\alpha/(\eta(1 + \alpha h))$ is destabilizing, and both the streamwise curvature term h_{xx} and the film stabilization term Π (h) are stabilizing. For $\kappa > 0$, the temporal instability is enhanced by the thermal-viscosity influence.

Following the work of Ji et al. [94], we select the stabilization parameter A based on the dimensional thickness $\varepsilon_p = Hh_c$ of a stable uniform layer based on experiments, where h_c is the dimensionless thickness of the stable coating film. Specifically, we pick $A = A_c$, where

$$A_c = \frac{\alpha^2 h_c^4}{3\eta(1+\alpha h_c)^2}, \qquad (3.20)$$

which ensures that any thin flat film $h \leq h_c$ is linearly stable ($\mathrm{Im}(\Lambda) < 0$) for all real wave numbers $k > 0$.

To understand the spatiotemporal stability of the uniform state, we consider the peak of a localized wave packet that travels with a speed given by the group velocity $v_g = \mathrm{d}\Lambda/\mathrm{d}k$, where both Λ and k are complex. The merging of two disconnected spatial branches at a point in the complex k-plane leads to a vanishing group velocity k_0, $v_g|_{k=k0} = 0$, which defines the absolute wavenumber k_0 and the corresponding absolute frequency $\Lambda_0 = \Lambda(k_0)$ (Duprat et al. 2007; Scheid, Kofman & Rohlfs 2016)[92], [123]. For $\mathrm{Im}(\Lambda_0) > 0$, the system presents absolute instability; for $\mathrm{Im}(\Lambda_0) < 0$, the fluid film shows convective instability. The absolute/convective (A/C) instability transition corresponds to a real absolute frequency, $\mathrm{Im}(\Lambda_0) = 0$.

Following the approach in the work of Duprat et al. (2007), we introduce the transformation

$$k = \tilde{k}\left(\frac{C}{3D}\right)^{1/3},\ \Lambda = \tilde{\Lambda}C\left(\frac{C}{3D}\right)^{1/3},\ \frac{\alpha^2}{\eta(1+\alpha)^2} - 3A = \beta\left(\frac{C}{3D}\right)^{2/3} \qquad (3.21)$$

and reduce the dispersion relation (3.18) to the equation

$$\tilde{\Lambda} = \tilde{k} + i\frac{\tilde{k}^2}{3}\left(\beta - \tilde{k}^2\right). \qquad (3.22)$$

This corresponds to the dispersion relation for a weakly nonlinear lubrication model studied in Frenkel [97]. Based on the calculation in Duprat et al. [92], the instability of the system becomes absolute when $\beta > \beta_{ca} \equiv [9/4(-17 + 7\sqrt{7})]^{1/3} \approx 1.507$. This leads to the A/C threshold for the instability of isothermal films,

$$\frac{3(1-\omega\Theta_0)\phi(\alpha)}{\alpha\phi'(\alpha)+3\phi(\alpha)}\left(\frac{\alpha^2}{\eta(1+\alpha)^2} - 3A\right)^{3/2} = \beta_{CA}^{3/2}. \qquad (3.23)$$

which shows that the A/C marginal curve is influenced by the thermal effects only through the prefactor $1 - \omega\Theta_0$, and the temperature-dependent viscosity does not play a role. We note that this conclusion may change if moderate inertia effects or streamwise heat diffusion is included in the model [103], [111], [123].

Following the studies of Duprat et al. and Ruyer-Quil & Kalliadasis [93], [104], we rewrite the threshold (3.23) in terms of R^*/l_c and α and obtain

$$\frac{1}{C_k(\alpha)(1+\alpha)^4}\left[\alpha^{2/3} - 3(1+\alpha)^2\left(\frac{R^*}{l_c}\right)^{4/3}A\right]^{3/2} = \beta_{CA}^{3/2}\mathcal{S}^2. \qquad (3.24)$$

where R^*/l_c is the ratio of the fiber radius R^* and the capillary length l_c, $C_k(\alpha)$ is the linear wave speed $C(\alpha, \kappa, \Theta_0)$ in (3.19) for $\kappa\Theta_0 = 0$, and $\mathcal{S} = (R^*/l_c)[1 - \omega\Theta_0]^{-1/2}$. For $\omega\Theta_0 = 0$ and $A = 0$, this threshold (3.24) is consistent with the A/C threshold proposed in the works of Ruyer-Quil & Kalliadasis and Duprat et al. [93], [104].

Figure 4 presents the A/C instability regimes predicted by (3.24) for isothermal films with $A = 0$. Downstream flow dynamics for the experiments in Table 3.1 are shown in figure 4 with circles representing the RP flow regime and crosses representing droplet coalescence dynamics. This analysis suggests that for all the experimental cases in the present study, the flow dynamics of the uniformly heated isothermal liquid film at the temperature T_{IN}^{*} fall in the absolute instability regime. Therefore, the bead coalescence observed in our experiments cannot take place without the presence of a temperature gradient. In particular, for $\omega = 0$, we note that for a spatially-constant temperature field $\Theta(x) \equiv \Theta_0$, a direct transformation $t \rightarrow t(1 - \kappa\Theta)$ in (3.14) leads to a PDE without any temperature-dependent terms. Therefore, for any trains of travelling beads in the absolute RP regime, we expect the flow to stay in the RP regime when the temperature is uniformly elevated across the fiber. This indicates that the non-uniform temperature field $\Theta(x)$ is crucial for the bead coalescence observed in our experiments.

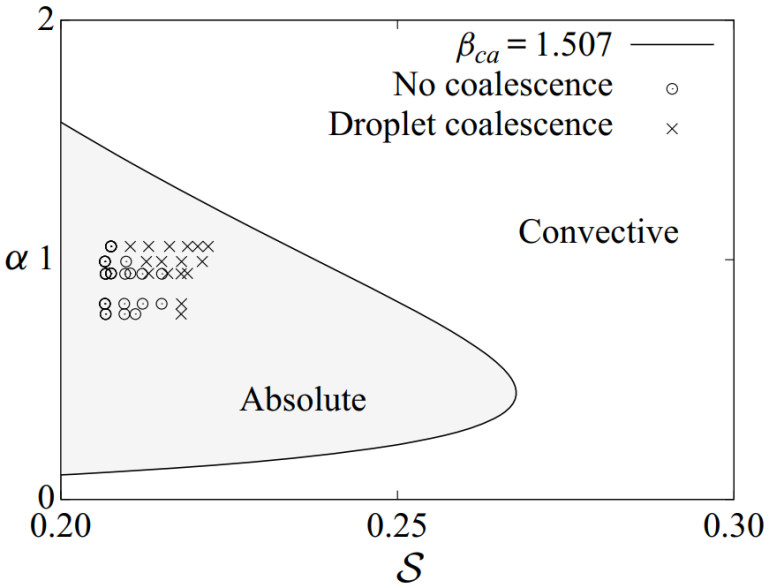

Figure 3.5 : The absolute and convective (A/C) instability regimes in the parameter plane of α and $\mathcal{S}$ predicted by (3.24) with $\beta_{CA} = 1.507$ and $A = 0$. The circle symbols represent experiments that are in RP regime and the cross symbols represent experiments with downstream bead coalescence.

3.7.1 Weakly non-isothermal films

Next, we show that for the weakly non-isothermal case, where the fiber is non-uniformly heated, both temperature-dependent viscosity and surface tension play an important role in determining the instability of the film. For simplicity, we consider the temperature $\Theta = O(\delta) << 1$ that linearly decreases in space in the leading order,

$$\Theta(x) = \delta\bar{\Theta}(x) = \delta(1 - \Theta_1 x) + O(\delta)^2, \quad \Theta_1 = \frac{1}{L} \ll 1. \quad (3.25)$$

This temperature $\Theta(x)$ satisfies $\Theta(0) \approx \delta$ and $\Theta(L) \approx 0$. Substituting (3.25) into the governing equation (3.14), for $\delta << 1$, we obtain the expansion for flux

$$q = (1 + \kappa\delta\bar{\Theta})\left\{M_0(h)\left(1 - \frac{\partial}{\partial x}[(1 - \omega\delta\bar{\Theta})(\mathcal{Z}(h) - h_{xx})]\right) + \delta\Theta_1 Ma M_1(h)\right\} + O(\delta)^2, \quad (3.26)$$

where

$$M_0(h) = \frac{h^3\phi(\alpha h)}{3\phi(\alpha)}, \qquad M_1(h) = \frac{h^2}{2}\frac{\psi(\alpha h)}{\phi(\alpha)}. \qquad (3.27)$$

For $\delta << 1$, the uniform film $\bar{h} = 1$ is a quasi-steady state of the system. Similar to the isothermal case, we apply the perturbation (3.17) to the governing equation and obtain the relation

$$\Lambda = \Lambda_0(k) + \delta\Lambda_1(k, x) + O(\delta)^2, \qquad (3.28)$$

where the leading-order term is given by

$$\Lambda_0(k) = k\frac{\alpha\phi'(\alpha)+3\phi(\alpha)}{3(1+\alpha)\phi(\alpha)} + ik^2\frac{1}{3(1+\alpha)}\left[-k^2 + \frac{\alpha^2}{\eta(1+\alpha)^2} - 3A\right], \qquad (3.29)$$

which is consistent with the dispersion relation (3.18) for the isothermal case for $\kappa = \omega = 0$.

The $O(\delta)$ term Λ_1 depends on both the wavenumber k and the spatial variable x,

$$\Lambda_1(k,x) = \frac{k}{3(1+\alpha)}\left(k^2 + \zeta'(1)\right)[i(-\kappa+\omega)\bar{\theta}(x)k + \theta_1(\kappa - 2\omega)] +$$

$$\frac{1}{1+\alpha}[(-\theta_1\omega\zeta(1)k + (\bar{\theta}(x)k + i\theta_1)\kappa)M_0'(1) + Ma\ \theta_1 k M_1'(1)]. \qquad (3.30)$$

This analysis reveals the combined effects of the temperature-dependent liquid properties on the film stability in the non-isothermal scenario through parameters κ, ω and Ma.

3.8 Results and discussion

3.7.1 Numerical simulations

We first perform numerical simulations of the PDE (3.14) to explore the influence of the thermal effects on the flow patterns. The dynamics near the nozzle are of interest because that is where the steepest temperature gradient occurs. To capture the near-nozzle dynamics, we set the initial conditions for the model (3.14) based on the nozzle geometry using a piece-wise linear profile for the film thickness h,

$$h(x,0) = \begin{cases} 1, & x > x_L \\ h_{IN} + (1-h_{IN})x/x_L & 0 \leq x \leq x_L, \end{cases} \qquad (3.31)$$

where $h_{IN} = (OD/2 - R^*)/H$ is determined by the difference between the nozzle outer diameter OD and the fiber radius R^*, and $x_L = 10$ is used for all simulations. We impose the following Dirichlet boundary conditions at the inlet $x = 0$ and the Neumann boundary conditions at the outlet $x = L$,

$$\begin{cases} h(0,t) = h_{IN}, & q(0,t) = 1/3\ x > x_L & \text{at } x = 0, \\ h_x(L,t) = 0, & h_{xx}(L,t) = 0 & \text{at } x = L. \end{cases} \qquad (3.32)$$

To numerically solve the model (3.14), we use a Keller-box-based centered finite difference method where the fourth-order differential equation is decomposed into a system of first-order differential equations:

$$\begin{cases} k = h_x, \quad p = \frac{\alpha}{\eta(1+\alpha h)} - k_x, \left(h + \frac{\alpha}{2}h^2\right)_t + q_x = 0, \\ q = M(h)\left(1 - \left[(1-\omega\Theta)\left(p + \Pi(h)\right)\right]_x\right) - \frac{h^2}{2}\frac{\Theta_x Ma}{1-\kappa\Theta}\frac{\psi(\alpha h)}{\phi(\alpha)}. \end{cases} \tag{3.33}$$

For most numerical simulations shown in this subsection, the boundary conditions (3.32) with $h_{\mathrm{IN}} = 1.46$ is used, which corresponds to the dimensional nozzle diameter OD = 1.55 mm. Moreover, we set $\alpha = 1.054$ and $\eta = 0.132$, which correspond to the dimensional fiber radius $R^* = 0.305$ mm and the flow rate $Q_{\mathrm{m}} = 8 \times 10^{-6}$ kg s^{-1} for silicone oil v50.

Starting from identical initial conditions (3.31), a comparison of the long-time dynamics of the model (3.14) with and without thermal effects is shown in Figure 3.6. Figure 3.6(a) shows that without thermal effects ($T^*_{\mathrm{IN}} = T^*_0$), the downstream dynamics ($x^* > 60$ mm) stabilizes into a sequence of equally-spaced travelling beads, which is a signature that the RP regime is attained. Figure 3.6(b) shows the response of the bead dynamics to the imposed temperature distribution $\Theta = \Theta_{\mathrm{I}}$ with the inlet temperature $T^*_{\mathrm{IN}} = 65$ ◦C and $\chi = 0.0085$. Close to the nozzle, the bead size and spacing are significantly smaller than those in Figure 3.6(a), which shows droplet compression in the high-temperature region. In the downstream region of 80 mm $< x^* <$ 160 mm in Figure 3.6(b), where the temperature is lower, the bead distribution becomes more irregular and the bead spacing is larger and more comparable to the bead spacing shown in Figure 3.6(a).

At $x^* \sim 73$ mm, we observe that two droplets collide and deform into a larger droplet. This type of bead coalescence happens repeatedly when a higher thermal gradient is present. Owing to the temperature difference between the upstream and downstream droplets, the upstream droplets

move faster down the fiber, repeatedly running into slower-moving beads in the downstream and initiating a coalescence cascade of droplets further downstream.

Figures 3.6(c) and 3.6(d) present the average bead spacing S_b and the bead velocity V_b over time as functions of the spatial variable x^*, respectively. For the $\Theta = \Theta^*_0$ case in the RP regime, the travelling beads have nearly constant spacing and velocity for $x^* > 60$ mm. For the $T^*_{IN} = 65$ °C case, the average spacing and velocity have a high spatial dependence; for $x^* < 60$ mm, both the average spacing and velocity slightly decrease as x^* increases. After the onset of bead coalescence at approximately $x^* = 65$ mm, large variations are observed in spacing and velocity as the downstream flow becomes irregular.

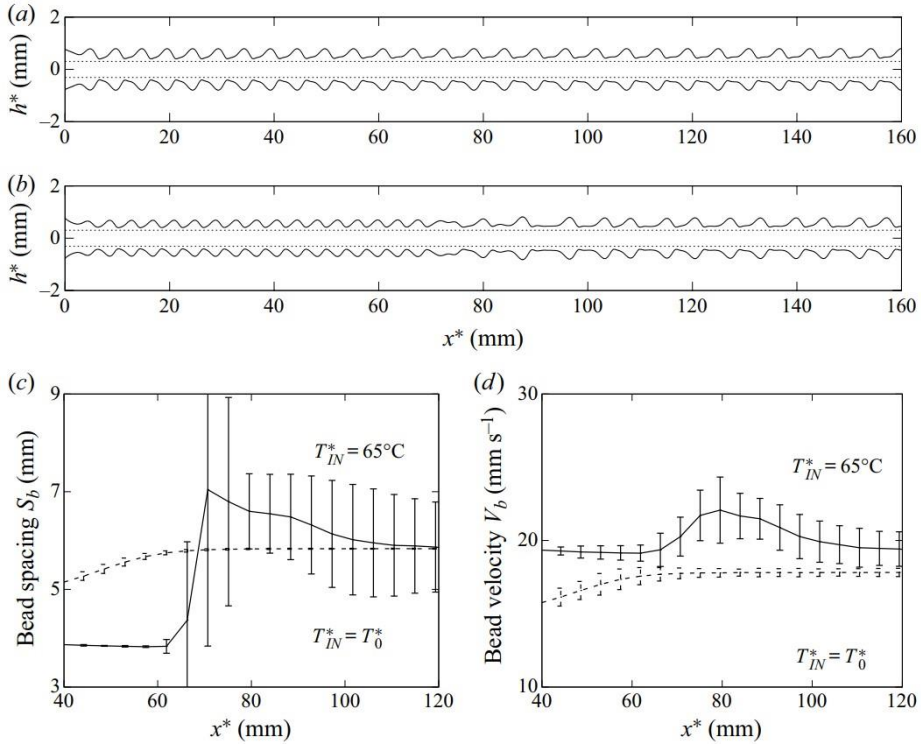

Figure 3.6 : A comparison of the dynamic solutions of (3.14) starting from identical initial conditions (3.31). (*a*,*b*) Transient profiles at time $t^* = 32.8$ s. In (a) without thermal effects ($T^*_{IN} = T^*_0$, $\kappa = Ma = \omega = 0$), the RP regime is reached. In (b) with thermal effects ($T^*_{IN} = 65$ °C), the dynamics involve compressed droplets near the inlet, bead coalescence and irregular bead patterns downstream. The average bead spacing S_b and bead velocity V_b are plotted against x^* in (*c*,*d*). System parameters are given by $\chi = 0.0085$, $\kappa = 0.543$, $Ma = 0.838$, $\omega = 0.111$, $\alpha = 1.054$ and $\eta = 0.132$. We set $\varepsilon_p = 0.05$ mm for the $T^*_{IN} = T^*_0$ case and $\varepsilon_p = 0.1$ mm for the $T^*_{IN} = 65$ °C case.

Figure 3.7 shows the influence of the film stabilization term in the droplet coalescence. For a higher value of the dimensional coating thickness ϵ_p, which corresponds to a larger parameter A in (3.20) and stronger film stabilization effect, we observe that the onset location of coalescence can move towards the inlet as ϵ_p increases (see Figure 3.7a). Moreover, Figure 3.7(b) shows that the film stabilization term enhances the upstream bead velocity, which is consistent with the observation for travelling wave solutions reported in Ji et al. [94].

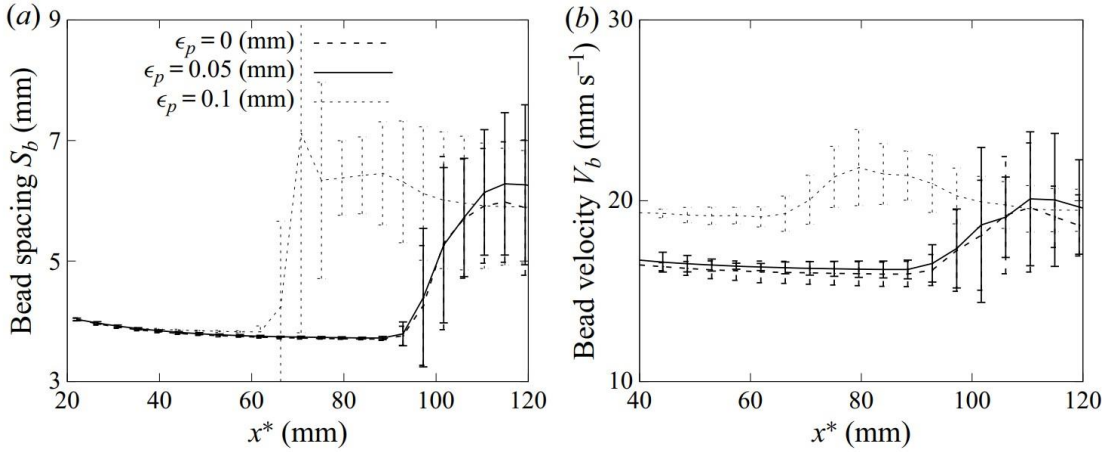

Figure 3.7 : Average bead spacing and velocity for T^*_{IN} = 65 ˚C with a varying stabilization parameter A in (3.20) for ϵ_p = 0, 0.05 mm and 0.1 mm, which shows that a larger value of ϵ_p can lead to the onset of droplet coalescence closer to the inlet and a higher upstream bead velocity. Other system parameters are identical to those used in Figure 3.6.

3.7.1 Experimental comparisons

To compare the numerical results against experimental observations and better describe the flow characteristics of liquid films, we constructed spatiotemporal diagrams from a sequence of numerical simulations. By tracing the peaks of the liquid beads, we plot the position of the peaks over time in Figure 3.8 to reveal spatiotemporal trajectories of the travelling beads. The slope of each trajectory indicates the travelling speed of each droplet, and the vertical distance between the trajectories represents the spacing between adjacent droplets. In Figure 3.8(a-d) where no

thermal effects ($T^*_{IN} = T^*_0$) are included, parallel trajectories are observed in both the experiment and simulation. This indicates that no droplet coalescence takes place, and the RP instability regime is attained. In the case where the inlet temperature $T^*_{IN} = 51\ ^\circ$C, the inter-bead spacings shown in both the experimental and numerical results are noticeably smaller than those in the $T^*_{IN} = T^*_0$ case. Moreover, the experiment with $T^*_{IN} = 51\ ^\circ$C shows that the coalescence of liquid beads starts to take place at $x^* \sim 90$ mm, which is reflected by two droplet trajectories coming together. A qualitatively similar pattern is also captured in the simulation where the bead coalescence occurs at $x^* \sim 92$ mm. When a higher inlet temperature is present, the thermally-driven droplet coalescence occurs further upstream. In the $T^*_{IN} = 65\ ^\circ$C case, the experimental spatiotemporal diagram shows that two droplets collide at approximately $x^* \sim 80$ mm, and in the simulation, cascades of droplet coalescence appear starting from $x^* \sim 72$ mm.

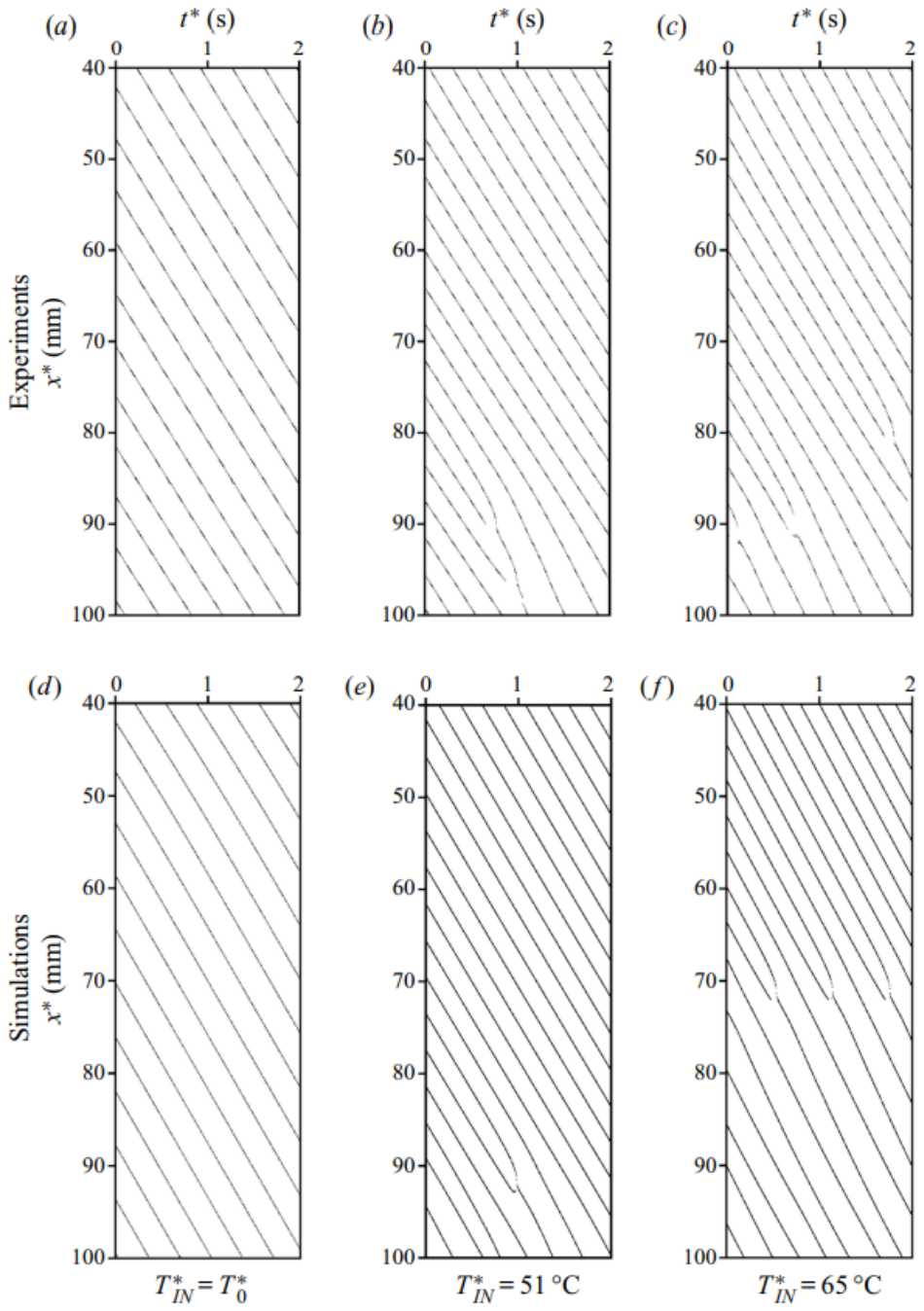

Figure 3.8 : Spatiotemporal diagrams for silicone oil v50 with the same liquid flow rate and fiber radius but different inlet temperatures from (a–c) experiments and (d–f) numerical simulations of (3.14). The fiber radius is $R^* = 0.305$ mm and the flow rate is $Q_m = 8 \times 10^{-6}$ kg s^{-1}. For the film stabilization term, $\varepsilon_p = 0.05$ mm is used for the $T^*_{IN} = T^*_0$ case, and $\varepsilon_p = 0.1$ mm is used for the $T^*_{IN} = 51$ ◦C and $T^*_{IN} = 65$ ◦C cases.

Figures 3.9 and 3.10 present the downstream droplet dynamics obtained by numerically solving the model (3.14) and the incompressible Navier–Stokes equations, and comparison with the experimental results. In Figure 3.9 where thermal effects are excluded ($T^*_{IN} = T^*_0$), the profile and inter-bead spacing of the steady train of beads obtained by both the model (3.14) and incompressible Navier–Stokes simulations are in good agreement with the experimental result. In Figure 3.10 where strong thermal effects (T^*_{IN} = 70 ˚C) are imposed, the experiment image exhibits upstream bead compression and a more irregular downstream droplet arrangement owing to the occurrence of bead coalescence. The transient solution profile of (3.14), as well as the Navier–Stokes simulation results, qualitatively captures a similar morphology but with a reduction of two orders of magnitude in computational time.

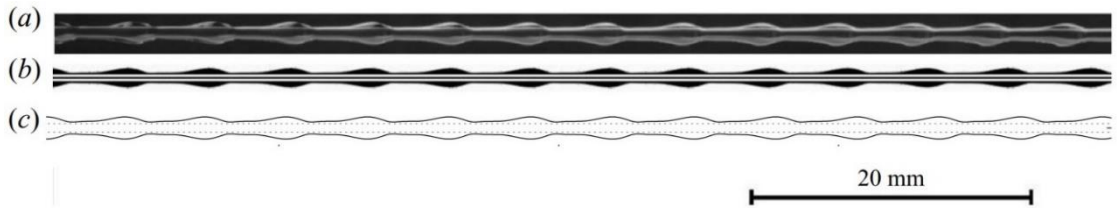

Figure 3.9 : The RP flow regime: profile comparison between (a) experiment, (b) incompressible Navier–Stokes simulation and (c) numerical simulation of the model (3.14) without thermal effects, $T^*_{IN} = T^*_0$, for silicone oil v50 starting from x^* = 53 mm away from the inlet.

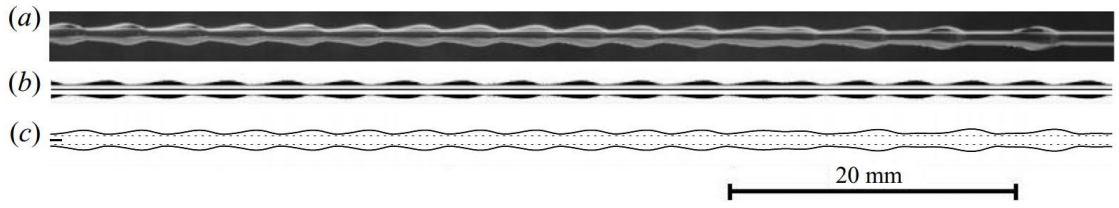

Figure 3.10 : Bead compression and coalescence: profile comparison between (a) experiment, (b) incompressible Navier–Stokes simulation and (c) numerical simulation of the model (3.14) for silicone oil v50 where the inlet temperature T^*_{IN} = 70 ˚C. The figures are shifted to align the locations to where two droplets collide.

The location of the onset of bead coalescence is also of interest. Figure 11 shows a comparison of the predicted locations of bead coalescence, based on numerical solutions of (3.14), against experimental observations with a varying inlet temperature for both low-viscosity silicon oil v20 and high-viscosity liquid v50. The onset location of coalescence is shown to become closer to the inlet as the inlet temperature increases, and the simulation results show good agreement with the experiments.

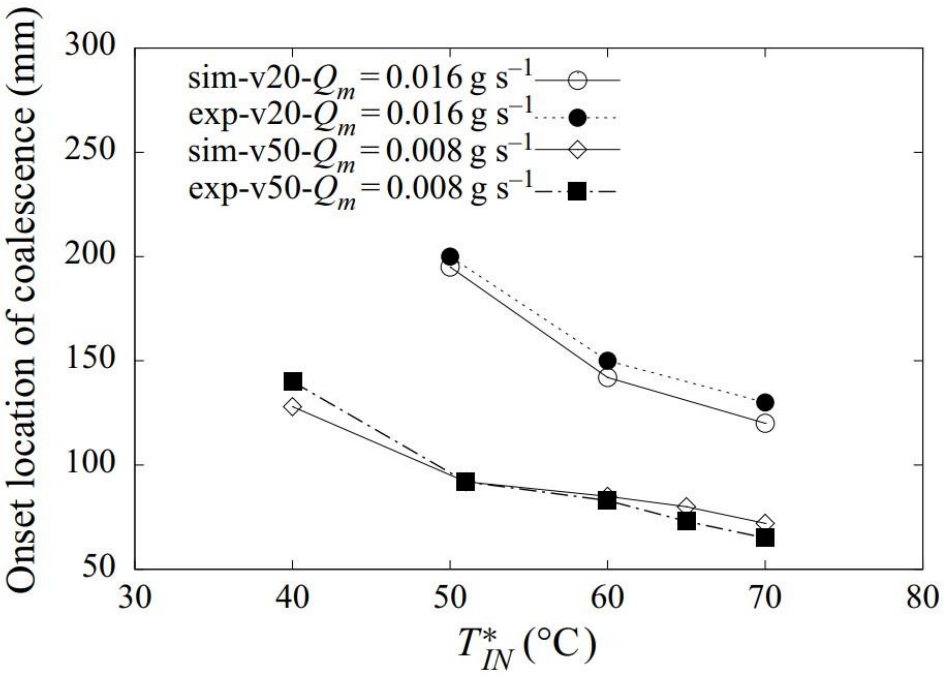

Figure 3.11 : Prediction of the location of droplet coalescence onset by numerically solving model (3.14) compared with the experimental results for silicone oil v20 at flow rate Q^*_m = 0.016 g s^{-1} and silicone oil v50 at flow rate Q^*_m = 0.008 g s^{-1}. The coating thickness ϵ_p = 0.1 mm is used for the stabilization term.

3.1 Summary

This study has focused on the investigation of the onset of thermally-driven droplet coalescence in the fiber coating dynamics. Through a set of experiments, we have demonstrated that droplet coalescence and irregular wavy patterns can be triggered by imposing a temperature

gradient along the fiber. We have presented a new lubrication model that incorporates spatially dependent viscosity and surface tension gradients arising from the imposed temperature field in the streamwise direction. This model addresses the roles of surface tension and viscosity gradients that cause bead coalescence cascades. Numerical simulations of our model show excellent agreement with experimental observations as well as incompressible Navier-Stokes flow simulations in terms of both droplet profiles and spatiotemporal diagrams.

CHAPTER 4

Film Viscosity Change on Fibers in String-Based Heat and Mass Exchangers

We present our study on the dynamics of liquid desiccant flow down a vertical thin cylindrical fiber where its properties are subject to change due to mass exchange with a wet air stream. We numerically and experimentally show that in addition to the inlet flow rate, fiber geometry, and nozzle geometry, change in the liquid properties along the string can lead to changes in the flow regime. As the desiccant concentration decreases, the absolute to convective instability transition mass flow rate also decreases. This is primarily due to the reduction in the viscosity which is characterized by the nondimensional Kapitza number. The experimental results show a promising dehumidification performance from the string-based exchanger which enables regime transition to occur only due to the vapor condensation on the liquid desiccant film. We reach a moisture removal rate of 16 $g/s/m^3$ from the exchanger while operating at ~43% effectiveness. We also compare the moisture removal rate of our string-based design as a function of efficiency with those of previously reported liquid desiccant-based air dehumidifiers. The present work demonstrates the efficient performance of compact, and scalable string-based mass exchangers where the effectiveness can be further improved by design optimization. Orr-Sommerfeld analysis is used to characterize and predict the absolute to convective instability transition for liquids such as Calcium Chloride aqueous solutions with intermediate viscosity values where inertia effect cannot be neglected. We also utilize incompressible Navier-Stokes

simulations that account for concentration-dependent liquid properties to investigate the bead dynamics. Both numerical simulations and Orr-Sommerfeld analysis show good agreement between the flow dynamics predictions and the experimental results.

4.1 Background

Thin liquid films flowing down a vertical fiber subject to thermal and mass exchange effects have been previously studied due to their importance in a variety of industrial applications, including dry and wet cooling systems and heat and mass exchangers for vapor, CO_2, and particle capture (Sadeghpour et al. 2019; Sadeghpour et al. 2021; Zeng, Sadeghpour, & Ju 2018; Zeng, Sadeghpour, & Ju 2019). Changes in liquid properties like surface tension and viscosity due to the presence of a temperature and/or concentration gradient influence the characteristics of these thin film flows (Ji et al. 2021). An improved understanding of the effect of the liquid property variation along fibers as a matter of mass exchange is crucial for systematic design of these systems.

It is generally known that when a liquid film coats a fiber, liquid beads may start to form due to the complex interplay of surface tension, gravitational, inertial, and viscous forces. Several research groups experimentally investigated and analyzed different flow regimes of these liquid beads flowing down a string. In an early study, a set of experiments was run to study the effect of the flow rate on the flow regime [15]. They qualitatively observed three different regimes of the interfacial patterns in the form of traveling liquid beads. At small flow rates, the isolated droplet regime occurs where widely spaced large droplets flow down the fiber separated by secondary small-amplitude wavy patterns. At higher flow rates, the Rayleigh-Plateau (RP) flow regime emerges where a stable train of droplets propagate at a constant speed. If the flow rate increases further, the convective instability regime emerges as collision of large droplets occurs in an irregular fashion. More recently, the effect of physical parameters, including liquid properties and the nozzle geometry, on the flow regime have been comprehensively investigated experimentally (Sadeghpour, Zeng, and Ju 2017; Gabbard and Bostwick 2021). The RP to convective flow regime transition can also be triggered by inducing a gradient to physical properties (i.e., surface tension/viscosity) of the liquid film along the fiber (Liu, Ding, and Chen 2018; Ji et al. 2021). In our

recent study, we investigate the effect of temperature gradient on the flow regime of a non-volatile viscous liquid, i.e., Silicone oil, flowing down on thin monofilament fibers (Ji et al. 2021). We observe regime transition occurs if the spatial rate of change of viscosity exceeds a certain threshold. In the present study, however, we focus on the effects of change in the concentration along the fiber on liquid properties and, eventually, on the flow regime.

Prior experimental works showed that the RP flow regime on a fiber offers a higher overall transfer coefficient compared to other flow regimes (Hattori, Ishikawa, & Mori 1994; Chinju, Uchiyama, & Mori 2000; Migita, Soga, & Mori 2005; Nozaki, Kaji, & Mori 1998). This proves maintaining a stable train of liquid beads is important for reliable heat and mass transfer performance in many applications. In this work, we first experimentally study the relationship between flow and fluid characteristics and mass transfer effectiveness for thin liquid films of Calcium Chloride ($CaCl_2$) solutions flowing on a single string exchanger against a counterflowing wet air stream in a confined space. We investigate the effect of solution concentration and liquid and air flow rates on the overall dehumidification performance. We then investigate the effect of concentration change along the fiber due to the mass exchange with humid air on flow properties and regime transition. To suppress the effect of temperature change, all the experiments are done at constant (room) temperature. In addition to the effect of liquid mass flow rate on regime transition, our study shows that for certain liquid and air inlet conditions, the flow no longer remains in the RP regime and can undergo a regime transition along the fiber. This regime transition due to the stream-wise liquid property change induced by the stream-to-stream mass exchange will be the focus of the present flow analysis.

An early study in 1990 demonstrated the effect of film thickness, compared to the fiber thickness, on the formation of instabilities on a fiber [124]. It was concluded that liquid bead formation will take place

only if the film thickness becomes large and quantitatively studied the conditions under which bead formation do not appear. A later study determined the critical film thickness, as a function of fiber radius (R_s) and capillary length (L_c), above which large liquid beads form and accelerate on a fiber [99]. This was done by stability analysis of axisymmetric flow of a viscous liquid on a fiber and defining a critical dimensionless saturation number (β_c) above which unbounded growth (i.e., convective regime) occurs. The study on the regime transition continued by a different group where it was shown that the absolute RP to convective regime transition in the inertia-less limit happens when β_c (or β^*) becomes larger than 1.507 [92]. This transition criteria reasonably applies to highly viscous liquids such as silicone oil v50.

Recently, (Ji et al. 2019) investigates a 1-D lubrication model that incorporates fully nonlinear curvature terms, slip boundary conditions and a film stabilization mechanism to simulate the train of beads on a fiber. For higher flow rates where inertial effects are no longer negligible, a few studies investigated systems of coupled equations for the film thickness and the flow rate based on the integral boundary layer approach [102]–[104]. This approach is further extended in [105] by introducing the film stabilization mechanism to address the influence of nozzle geometry on the downstream droplet dynamics.

There exist cases where the inertia effects can no longer be disregarded for predicting the absolute RP to convective regime transition. Hence, a linear stability analysis of the axisymmetric Navier-Stokes equations is conventionally used instead where the resulting equation, also known as the Orr-Sommerfeld (OS) equation, is a fourth-order ordinary differential equation for the complex stream function (Ψ). The solution to that equation also depends on the boundary conditions and the fiber thickness. The OS analysis shows that for a given film thickness, if the fiber size is very large or very small compared to the liquid film, the

flow becomes convective. It is also demonstrated that, if the fiber size exceeds a certain size determined by the capillary length, the flow will always be convective irrespective of the viscosity values. Finally, OS analysis shows that for a given fiber size, there exists a range of film thicknesses where the flow follows the absolute RP regime [92], [103].

Whereas many previous studies focus on the dynamics of viscous thin films with uniform properties flowing down fibers, fiber coating dynamics with liquid property change along the fiber have received less attention. For liquid films with non-uniform properties flowing on an inclined substrate, some earlier studies derived equations that incorporate the influence of temperature-dependent viscosity and surface tension [106], [107]. In one of our recent works, we propose a lubrication model that incorporates both temperature-dependent viscosity and surface tension. Using this model, we numerically simulate the downstream flow dynamics that forms bead coalescence due to the liquid property change along the fiber and obtain good comparison with experimental and incompressible Navier-Stokes simulation results (Ji et al. 2021). In the present work, in addition to considering the effect of streamwise liquid property change, we also focus on liquids with intermediate range of viscosities where transition lines precited for highly viscous liquids (such as silicone oil v50) or very thin liquids (such as water) no longer apply, and stability analysis needs to be done for each case individually. We work with a series of liquids with viscosity values ranging from water viscosity up to ~11 times higher. We conduct a series of OS analysis to predict the flow regime transition lines. These predictions are then compared against the experimental findings.

In the following sections, we first introduce the experimental setup and data used in the present study to fully analyze the dynamics of the thin film on the fiber. We also describe the methods we use to measure the properties of $CaCl_2$ solutions at different concentrations. Then we report our findings on the dehumidification performance of the single-string mass exchanger utilizing $CaCl_2$ solutions to dehumidify a saturated air stream. In the final discussions, we introduce numerical modeling, based on OS analysis, which we use to predict the absolute RP to convective regime transition and compare the results against our experimental findings. Flow transition lines are also defined in terms of three main dimensionless parameters: the liquid film aspect ratio ($\alpha = h_N / R_s$), the normalized string radius (R_s / L_c), and the Kapitza number (Ka).

4.2 Numerical simulation

We solve the transient problem for an incompressible Newtonian liquid discharging at a given constant mass flow rate (Q) from a cylindrical nozzle with an outer diameter of D_o and an inner diameter of D_i on a rough cotton fiber in a quiescent ambient air. The axis of symmetry is coincident with the cotton axis, along the direction of gravity. Both liquid and air properties are constant with time and uniform throughout the domain.

We use the PISO (pressure implicit with splitting of operators) algorithm to handle the pressure-velocity coupling [82], [117]. The solver [83] follows finite volume formulation to extract velocity and pressure fields at each interval. Further, we adopt the CSF model proposed by Brackbill et al.[84] where the effect of surface tension is introduced as an auxiliary body force in the momentum equations and the pressure staggering scheme (PRESTO) calculates the pressure on the faces (rather than the nodes). The wettability of the cotton fiber is applied by defining liquid-solid contact angle as a boundary condition. Note that, however, the defined

contact angle is for a stationary case. When a non-zero velocity field exists, the contact angle changes following the layout of the pressure field close to the contact line. The VOF method is used to track the liquid-air interface on a stationary Eulerian mesh[73].

We use an unstructured quadrilateral mesh of approximately 250000 elements with a time step size of 20 μs in our simulations. We conduct a mesh-independence and time step-independence study to verify that reducing the mesh size or time step by a factor of two results in less than 5% change in the predicted maximum meniscus heights. To help capture the contact line, we locally refine the mesh near the nozzle wall as well as on the fiber. We also include the roughness of the cotton thread while building the geometry to enhance the precision of the numerical simulations [1]. The simulation time is long enough to accurately capture steady periodic behavior, which is confirmed for each case by comparing the bead spacing of three consecutive beads over time. Finally, we include the effect of concentration gradient along the fiber using user defined functions for density, surface tension, and viscosity from Table 4.1.

Table 4.1: Experimental cases of $CaCl_2$ solution with different concentration (from 0% to 42% wt/wt), liquid and air mass flow rates, and liquid properties at 20 ˚C.

Solution concentration, kg_$CaCl_2$ / kg_solution (%)	Density, ρ (kg/m^3)	Surface tension, σ (mN/m)	Dynamic viscosity, μ (mPa.s)	Liquid desiccant mass flow rate, Q (g/s)	Counterflow air condition (Dry or wet)	Air mass flow rate (g/s)
42	1402.1	94.7	11.11	0.1 to 0.25	Dry & wet	0, 0.1, 0.2, 0.3
40	1367.8	93.3	9.04	0.1 to 0.25	Dry	0
38	1340.1	91.9	6.99	0.1 to 0.25	Dry	0
36	1322.2	90.6	5.60	0.1 to 0.25	Dry & wet	0, 0.1, 0.2, 0.3
35	1302.5	89.5	5.34	0.1 to 0.25	Dry	0
34	1290.3	88.4	4.98	0.1 to 0.2	Dry	0
32	1275.0	87.4	4.40	0.1 to 0.2	Dry	0
30	1252.1	85.8	3.58	0.1 to 0.2	Dry & wet	0, 0.1, 0.2, 0.3
0 (DI water)	997.8	72.1	1.14	0.06 to 0.15	Dry	0

Figure 4.1 compares incompressible Navier-Stokes solver results (top) with the pictures taken from actual experiments (bottom). The results show our numerical simulations can reasonably capture the dynamics of liquid desiccant flow on a rough cotton fiber for the intended range of concentration and flow rate. The small discrepancy between the results is believed to be due to the uncertainty in the property measurements.

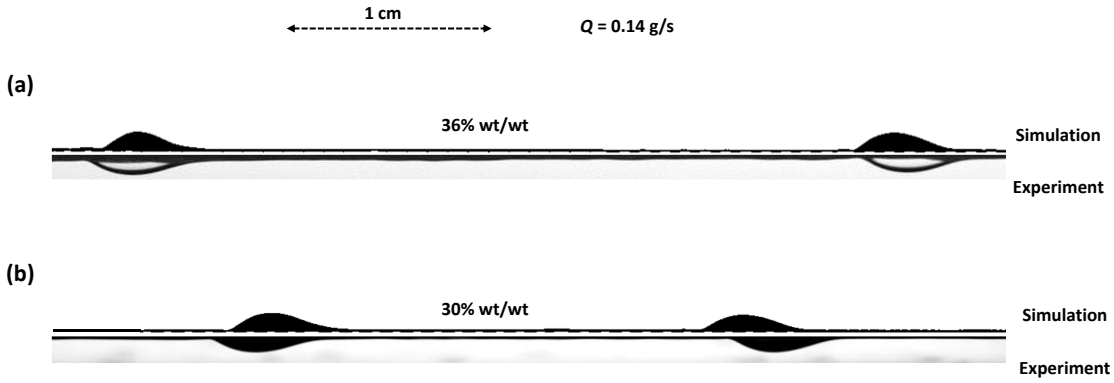

Figure 4.1: Comparison of the incompressible Navier-Stokes numerical simulation (top) liquid flow profile and the experimentally obtained results (bottom) for (a) 36% wt/wt and (b) 30% wt/wt $CaCl_2$ aqueous solutions. String diameter is 0.76 mm, the nozzle inner diameter = 1.22 mm, the nozzle outer diameter = 1.47 mm, liquid mass flow rate = 0.14 g/s, and average surface roughness = 0.04 mm.

Figure 4.2 shows the configuration of the train of beads in a separate simulation run where, unlike the cases shown in Figure 4.1, we impose a streamwise liquid property gradient. This is done by changing the desiccant concentration from 42% at the nozzle outlet (x = 0) to 40% at the end of the simulation domain (x = 15 cm) while keeping the inlet mass flow rate at the same level. Bead spacing and bead velocity increase as we move away from the nozzle outlet as a result of the streamwise viscosity reduction. This clearly shows how change in the liquid properties can result in nonuniformity in the bead pattern which can eventually lead to regime transition at a different flow rate. We further discuss the effect of property change on the

transition flow rate in later sections.

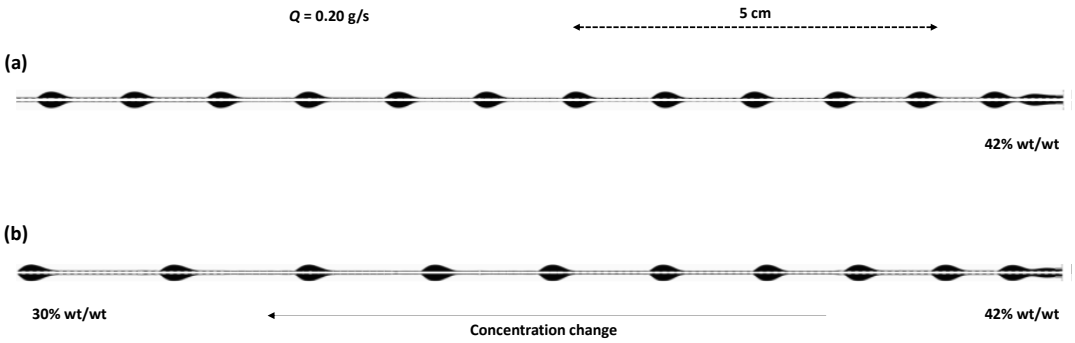

Figure 4.2: Comparison of the flow regimes obtained from numerical simulation for (a) when $CaCL_2$ at 42% wt/wt is flowing on the fiber without experiencing any concentration change and (b) when $CaCl_2$ starts to flow on the fiber at 42% wt/wt but the concentration decreases linearly with position to 30% wt/wt. Liquid mass flow rate is 0.20 g/s, and other physical properties are identical to Figure 4.1.

4.3 Experimental setup

Figure 4.3 shows a schematic of the experimental setup. A syringe pump (KDS-410, KD Scientific) is used to pump the $CaCl_2$ aqueous solution through a nozzle at a prescribed flow rate. The solutions are made by mixing DI water and laboratory grade anhydrous calcium chloride pellets with ~92% purity (also containing Potassium Chloride, Sodium Chloride, Strontium Chloride, and water). We use stainless steel nozzles with 1.22 mm inner diameter and 1.47 mm of outer diameter and a cotton string with 0.76 mm of thickness. However, to minimize the effect of nozzle on the transition mass flow rate, we use a different nozzle size for each concentration to compare the results with OS prediction analyses. Grippers are used in the setup for proper alignment and ensuring the nozzle and the string verticality. The cotton string is always under tension and secured to the bottom plate of the setup. A Plexi cylinder with 1.0 cm of inner diameter provides the confinement for the air flow. All the connections have been carefully investigated and inlet and outlet air flow rates have been checked prior to the experiments to

make sure there is no air leak from the system. $CaCl_2$ solution of different concentrations and DI water are used as the liquids. The liquid is collected and weighed using precision scale to verify the applied mass flow rates. The properties of the liquids at 20˚ C are listed in Figure 4.5.

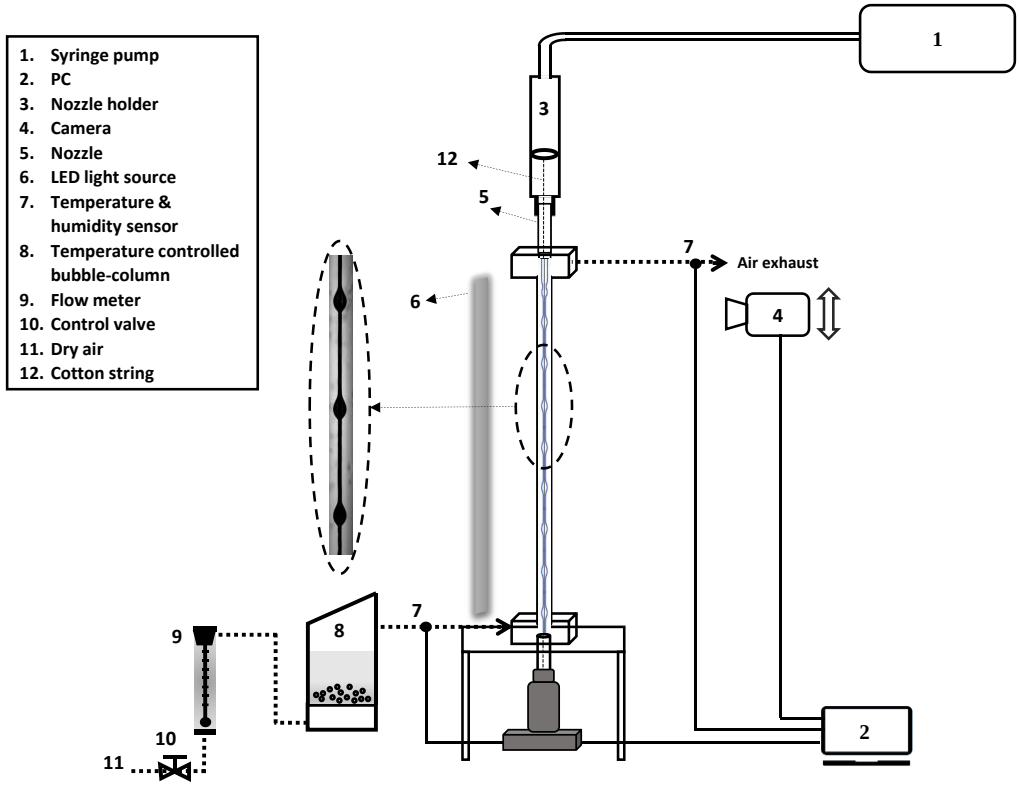

Figure 4.3: Schematic of the experimental setup. A bubble column is used to produce an air stream with 100% RH at the inlet of the setup. The temperature is almost uniformly constant in the device, and it is the same as the ambient throughout all the experiments.

A high-speed camera (VR-Phantom, AMETEK) mounted on an X–Y stage captures the liquid beads at 1000 frames/s. A light source and a light diffuser are used to improve image contrast. The uncertainty in the bead spacing and the bead velocity measurements are estimated to be ±0.05 mm and ±0.001 m/s, respectively. The videos are analyzed using ImageJ [87] to extract the bead shapes, bead spacing, and bead speed. The bead spacing is defined as the

distance between the tips or tails of two neighboring beads on the string. All the measurements shown are the averaged values.

Each dehumidification experiment case resumes for 25 minutes to ensure that the system is operating well beyond its transient state. Figure 4.4 shows the relative humidity (RH) values with time at the inlet and outlet of the device. Figure 4.4 (a) shows device's response right after switching from dry (0% RH) to wet (100% RH) air when there is no liquid flowing on the string, and Figure 4.4 (b) shows how the RH at the outlet decays with time just after the desiccant flow is enabled. Maximum RH difference between inlet and outlet when there is no liquid flow is 1%. All the experiments are conducted under a constant temperature of 20.5˚ C. No condensation was observed on the walls and hence, the RH difference between inlet and outlet air streams are considered to be solely due to the liquid desiccant flow.

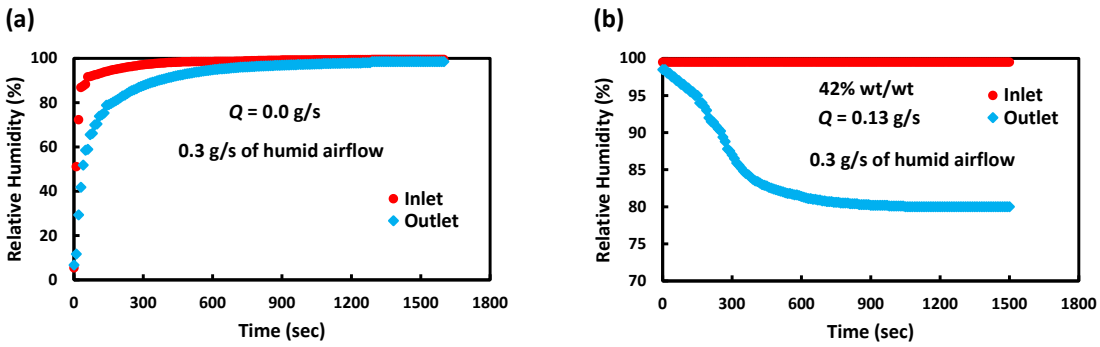

Figure 4.4: Relative humidity change with time at the inlet and outlet of the single-string mass exchanger while there is a 0.3 g/s of saturated airflow for two scenarios of (a) no desiccant flow, and (b) a 0.13 g/s stream of 42% wt/wt of $CaCl_2$ solution.

One-second-long videos are recorded for each case. The results show no appreciable differences in the bead shape, spacing and velocity during the recording time. A summary of the experimental conditions is presented in Table 4.1.

4.4 Results and discussion

4.4.1 Concentration dependent liquid properties

Liquid desiccant properties can change as concentration varies. In this work, we investigate the effect of concentration change on the density, surface tension, and viscosity of the liquid.

Densities are measured using a graduated cylinder and a precision weight scale. To characterize the concentration-dependence of the surface tension of our liquids, we use the pendant drop method where we use simple syringe and nozzle setups for each respective concentration to produce pendant droplets. We then implement commonly used image analysis techniques [125] using ImageJ and MatLab software and incorporate it into the Young-Laplace equation to extract the surface tension values. Equation (4.1) shows the Young-Laplace equation which can predict the shape of a static pendant droplet:

$$\frac{d\varphi}{ds} = -\frac{sin\varphi}{r} + \frac{\triangle \rho g z}{\sigma} + C, \quad (4.1a)$$

$$\frac{dr}{ds} = cos\varphi, \qquad (4.1b)$$

$$\frac{dz}{ds} = sin\varphi. \qquad (4.1c)$$

Here, C is a parameter that correlates with the excess pressure inside the liquid (pressure at the bottom of the droplet) and is determined as part of the iteration process for solving the problem. r is the radial and z is the axial coordinate, φ is the angle between the tangent line at the meniscus and the r axis, s is the curvilinear variable ($ds = (dr^2 + dz^2)^{1/2}$), ρ is the density, g is the gravitational acceleration, and σ is the surface tension.

The dynamic viscosity of solutions is measured using a simple force balance analysis on a stainless-steel sphere, with 0.5 mm diameter size, sinking with its terminal velocity in a column filled with the desiccant liquid:

$$F_g - F_b = C_d \, {}^1\!/_2 \, A \, \rho_l V_{sphere}{}^2, \quad (4.2)$$

where F_g is the gravitational force, F_b is the buoyancy force, ρ_l is the density of the solution, C_d is the drag coefficient, A is the projected area, and V_{sphere} is the terminal velocity of the sinking sphere captured by the high-speed camera. We use one of the proposed correlations that represents C_d as a function of Reynolds number [126]:

$$C_d = \frac{24}{Re} + \frac{2.6(\frac{Re}{5})}{1+(\frac{Re}{5})^{1.52}} + \frac{0.411(\frac{Re}{2.63\times10^5})^{-7.94}}{1+(\frac{Re}{2.63\times10^5})^{-8}} + \frac{0.25\,(\frac{Re}{10^6})}{1+(\frac{Re}{10^6})}. \quad (4.3)$$

Plots showing the relation between the liquid properties and concentration are included in Fig. 4.5. All the measurements are performed in a temperature-controlled lab. Maximum uncertainty in the measured density, surface tension, and dynamic viscosity values are estimated to be 16.5 kg/m^3, 1.2 mN/m, and 0.1 mPa.s, respectively.

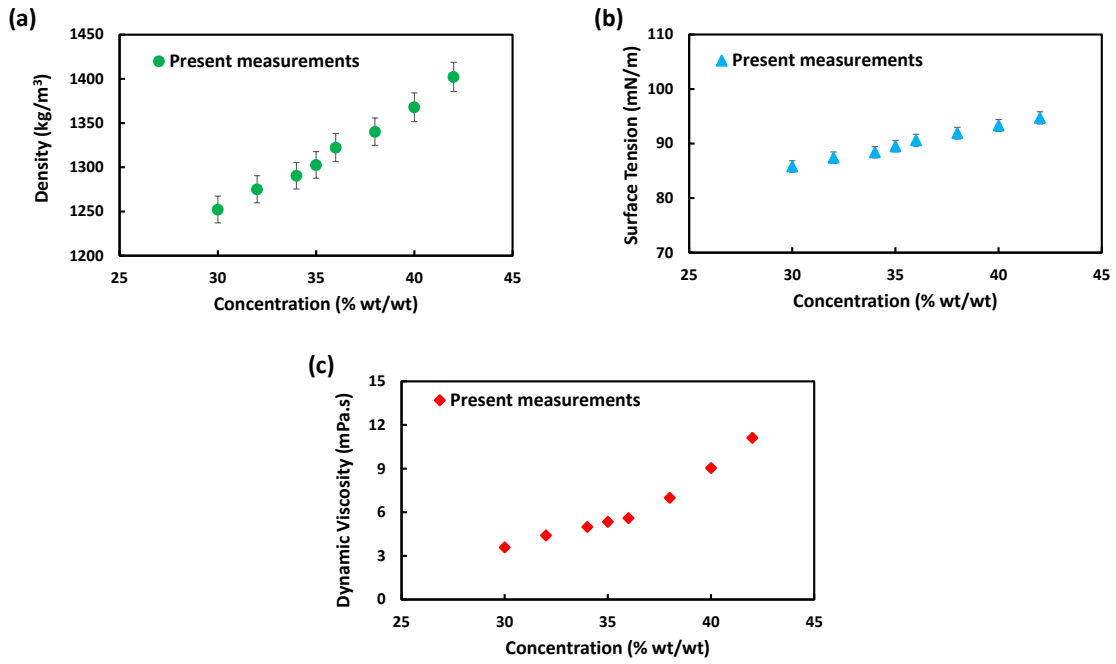

Figure 4.5: Data obtained for (a) density, (b) surface tension, and (c) dynamic viscosity of $CaCl_2$ aqueous solutions from experimental measurements.

4.4.2 Dehumidification performance

For each experimental case, the strong desiccant solution is supplied at a desired rate by the syringe pump to the nozzle setup, where then the solution continuously flows on the cotton string. Simultaneously, the air extracted from the dry air supply line first gets humidified to 100% RH by going through the bubble column humidifier then flows through the device in a counterflow manner with respect to the liquid flow. In all the experimental cases conducted in this work, the vapor pressure on the air side is higher than the vapor pressure of the liquid surface hence, the moist air always gets dehumidified to some level before exiting through the exhaust tube.

As mentioned earlier, the desiccant temperature as well as the moist air temperature is almost constant and the same (at 20.5˚ C) throughout the whole setup. The dehumidification performance is reported here under different air and desiccant flow rates and desiccant concentrations. We use two parameters to evaluate the performance of our device under different flow conditions: dehumidification effectiveness (ε_d), and moisture removal rate per volume of the device in g/s/m^3 (*MRR*). ε_d is defined as the ratio of actual dehumidification to the maximum possible dehumidification:

$$\varepsilon_d = \frac{\omega_{air,in} - \omega_{air,out}}{\omega_{air,in} - \omega_{desiccant,in}}, \quad (4.4)$$

where ω is the humidity ratio, subscripts "in" and "out" refer to inlet and outlet, and $\omega_{desiccant,in}$ is humidity ratio of an air stream with a vapor pressure the same as the vapor pressure at the surface of the strong desiccant supplied at the inlet. *MRR* on the other hand represents the rate of moisture removed from the air. We divide the values over the volume of the device in order to better compare the results with similar works in the literature (Pantelic et al. 2018; Kumar & Asati 2016; Ahmed & Kumar 2021; Naik & Muthukumar 2019). Therefore, we formulate *MRR* as:

$$MRR = \dot{m}_{dry\ air}\left(\omega_{air,in} - \omega_{air,out}\right) / Volume_{device}, \quad (4.5)$$

where $\dot{m}_{dry\ air}$ is the mass flow rate of dry air and $Volume_{device}$ is the volume of the cylindrical section.

A correlation proposed by Bouzenada et al. [131] gives the vapor pressure on the surface of the liquid desiccant solution as a function of concentration and temperature:

$$\ln(P_s) = A(\zeta) - \frac{B(\zeta)}{T_s + 111.96}, A(\zeta) = a_0 + a_1\zeta, B(\zeta) = b_0 + b_1\zeta, \quad (4.6)$$

where P_s is the vapor pressure in mmHg at the air-liquid interface, T_s is the solution temperature in Centigrade, and ζ is the concentration of the solution (mass of the salt to the mass of solution). The constants used are α_0 = 10.062, α_1 = 4.4674, b_0 = 739.828, and b_1 = 1450.96. The equilibrium vapor pressure is then converted to humidity ratio for implementing in Eqs. (4.4-4.5).

A total of 27 different scenarios by varying the air flow rate, the desiccant flow rate, and the desiccant concentration are tested and the results are compared in Figure 6. In Figure 6 (a) the device's effectiveness is presented as a function of the applied air mass flow rate for the three different desiccant concentrations used while the liquid mass flow rate is 0.16 g/s, and in Figure 6 (b) the desiccant concentration is kept at 42% wt/wt but the effectiveness is presented for three different liquid mass flow rates. We see that the effectiveness becomes larger as we decrease the air mass flow rate, increase the desiccant mass flow rate, and/or use a very strong desiccant. Figures 4.6 (c) and 4.6 (d) similarly show the *MRR* values for a variety of conditions where we notice increasing any of the experimental variables, i.e., air/desiccant mass flow rate and/or desiccant concentration, leads to a higher moisture removal rate.

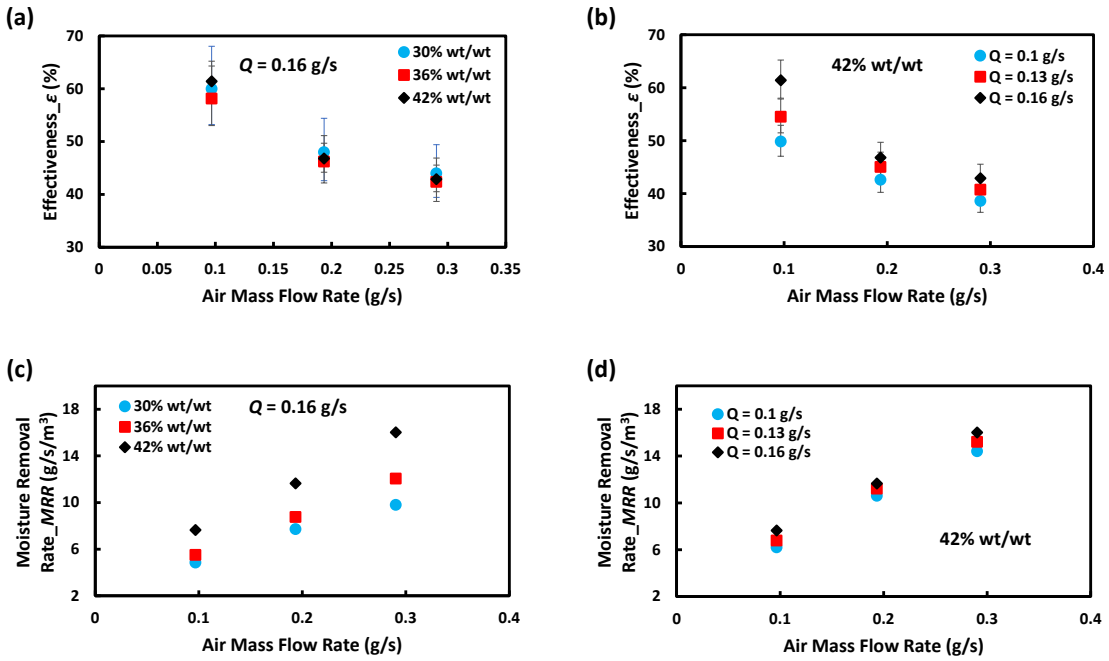

Figure 4.6: Single-string mass exchanger effectiveness with air mass flow rate for (a) different liquid desiccant concentrations and (b) different liquid mass flow rates. Also shown the exchanger's moisture removal rate (*MRR*) for (c) different liquid desiccant concentrations and (d) different liquid mass flow rates. Air is saturated (100% RH) at 20.5 ˚C at the inlet for all the experimental cases.

Since effectiveness for any mass exchanger highly depends on the inlet conditions, we instead decide to compare the string-based exchanger's *MRR* as a function of effectiveness with other dehumidification devices that use liquid desiccants in the literature. Figure 7 compares the maximum *MRR* versus ε values reported for different mass exchangers working with liquid desiccants while dehumidifying a wet air stream within a close range of inlet air humidity ratios (~15 to 21 g/kg). The string-based exchanger shows a promising performance by offering high *MRR* values at each operating effectiveness while dehumidifying wet air at temperatures as low as 20.5 ˚C. Note also that the current design is not optimized for performance and it is believed that a design similar to our previously-reported multi-string exchangers [1] can further enhance the dehumidification performance by enabling higher surface to volume ratio within the exchanger.

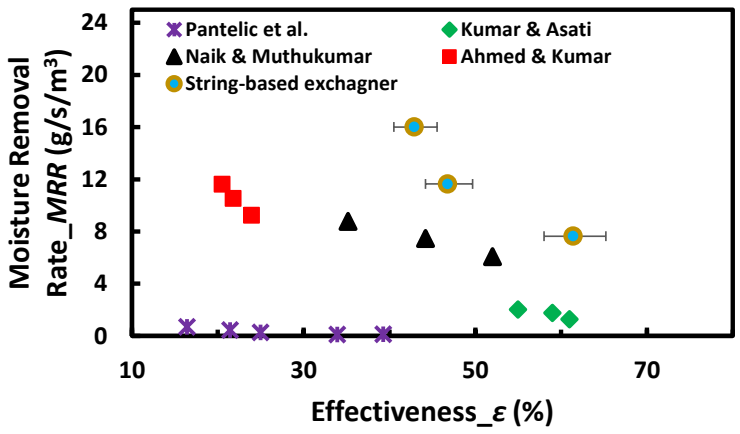

Figure 4.7: Dehumidification performance comparison in terms of *MRR* for different mass exchanger designs. Inlet air humidity ratios are all within 15 to 21 g/kg. All data can be found in (Pantelic et al. 2018; Kumar & Asati 2016; Naik & Muthukumar 2019; Ahmed & Kumar 2021).

4.4.3 Flow transition analysis using the Orr-Sommerfeld modeling

Here we investigate the effect of concentration on the transition flow rate using our experimental studies and applying the Orr-Sommerfeld (OS) analysis. The OS equation derived from linearization of the Navier-Stokes equation, shown in Eq. (7), is a fourth-order differential equation for the complex perturbation stream function amplitude $\psi_{(r)}$. Using a cylindrical coordinate with positive z pointing vertically downwards and r representing the radial direction on the fiber, we can write the non-dimensional OS equation as (Solorio & Sen 1987):

$$\left[(\Omega - u_z)\left(\mathrm{D}^2 - {k_r}^2\right) + \mathrm{D}^2 u_z\right]\psi = \frac{i}{k_r\ Re}\left(\mathrm{D}^2 - {k_r}^2\right)^2\psi, \quad (4.7)$$

where $\mathrm{D}^2 = r\frac{d}{dr}\left(\frac{1}{r}\frac{d}{dr}\right)$.

The form of the perturbation is given by $\psi_{(r,t)} = \psi_{(r)} \exp(i(kx - \Omega t))$, where $k = k_r + ik_i$ and $\Omega = \Omega_r + i\Omega_i$. Further, in Equation (4.7), $u_z(r)$ is the unperturbed fluid velocity, and $Re = U(h_N - R_s)/\nu$;

where U is the unperturbed fluid velocity at the free surface, h_N is the unperturbed thickness of the liquid film, and R_s is the average fiber radius.

A zero-group velocity (i.e., $v_g = d\Omega / dk = 0$) with $\Omega_{0i} > 0$ identifies the onset of the absolute instability [1]. We also add the effect of finite roughness of the cotton thread surface by introducing a Navier slip condition at the fiber surface ($r = R_s$), shown in Equation (4.8), where λ is the effective negative slip length. This approximation, also known as the Navier friction condition, regulates the no-slip condition on rough surfaces (Miksis & Davis 1994). We use $\lambda = 0.04$ mm for inducing the roughness effect in current study.

$$\frac{d\psi}{dr} + \lambda \frac{d^2\psi}{dr^2} = 0 \qquad (4.8)$$

We perform the OS analysis for a range of string radius values, 0.08 mm $\leq R_s \leq$ 0.53 mm, and compare the predicted critical flow rates for different concentrations of 42%, 36%, 30%, and 0% wt/wt in the plot shown in Figure 8. In this plot the horizontal axis represents the normalized string radius (R_s / L_c), and the vertical axis represents the liquid film aspect ratio ($\alpha = h_N / R_s$). Each prediction line, in fact, corresponds to a specific Kapitza number ($Ka = (\sigma\rho^{1/3}) / (g^{1/3}m^{4/3})$) where its variation in present work is primarily due to viscosity change and the rest of the liquid properties have much less significant impact. Our results show that the OS analysis predicts the transition flow rate increases monotonically by increasing the viscosity (or decreasing the Ka) which is consistent with our experimental observations (solid symbols in Fig. 4.8). This also means that even by keeping the mass flow rate at a constant level, the flow regime could change on the fiber if the liquid viscosity changes. We experimentally investigate the possibility of regime transition due to concentration (i.e., viscosity) change in the following sections.

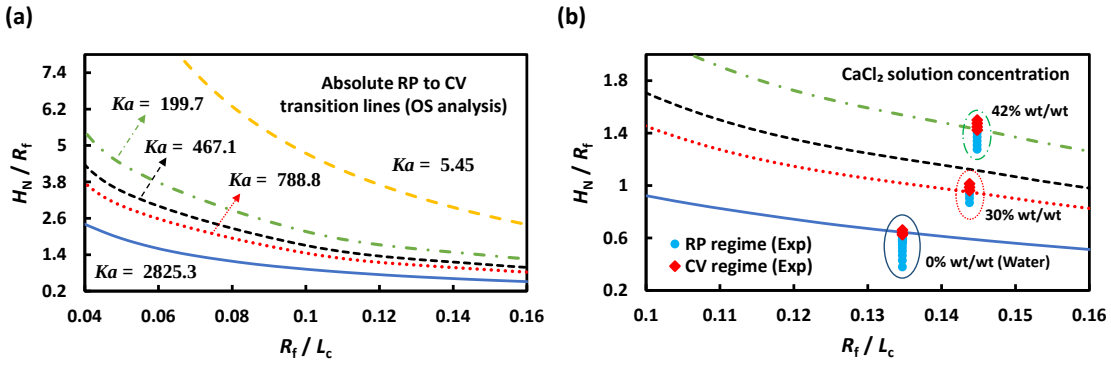

Figure 4.8: The absolute and convective instability regimes in the parameter plane of the liquid film aspect ratio ($\alpha = h_N / R_s$), the normalized string radius (R_s / L_c). The lines correspond to the OS solutions with roughness-induced boundary slip for a wide range of *Ka* numbers. The circle and diamond symbols in (b) represent the absolute RP and convective instabilities in the experiments, respectively.

Note that, by using appropriate nozzle sizes we cancelled the effect of nozzle on the flow regime during the experiments. We basically choose a nozzle size that is large enough to not let jetting happen in the vicinity of the nozzle outlet for the range of the flow rates applied. The nozzle size, on the other hand, should not be very large to skip the absolute RP regime. For more information on the effect of nozzle on flow regimes of liquid films on fibers please refer to [105].

4.4.4 Effect of desiccant mass flow rate and concentration on flow dynamics

All the experimental cases shown hereafter use a constant nozzle size in order to implement a better comparison.

Figure 4.9 compares bead spacing and bead velocity for different $CaCl_2$ solution concentration values when no air flow is applied. Both bead spacing and bead velocity generally decrease as we increase the viscosity. This trend, however, might change near the RP to convective transition flow rates as the bead spacing and bead velocity reach their minimum values just before the transition.

This plot also clearly shows the direct relation between viscosity and the transition mass flow rates.

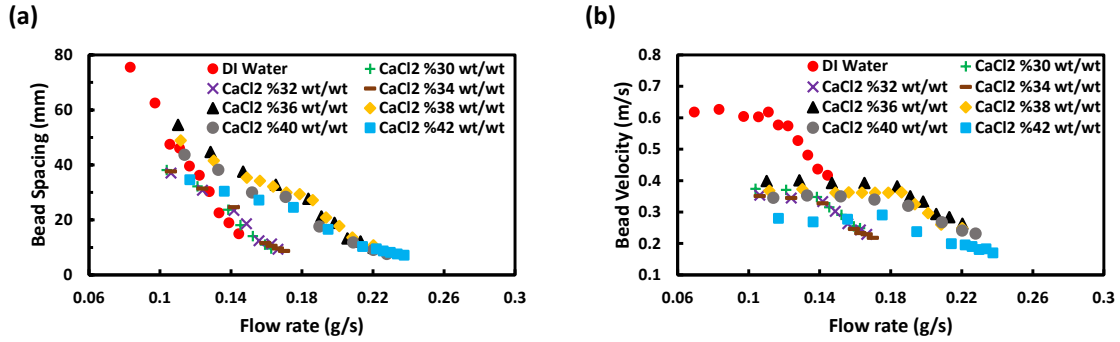

Figure 4.9: (a) Bead spacing and (b) bead velocity of the train of beads on the cotton fiber as a function of liquid desiccant mass flow rate and concentration.

Figure 4.10 shows how the bead size changes with concentration when the flow rate is kept constant at Q = 0.12 g/s (Fig. 10 (a)), and its variation with mass flow rate when the concentration is constant at 42% wt/wt (Fig. 10 (b)). Bead diameter increases by ~15% when increasing the concentration from 0% (i.e., DI water) to 42% (i.e., almost saturated solution) which is mainly due to the increase in surface tension [5].

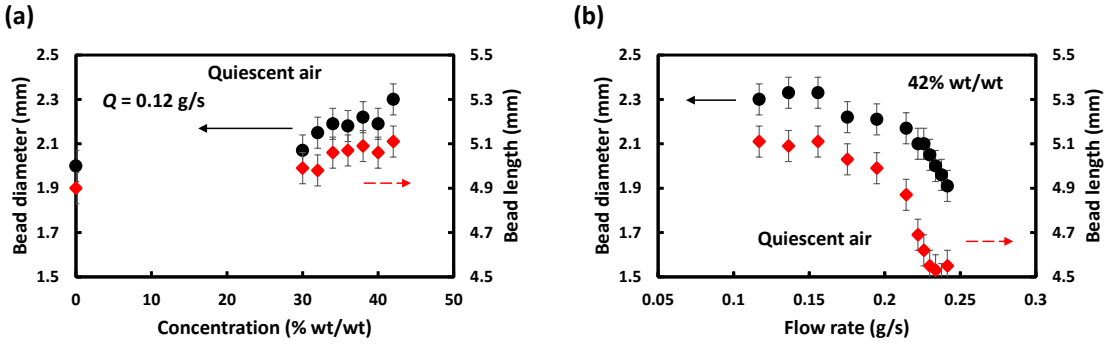

Figure 4.10: Variation in the bead size with (a) desiccant concentration while the liquid flow rate is fixed at Q = 0.12 g/s and (b) with liquid flow rate while the desiccant concentration is 42% wt/wt.

4.4.5 Effect of condensation on flow dynamics and flow regime

In order to study the effect of concentration change on the liquid desiccant flow characteristics, we subject a wet air stream to the exchanger and compare the findings with a similar set of experiments where a dry air stream is used instead. We basically pick the desiccant concentration (42% wt/wt) and the air mass flow rate (0.3 g/s) and keep them fixed while we record the flow regime for different desiccant mass flow rates under both dry air and wet air scenarios. The saturated air at room temperature, as discussed in the experimental section, is produced when the dry air goes through the bubble column being fed by a water bath. We, however, have checked the effect of air flow rate on the train of beads and the transition and found no alteration in those parameters for the range of air flow rates applied here. Figure 4.11 (a) and (b) show how the bead spacing and bead velocity change, respectively, as we switch from dry to wet air. Both bead spacing and bead velocity increase when the liquid desiccant flow gets in contact with the wet air. This is due to the slight decrease in viscosity of the liquid stream after starting to absorb water vapor from the wet air stream. However, the bead spacing ultimately becomes smaller compared to the dry air case as we get close to the transition mass flow rate and ultimately leads to flow transition at a lower mass flow rate. Figure 4.11 (c) and (d) also show how the bead shape changes where the increase in bead velocity due to concentration reduction results in having beads with larger aspect ratios.

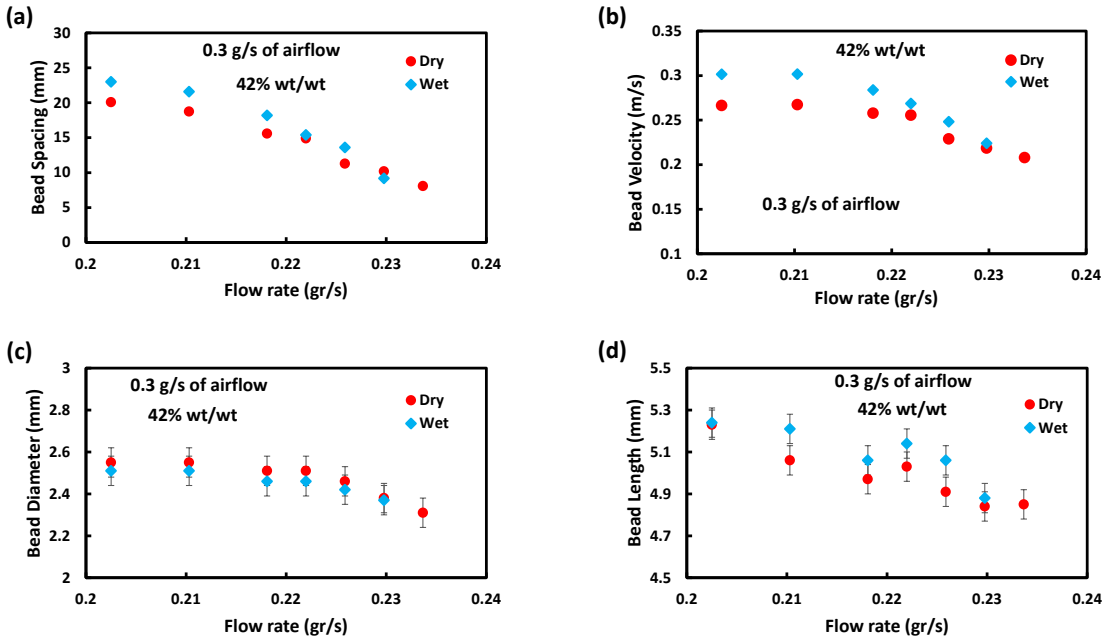

Figure 4.11: (a) Bead spacing and (b) bead velocity change with liquid flow rate under wet or dry air stream at 0.3 g/s. Also shown the variation in the (a) bead diameter and the (b) bead length with liquid flow rate for the same cases. All data represent liquid desiccant at 42% concentration.

Figure 4.12 shows spatiotemporal diagrams of the train of beads with 42% wt/wt concentration at different desiccant mass flow rates under both wet and dry airflow conditions. As we increase the liquid mass flow rate, the slope, which represents the bead velocity, does not change much but the distance between the lines (representing the bead spacing) decreases. More importantly, the wet air flow causes the RP to convective regime transition to occur at a lower mass flow rate compared to the dry air flow which can be noticed from the irregularities in the spatiotemporal lines at 0.2337 g/s of desiccant mass flow rate. This means that the wet air flow has resulted in ~ 3.2% reduction in the transition mass flow rate compared to the dry airflow condition. The small change in the transition mass flow rate is because of the very slight decrease in the concentration of the liquid desiccant (~1% wt/wt). Also note that these frames start at a distance of ~15 cm from the liquid

inlet.

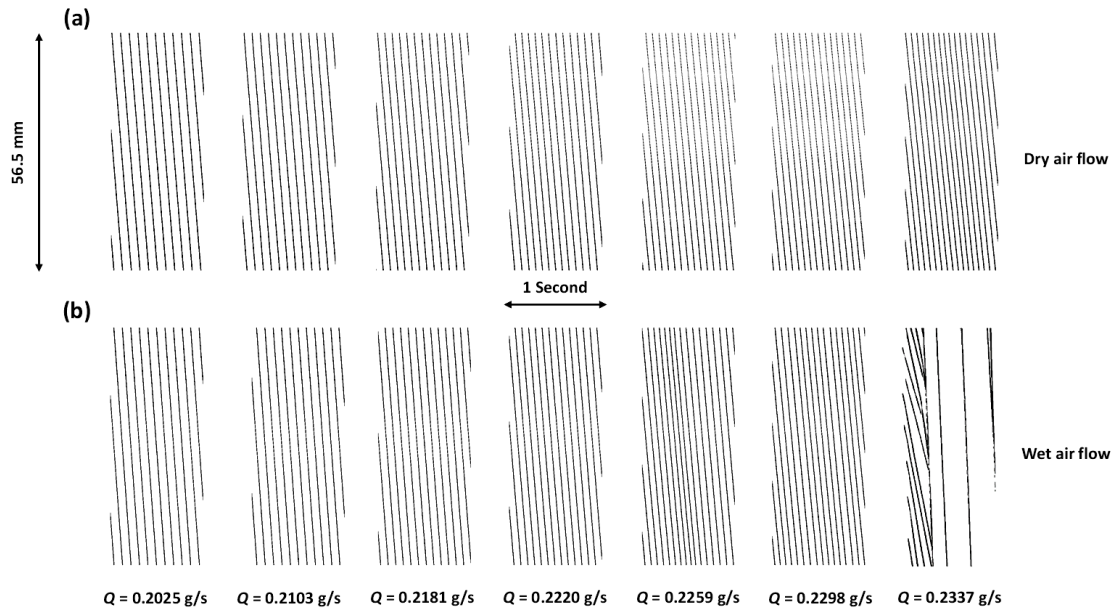

Figure 4.12: One-second-long spatiotemporal diagrams of 42% wt/wt $CaCl_2$ desiccant beads over a 56.5 mm range on the cotton fiber. The air stream flows at 0.3 g/s in a (a) dry condition (0% Rh) and (b) wet condition (100% RH) and the results show steady state condition. All the frames start at a distance ~15 cm from the liquid inlet.

4.5 Summary

We conduct a systematic experimental and numerical study on the flow regime transition of liquid films on thin fibers induced by concentration change. We make Calcium Chloride aqueous solutions at different concentrations to create a set of liquid samples with different properties and utilize them as liquid desiccants in our single-string mass exchanger. We perform the study over a range of intermediate viscosity values (1.14–11.11 mPa.s) and up to absolute RP to convective instability transition mass flow rates (0.06–0.25 g/s). Other liquid properties such as density (997.8–1402.1 kg/m3) and surface tension (72.1–94.7 mN/m) change less significant. The range of the dimensionless parameter considered in the present study (i.e., the Kapitza number) is for $199.7 < Ka < 2826.1$. In general, as the viscosity increases (or as the Ka decreases), the absolute

RP to convective transition mass flow rate becomes smaller. Through a set of experiments where we use the liquid desiccants to dehumidify a wet air stream, we demonstrate that irregular wavy patterns can be triggered by imposing a concentration gradient along the fiber. Further, Orr-Sommerfeld analysis and incompressible Navier-Stokes simulations are performed to predict both flow regime transition and train of beads dynamics, respectively. The numerical results show good agreement with our experimental observations.

To quantify the performance of our string-based liquid desiccant dehumidifier, the moisture removal rate and the effectiveness is experimentally determined under various conditions. Consistent with similar works, we show that as the air mass flow rate increases, the moisture removal rate increases but the exchanger effectiveness decreases. Increasing the liquid desiccant flow rate can enhance both moisture removal rate and the effectiveness and increasing the desiccant concentration to near saturation increases the moisture removal rate due to inducing a higher vapor pressure difference along the device. We reach a moisture removal rate of 16 $g/s/m^3$ with the presented string-based exchanger while operating at ~43% effectiveness. We believe this performance can be easily enhanced by scaling up and utilizing a more optimized design. In this connection, additional research efforts are also necessary to systematically investigate the effects of practical parameters, such as the air and the liquid streams temperatures, which were not examined in the present work.

CHAPTER 5

Highly Efficient and Economic Multi-String Heat/Mass Exchangers for Desalination Based on the Humidification-Dehumidification Process

We designed, constructed, and tested an innovative low-cost lightweight heat and mass exchanger technology to enable economic and energy efficient brine concentration and desalination via a humidification-dehumidification (HDH) process. By increasing energy efficiency while driving down capital and operating costs, our technology enables modular mobile desalination systems capable of treating a wide variety of feed waters. These include hypersaline oil and gas produced waters, seawater desalination brines, and other hypersaline waters, which cannot be treated by reverse osmosis (RO) and traditional thermal desalting technologies are too expensive and energy intense. We conducted a series of numerical optimization problems in order to find a design that offers very high Gained Output Ratios (*GOR* >7 values) while taking advantage of our multi-string exchanger technology and found that a 3.5-meter-tall system with two intermediate extracted airlines between the humidifier and the dehumidifier gives a *GOR* of 7.5 and recovers about 9.5% of the brine feed in a single pass. Due to some practical and space limitations, however, we decided to proceed with an alternate, more compact (~2.2 meters-tall), design that incorporates a single extraction line and obtained promising experimental results (*GOR* ~ 2.9, *RR* ~ 7.5%, STEC ~ 220 kWh/m3, SEEC ~ 2

kWh/m3) that are within 20-25% of our numerical predictions.

We leverage our previous work on novel string-based, direct-contact heat and mass exchangers to develop and experimentally validate rigorous thermodynamic and heat/mass transfer models for humidification and dehumidification. We then use these models to systematically optimize the design of an integrated HDH brine concentration and desalination system. A lab-scale system prototype is constructed, and performance is characterized using simulated feed water streams at influent salt concentrations up to 250,000 ppm to validate the design and assess scalability for future commercial applications. Results presented in this report will benefit future designs and deployments of HDH desalination plants.

5.1 Background

Desalination systems can generally be divided into three groups: membrane-based systems, thermally driven systems, and desalination systems that use other innovations, e.g., electro-dialysis (ED) or mechanical vapor compression (MVC), for desalinating purposes [23]. The desalination systems that primarily rely on membrane filtration generally consist of, membrane distillation, reverse osmosis, and forward osmosis [1], [24], [25]. Thermally driven systems are mostly based on solar still, solar chimney, humidification-dehumidification (HDH), multi-stage flash (MSF) evaporation, and multi-effect distillation (MED) [24], [26]–[28]. Reverse osmosis (RO)[29], [30], a membrane-based desalination technique, has been widely used for desalination of sea water, brackish groundwater and treatment of waste-water in large scales and it is considered the leading and the most optimized membrane-based desalination process [31]. Typical RO plants in a multi-stage design provide water recovery of 50%. However, the general performance and efficiency depends on the feed characteristics, feed salinity, pre-treatment, design configuration, and brine disposal considerations [32], [33]. Therefore, high consumption of electricity and increased pre-treatment and membrane maintenance cost due to membrane fouling, and their relatively low limits on the acceptable salinity of feed water are major drawbacks of this kind of desalination systems [30], [31], [34], [35]. In other words, system performance is highly dependent on its filtration parts, and therefore, demands a high degree of maintenance due to membrane fouling and scaling to keep its productivity at a reasonable level.

Thermal desalination techniques such as HDH have become an appealing technology for brine concentration during the past few decades as they are more fit to run with a renewable energy source (i.e., solar energy), can process brine having salinity much greater than seawater, and can be utilized in more compact and portable platforms compared to the desalination systems

that are purely relied on membranes. MSF and MED processes are among the most reliable and very well-known thermal desalination techniques. MSF desalination plants, for instance, were being utilized by about 21% of the world's total installed or contracted desalination systems at 2015 [36]. However, MSF process is highly energy-intensive where the energy consumption easily exceeds 20 kWh per meter cubed of produced fresh water [37], [38].

There are performance parameters that are frequently used by researchers to quantify and compare the performance of thermal desalination systems. Here, we introduce two important factors. A parameter most widely used to quantify the performance of thermal desalination systems is the gained output ratio (*GOR*), defined as the ratio between the latent heat of condensation and the net thermal energy input (Eq. 5.1). Where it indicates how much fresh water is being produced per unit heat applied to the system.

$$GOR = \frac{\dot{m}_{pw} h_{fg}}{\dot{Q}_{in}} \qquad (5.1)$$

$\dot{m}_{pw}$ is the rate of purified water production, h_{fg} is the latent heat of vaporization, and $\dot{Q}_{\mathrm{in}}$ is the rate of heat being applied to the device. Another important parameter that is commonly used in the literature is the recovery ratio (*RR*). *RR*, as defined in Eq. (5.2), is the ratio of the amount of water produced ($\dot{m}_{\mathrm{pw}}$) per kg of brine feed ($\dot{m}_{\mathrm{b,in}}$). In a desalination system working with a closed air loop, once the steady-state condition is reached, evaporation and condensation happen at the same rate, hence *RR* can be calculated using the rate of either evaporation or condensation.

$$RR = \frac{\dot{m}_{pw}}{\dot{m}_{b.in}} \qquad (5.2)$$

Note that, since *GOR* depends on the rate of freshwater production, having a higher *RR* may also result in having higher *GOR*. However, *GOR* also depends on heat recovery and as more heat is recovered from the hot product, less energy (i.e., $\dot{Q}_{in}$) would be needed to run the system at the same water production level.

As we mentioned earlier, nowadays the most abundant thermal desalination technology in the world is MSF, where similar to other thermal processes such as MED, it can produce high quality distilled water [134]. However, relatively high total energy consumption (due to high brine temperature), high capital costs (due to relatively large number of stages), and the need for their frequent maintenance have put a delay in their further commercialization [135]. On the other hand, ease of access to solar energy in some regions around the world has attracted much interest towards coupling thermal desalination systems with solar energy harvesting plants in order to establish sustainable desalination sites that are almost independent of fossil fuels and can be relied on as a stable source of clean water [136]–[138]. However, for making this energy transition possible we also need to address the low energy efficiency of thermal desalination systems due to limited availability of space and sunlight around the globe.

5.1.1 Humidification-Dehumidification (HDH) desalination

Humidification and dehumidification (HDH) thermal desalination technique is a better choice for small to medium scale and mobile desalination and water treatment applications (Giwa et al. 2016; Farid et al. 2003; Parekh et al. 2004) since it can operate under a wide variety of conditions using a low-grade heat source (e.g. a solar panel) and its simple construction needs. An HDH unit mimics our natural water cycle by first humidifying a carrier gas (i.e., air) and then

condensing water vapor to produce distilled water (see Fig. 5.1). Hence, the HDH system operates with evaporation and condensation cycles that consists of an air stream, being driven via either natural or forced convection, and a water stream [42]. It can be further classified based on the stream that is being heated in the system: air-heated or water-heated. For either heating scenario, four different approaches are available depending on whether each fluid stream is undergoing a closed cycle or an open cycle configuration [23]. Figure 5.1 qualitatively shows how a closed-air open-water (CAOW) water-heated HDH cycle works which have been investigated through many numerical and experimental research. The *RR* is, generally, found to be much lower for the HDH system than conventional systems. This might seem like a drawback for the overall performance of an HDH system. However, using a multi-stage or the so-called "feed-and-bleed" design can solve the problem and *RR* can be further improved until a limit set by the device's salinity tolerance. Another drawback for HDH systems is the need for dehumidifiers with very large surface areas. This is mostly due to the presence of non-condensable gases while working under atmospheric conditions which makes the condensation process less efficient. Hence, designing and utilizing an efficient dehumidifier is crucial for any HDH system to make them more affordable and reduce the final cost of freshwater production.

A preceding study constructed three HDH units each with a different size and material following the CAOW water-heated desalination approach [139]. The heat and mass transfer characteristics were quantified as a function of air and water mass flow rates, inlet temperatures, and surface areas. Air circulation via natural convection was found to be sufficient for running the system. Various packing materials and design structures have been tested in the recent years. To name a few: cellulose papers with honeycomb structure for humidification and cylindrical shell with coiled copper tubes for dehumidification [140], fin-tube heat exchanger for

dehumidification and an evacuated tube solar collector for providing the necessary heat [141], packed-bed cooling tower made of polypropylene for humidification and plate and tube dehumidifiers from the same material [142], a cooling tower with inclined wooden slats packing for dehumidification [143], galvanized steel plates for dehumidification [40], plate-fin and tube heat exchanger for dehumidification [144], and using permeable membrane between humidifier and dehumidifier for continuous airflow adjustment [145]. The maximum reported *GOR* for an HDH system in the literature is 8 where the proposed design takes advantage of multi-effect humidification to reduce the stream-to-stream temperature difference and enhance the energy efficiency in the system [145], [146].

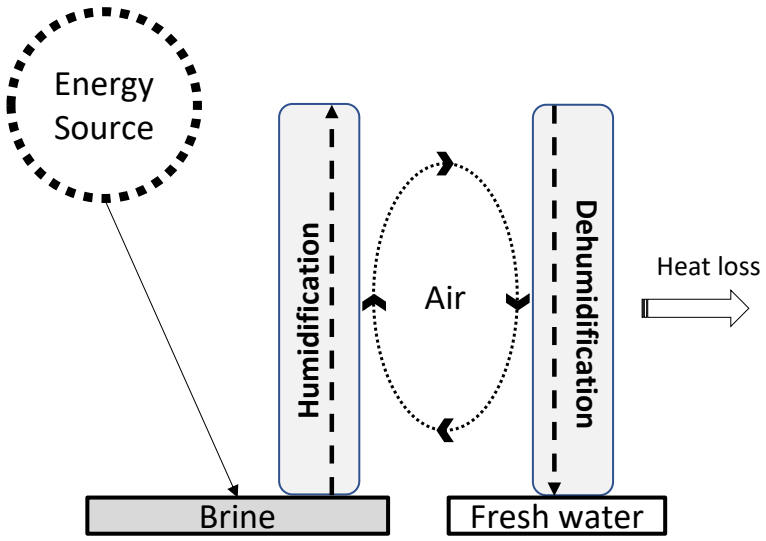

Figure 5.1: Closed-air open-water (CAOW), water-heated, humidification-dehumidification (HDH) inspired by the natural water cycle.

The HDH technology offers many advantages over other thermal desalination technologies. For instance, HDH systems do not use membranes or hot metal surfaces that are prone to scaling or fouling and expensive to replace [43]. Hence, do not require sophisticated feed water pre-

treatments and costly maintenance. HDH technique is very tolerant to high salinity and it can produce high-quality (distilled) water by treating polluted water, brine from other desalination plants, irrigation run off, and various industrial wastewater, including produced water from oil/gas exploration and mining [147]. Their simple transportation mechanism requires no complex mechanical or thermal components, reducing capital and operation/maintenance costs [148]. Furthermore, HDH systems can be powered by solar and geothermal energy or low-grade waste heat [23], and due to their modular characteristics, can be designed to produce minimal or zero liquid discharge, making them well-suited for mobile in-land applications. Figure 5.2 shows a map of the present study area.

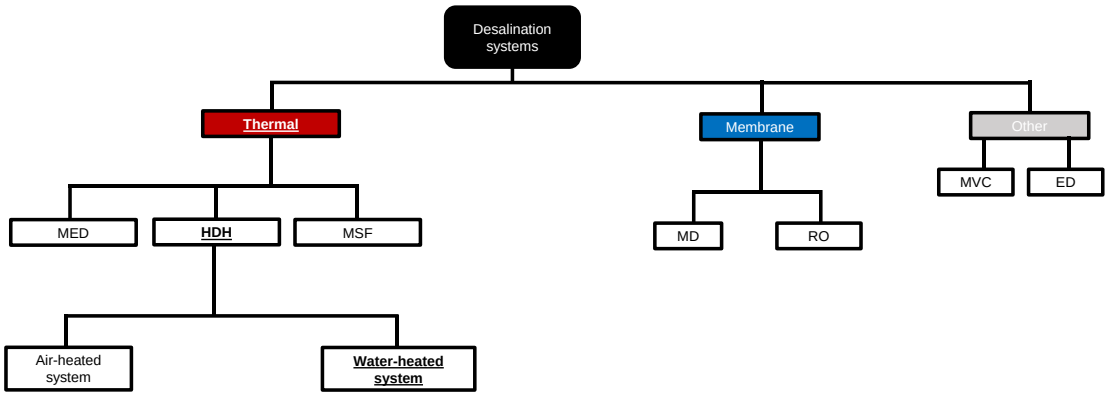

Figure 5.2: An overview of desalination techniques. Area of current study shown in underlined font.

A primary issue with earlier versions of HDH systems is their relatively low effectiveness for dehumidification. Much higher surface areas are needed for condensation to compensate for the low mass transfer rates due to the abundant amount of non-condensable gases under atmospheric conditions [43]. This leads to a more critical challenge with HDH which is its low energy efficiency. To enhance thermal efficiency, past studies [44] proposed mass extractions/injections

between a humidifier and a dehumidifier to thermodynamically balance the HDH system and maximize the thermal energy recovery by reducing entropy production. However, even with implementing the proposed scenario on the existing heat/mass exchanger technologies, a previous theoretical study projected that exchangers of very large sizes are still needed to give *GOR* values that are competitive among other highly efficient desalination devices [45].

Another characterization parameter that researchers normally use to compare desalination systems of any kind-both thermally and mechanically driven-is called specific energy consumption (SEC). SEC is the amount of energy consumed in kilowatt-hour (kWhr) per meter cubed of water production. Compared to pressure-driven RO, any evaporation-based thermal desalination process consumes substantially more energy, up to two orders of magnitude [149]. This shows that currently, in terms of energy consumption, thermal desalination devices are not as efficient as their mechanically driven peers and more research needs to be done, in addition to utilizing alternative renewable energy sources (e.g., solar panels), to reduce the water production cost of thermal desalination systems. On the other hand, however, RO and other filtration technologies are not capable of processing highly saline waters whereas this limitation can be overcome, and near-zero brine discharge plants are achievable using thermal desalination. Similarly, for comparing the amount of electrical energy consumption only in thermal desalination devices, specific electrical energy consumption (*SEEC*) is used which does not include the amount of applied thermal energy. Pumps and fans are the primary consumers of electricity in any thermal desalination system.

The current project addresses the problem of low thermal and electrical efficiency of thermal desalination devices by proposing a novel exchanger for humidification and dehumidification purposes and characterizing its performance by taking advantage of heat/mass transfer and

thermodynamics fundamentals. In this project, we offer a device that can tolerate high levels of brine salinity which is a critical factor for desalination systems aiming at high levels of water recovery. Furthermore, we propose and utilize simple, yet highly effective experimental strategies for both running the system and characterizing its performance which can be used for similar future research in the field of desalination.

5.1.2 Previous research in HDH desalination

Most of the previous studies in the literature on HDH systems have focused on numerical analysis. In a past study, an exergy analysis study on different parts of HDH systems was done with the assumption that exergy gets lost primarily due to the existing driving forces. It was concluded that, since the mass exchange in humidifier is the same as dehumidifier, the total exergy loss due to mass transfer is zero [150]. A more recent study investigated entropy production and exergy efficiency of an HDH system that utilizes a semi-closed air circulation system while applying heat to both air and water streams at different heat ratios. The study suggests that when a low-grade energy source is only available, heating the water stream would result in less entropy generation and hence, higher thermal efficiency [151]. Another study calculated the optimum flowrates for extraction/injection of the air steam in an HDH system driven by solar power with given sizes and water production rates by minimizing the exergy loss [152]. The effects of using a heat exchanger and/or a mixer in a CAOW water-heated HDH system to maximize the heat recovery and *GOR* within the cycle was examined in a different study [153]. The study also included the effect of having zero, one, or two air extractions in their proposed design scheme for a wide range of humidifier and dehumidifier effectiveness.

It is believed that the work by Müller-Holst [146], [154], back in 1999, was the first study that experimentally showed the benefit of multi-effect HDH concept. In their design, to achieve higher performance, air flow rate was adjusted at different sections of humidifier and dehumidifier which resulted in smaller temperature difference between air and water streams. This, in turn, enabled higher heat recovery in the system and a *GOR* range of 5 to 8 was reported from their on-site and laboratory experiments, respectively. In a similar work, a pilot-scale HDH unit with one intermediate air extraction line was constructed and some prior thermodynamic analyses were used to find and apply the operating parameters that give the optimum performance [142]. Based on the experimental data, a maximum *GOR* of 2.6 and 4.0 were projected at optimum points for no extraction and single-extraction cases, respectively. Two years later the same group [43] proposed an HDH system using a direct-contact packed-bed structure for humidification and a series of bubble columns at different temperature levels for dehumidification, both having known sizes and characteristics. A maximum *GOR* of 3.8 was projected when adding an intermediate air flow line from the humidifier to the dehumidifier and applying a specific air flow rate through each channel. In a similar thermal HDH analysis, a recent study found that by increasing the working temperature range, the *RR* increases. Also, it was found that there exists an optimum device size/exchanger area beyond which the *GOR* does not improve appreciably [147].

Desalinating brine using multiple but connected humidifiers and dehumidifiers has also been tested by researchers. In a study, a 3-stage multi-effect solar driven desalination system was numerically and experimentally investigated and a maximum *GOR* of 2.65 was achieved as a result of a higher degree of heat recovery [155]. Another study demonstrated a multi-stage HDH solar desalination system where the heat input is provided directly by a cylindrical Fresnel lens

concentrator [156]. A maximum *GOR* of 2.1 is reported because of exploiting the solar radiation in the desalination unit. Furthermore, subjecting humidifiers to sub-atmospheric pressures is a technique that has been tested on different types of desalination systems including HDH systems. One study reported a *GOR* of 3.4 while using solar irradiation as the heating source and humidifying the air stream under vacuum [157]. Investigators often combine HDH systems with different units to further enhance the energy efficiency. A research group experimentally studied the performance of an HDH desalination system with heat pump unit in order to enhance both heat and water recovery and were able to exceed a *GOR* of 2 at the optimum air circulation flow rate [148].

As noted, mostly conventional shell and tube exchangers or coil finned tubes [158], [159] are used in an HDH system for dehumidification purposes. However, they are typically heavy and expensive due to their large size and suffer from problems of corrosion and scaling. These problems can be partly solved by switching to direct contact heat/mass exchangers where lightweight and cheaper materials are used and latent heat due to the transportation exchanges directly between the air-water streams [160]. There are a few studies where a direct-contact dehumidifier is considered for condensate collection. A parametric analysis compared both types of dehumidifiers and concluded that using direct-contact dehumidification would reduce the cost of water production by nearly 3 fold [161].

As introduced earlier, in addition to HDH, there are other desalination techniques that are primarily driven by a heat source and often give high efficiencies if sufficient number of stages are provided. In a very recent study, a 10-stage solar still device is investigated and a maximum *GOR* of 3.85 is reported as a result of a high degree of heat recovery [162]. However, the sample device is built in small dimensions (~15 cm) and the condensate production is purely relied on

conduction heat transfer which can limit the performance of such platforms if a larger scale design is desired.

Research on water desalination systems using multi-string direct contact heat/mass exchangers started at UCLA (MTSLab) by introducing humidifiers and dehumidifiers that work with such structure [1], [163]. In our earlier works, the superior performance of the multi-string setups compared to other existing devices, in terms of exchanger effectiveness, rate of vapor exchange per device size, and air stream pressure drop were shown. In this project we take advantage of our multi-string exchanger design to build a desalination system that works with HDH concept and offers relatively high levels of thermal efficiency. Furthermore, we realize that a comprehensive experimental study on HDH devices is lacking in the literature where our present work tries to fill this gap.

5.1.3 Direct-Contact Multi-String Heat/Mass Exchangers

One example of exchangers based on the direct-contact concept are bubble columns where they can be used as humidifiers and/or dehumidifiers in an HDH system [164]–[166]. A stream of air injected to a pool of water through small holes can create large liquid-gas interfacial areas for effective heat and mass transfer. A past study [167] experimentally investigated the effects of water temperature, hole diameter, and air flow rate on the performance of a bubble column humidifier. Although these devices guarantee complete humidification of passing air, bubble columns introduce significant gas-stream pressure drops and thereby require high electric energy consumption resulting in high *SEEC* values.

We propose a new direct-contact design for heat/mass exchangers to be utilized in an HDH system to overcome the issues with the existing exchangers. Our novel exchanger is based on a multi-string structure consisting of a dense array of vertically aligned strings as illustrated in Fig. 5.3. A heated brine stream is flown down the strings in the humidifier while making direct contact with a counterflowing gas stream that carries the evaporated water. Then the humidified air enters the dehumidifier and loses a portion of its water content on the surface of the counterflowing clean water stream. The unique configuration of our multi-string humidifier design affords high interface-to-volume ratios necessary for high heat/mass exchanger effectiveness in a compact and light-weight unit at very low gas-stream pressure drops. Our system also enables performance enhancement of the device by introducing intermediate extractions/injections between the humidifier and the dehumidifier. We further discuss the effect of mass extractions in subsequent sections.

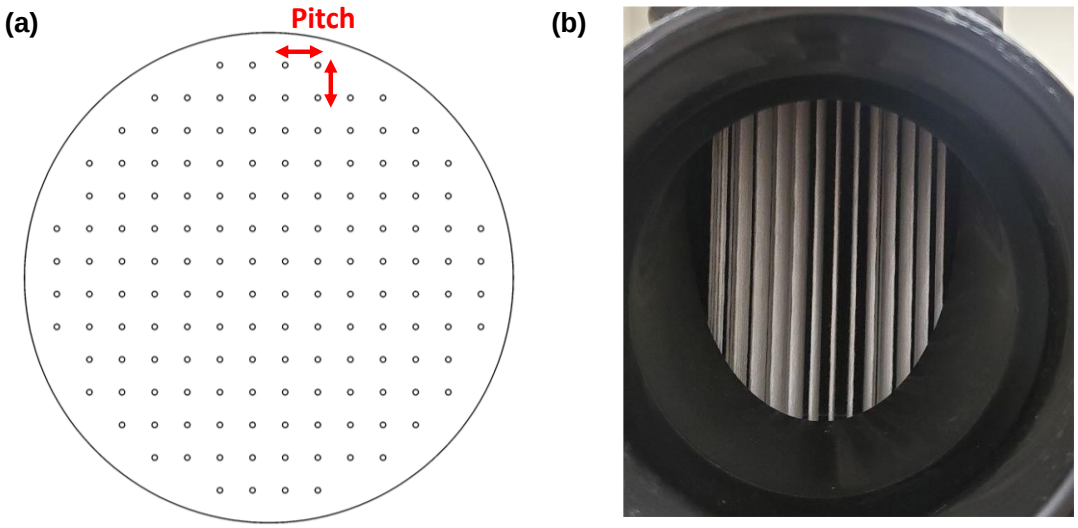

Figure 5.3: (a) Top view schematic and (b) a picture of a dense array of strings in a multi-string exchanger.

Past studies explored the use of liquid films flowing down strings for direct contact heat or mass transfer applications. Hattori et al. [168] presented approximate analytical models for the temperature distribution of a liquid film on a string subjected to cross-flows of a cooling gas. A later study performed CO_2 absorption experiments where they compared the performance of spray columns, packed beds and wetted string columns and demonstrated the superiority of wetted string columns[169]. Extending this work, Uchiyama et al. [170] reported an analytical model to predict the CO_2 absorption performance. Migita et al. [171] constructed a prototype containing an array of 109 strings to study CO_2 absorption effectiveness. They successfully demonstrated that, under the same inlet liquid and gas conditions, wetted string columns perform better in terms of absorption effectiveness and gas pressure drop over conventional packed columns and spray columns. Pakdehi et al. [172] investigated the hydrazine absorption by a wetted string column with different number of strings and confirmed the advantage of wetted string columns in gas-phase pressure drop. Hosseini et al. [173] developed a computational fluid dynamics (CFD) model and performed a parametric study to examine CO_2 absorption by a liquid film flowing along a single string. A recent study [174] also developed a numerical model for a CO_2 absorption process in a wetted string column and reported good agreement with the previous experimental results [171]. In addition to mass transfer studies, many experimental studies focus on heat transfer performance of a turbulent liquid film around a uniformly heated tube [175]–[177]. Shmerler et al. [178] measured the wall heat flux and temperature gradients across the liquid films to develop correlations for the normalized liquid-side heat transfer coefficients and the Reynolds number. These experiments focused on subcooled liquid films or saturated liquid films undergoing evaporation. However, very few studies were reported on heat transfer characteristics of liquid films flowing down thin strings with a counterflowing gas. A previous

study [95] reported a rather limited experimental investigation of the cooling of thin films of a heated silicone oil flowing down a single string. They compared the effectiveness of string-of-bead flow and annular film flow at the same liquid flow rate and demonstrated that the string-of-bead flow exhibited a higher overall heat transfer coefficient than the annular film flow.

The multi-string exchanger has advantages of the high interfacial heat/mass transfer rate, low gas phase pressure drops, and light foot weight/cost. Implementing multi-string exchanger platforms in industrial dry cooling or thermal desalination can greatly reduce the facilities size and expense. These advantages make the multi-string exchanger superior to other direct contact methods and competitive among existing commercial exchangers. In this study, we investigate the performance of direct-contact multi-string heat/mass exchangers in an HDH desalination system.

5.1.4 Research idea

From both fundamental laws of thermodynamics and heat and mass transfer analysis we later prove that higher water production rate per unit heat input (i.e., *GOR*) is achievable by adjusting the ratio of air and water flow rates along heat/mass exchangers in a given HDH desalination system. This is a result of minimizing entropy generation per freshwater production in the thermodynamic cycle which results in higher heat recovery, and hence, lowers the amount of energy input that is needed for the device operation.

The idea here is to use such scientific findings and incorporate it into our multi-string heat/mass exchangers to build a thermal desalination device that can produce high quality fresh water by processing highly saline brines at relatively low energy consumption rates.

5.2 Experimental setup and methods used for numerical and experimental analysis

5.2.1 Design criteria

Design criteria is to develop an innovative low-cost, lightweight heat and mass exchanger technology specifically optimized to enable economic and energy efficient (high *GOR*) thermal desalination systems based on the humidification-dehumidification (HDH) process. The system is designed to provide ~60 L/day of fresh water. The prototype is also designed to tolerate simulated feed water streams at TDS >250,000 ppm. Furthermore, total size/height of the device is designed to accommodate limited space availability.

5.2.2 Multi-string HDH desalination system prototype

We construct the multi-string heat and mass exchangers based on results from our thermodynamic and optimization model for a CAOW HDH thermal desalination system with mass extractions. In this system, as shown in Fig. 5.4 the hot and humid air exits through 2 different paths from the humidifier into the dehumidifier: one at an intermediate section and the other at the outlet, located respectively at $x1 = 0.73$ m and $x1 = 1.79$ m. After cooling down and condensing its surplus water content, air exits the dehumidifier and enters the humidifier and completes the loop. Each setup consists of a vertical acrylic cylindrical pipe with an inner diameter of 7.62 cm for air flow, a top liquid reservoir, a bottom liquid reservoir, and a dense (with a pitch of 5mm) 2D array of 148 vertically aligned cotton strings as illustrated in Fig. 5.3. All the strings are under tension to ensure their verticality and sturdiness. Plastic nozzles, engraved directly into the plexi-glass sheets, with an inner diameter of 1.25 mm are used to

supply water from the reservoir (Fig. 5.5). For the airflow extraction and injection, tee sections are chosen with respect to the flow configuration to minimize irreversibility due to flow bending. Moreover, we minimize unwanted pressure drops and condensations by using channels with same dimensions throughout the device and only airflow controller to control the amount of mid-point extracted air stream.

A two-step heating system consisted of immersion heater and an in-line heater is used to heat the inlet brine to high temperatures up to 90 ℃. A circulation pump keeps the brine concentration and temperature uniform by constantly mixing the brine in the tank and feeds the hot brine stream into the top humidifier reservoir. Another pump supplies the clean (condensing) water to the dehumidifier. The liquid in each device is then divided into multiple uniform streams using an array of nozzles built into the top reservoirs. As the liquid streams flow down the strings under gravity, they form traveling liquid beads due to intrinsic instability caused by the interplay among surface tension, viscous, gravity, and inertia forces [16]. A total of 30 micro thermocouples are mounted at different sections including different axial locations along the body of the exchangers (x1 = 0 or liquid inlet, 0.92, and 1.79 m in the humidifier, and x2 = 0, 1.08, and 2.09 m in the dehumidifier) and different radial positions to capture the temperature profile of the airflow, as shown in Fig. 5.4 (locations 1 to 3 for humidifier and dehumidifier). Moreover, multiple thermocouples are used to monitor inlet and outlet temperatures of the brine/water streams. All piping, reservoirs, and junctions are insulated using fiberglass with different R-values (up to 13).

12V DC brushless fan placed in-line with the side channel, capable of withstanding temperatures up to 85˚ C and saturated conditions (i.e., 100% relative humidity), guides the air flow in the system and is controlled using a 25 kHz signal. 2 set of venturi tubes (throat

diameter: 24.5 mm, inlet diameter: 62.5 mm) attached to pressure transducers (Dwyer, 648C series) and placed at reasonable distances from the fan measure the air flowing through the side air channels. Pressure transducers are chosen based on the range of air flow rate (0-62 Pa) and always remain attached to the system. During operation, top reservoir nozzles and bottom outlet openings are filled with water, keeping the airflow in a closed loop. We ensure the accuracy of venturi tubes by comparing measured values with standard calibrated rotameters. Venturi tube measurements are used for calculating the wet and dry airflow rate through the system. The air flow through the mid-point extraction line is controlled via both fan speed and a flow controller (i.e., an orifice).

We use National instrument (NI, models: 6009, 9162, 9213) devices for measuring electrical signals and transferring them to temperature and pressure/flowrate readings. We use turbine flow meters (GEMS, FT-210) and precision scales (Ohaus SP, 0.01 g precision) to measure the inlet and outlet water flow rates. A precise conductivity meter (LAQUA, F-74G) is used to analyze the feed, concentrated bine, and the produced water and, also, to verify the amount of evaporation/condensation calculated based on the concentration balance.

Uncertainty in the measured water temperatures at inlets and outlets is measured to be ±0.5 °C. Uncertainty in the measured air mass flow rate is estimated to be 0.05 g/s, and uncertainty in the measured liquid flow rates is 0.1 g/s. A picture of our experimental setup is shown in Fig.5.6.

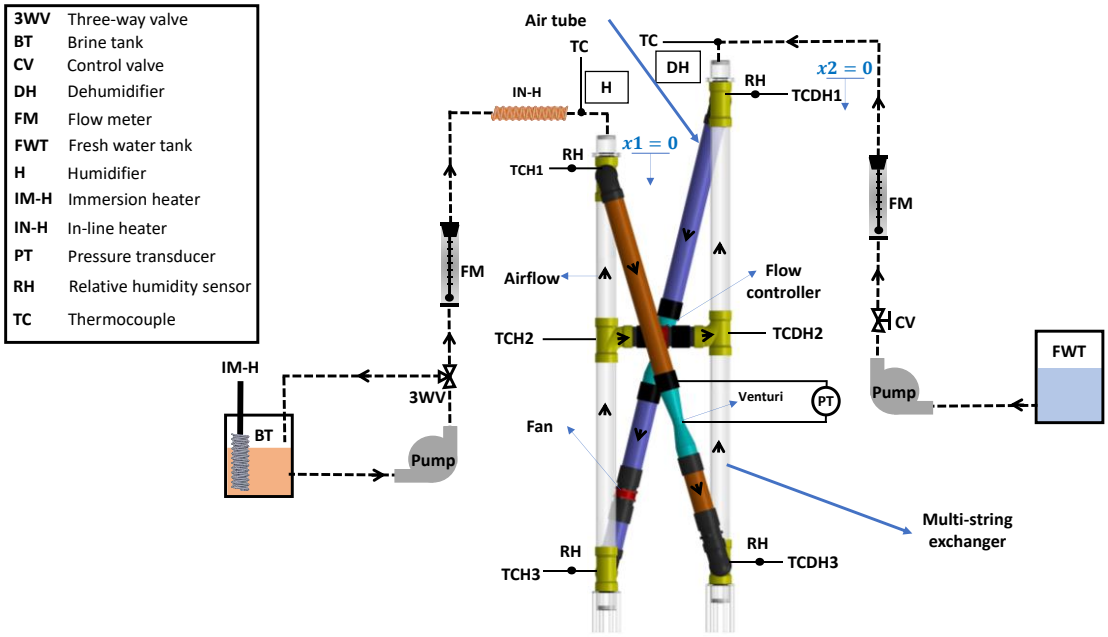

Figure 5.4: Schematic of the experimental setup.

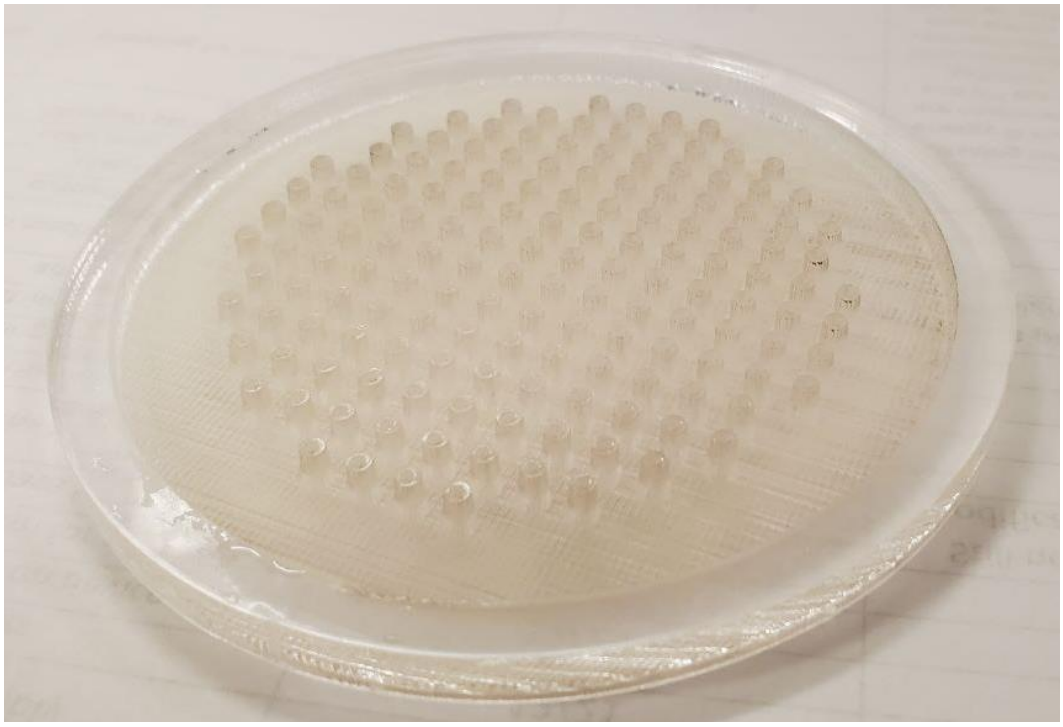

Figure 5.5: Plastic nozzles for liquid distribution in the multi-string exchanger.

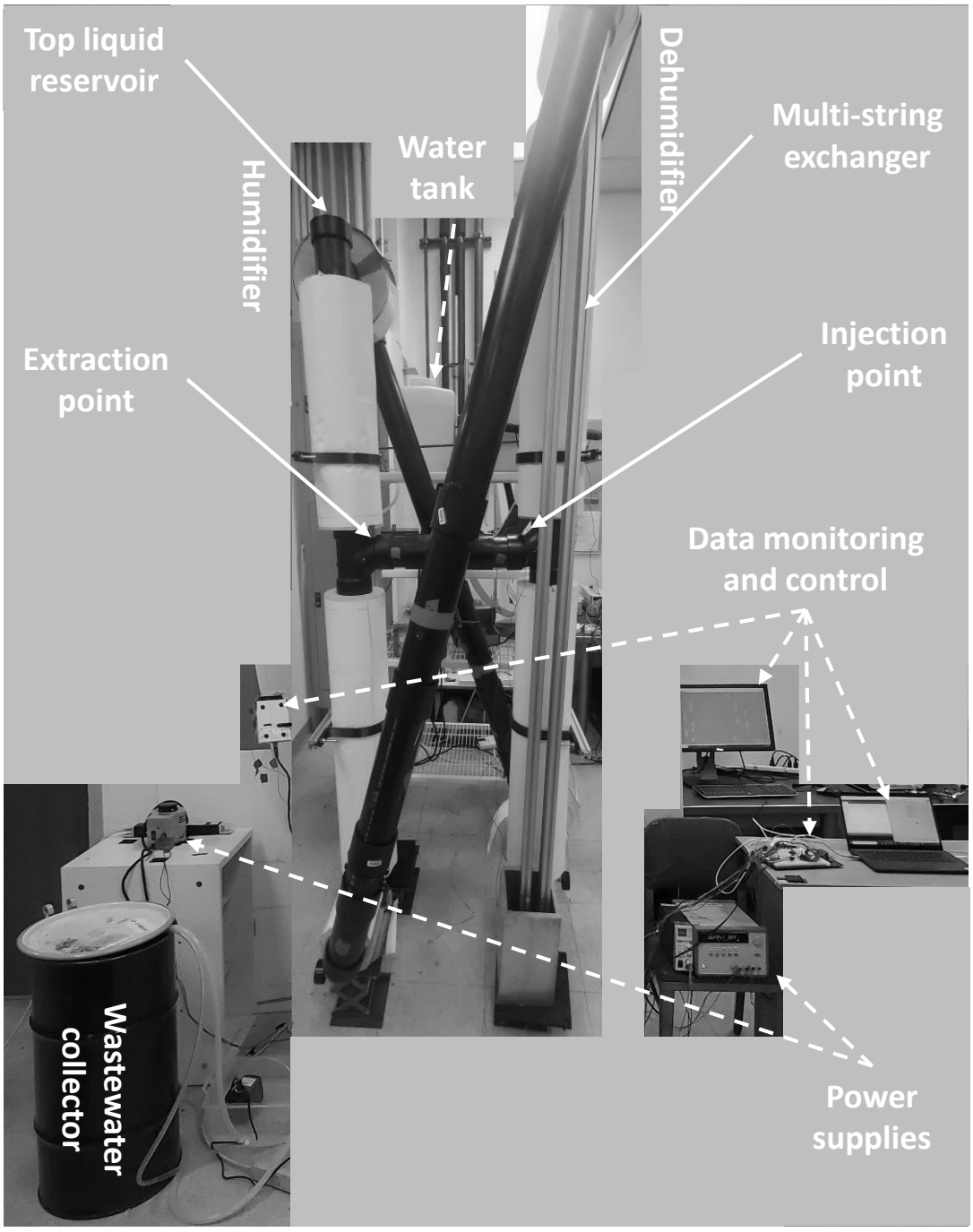

Figure 5.6: An image of the HDH experimental setup and the equipment. Solid lines are pointing at different parts of the exchangers and dashed lines are pointing at the equipment. Note that some parts are not shown in this figure.

5.2.3 Methods used

We first build a heat and mass transfer model and validated it using our comprehensive experimental results from the previously-studied scaled version multi-string exchangers [1], [163]. Then we conduct a general thermodynamics analysis on thermal desalination with HDH approach to create an initial design concept based on the effect of parameters on the performance of the system. We build a multi-string desalination system and predict its performance using our prior modeling knowledge and experience. We confirm our predictions (within ~20%) by conducting experiments on the setup. In the final step, we develop a system-level optimization model to find a highly efficient design and took the following as key inputs: the feed water (brine) input temperature (e.g., output from the solar heater) and flow rate, the condensing water inlet temperature and flow rate, the target clean water production rate, the heat and mass transfer conductance rates, and the maximum acceptable number of intermediate connections (i.e., extraction/injection points). The key outputs are the *GOR*, *RR*, the stream-to-stream flow rate ratio at all sub-sections, and each sub-section's height. The system-level model is implemented in an optimization scheme in MatLab.

5.2.4 Runs and experiments done

Using our developed heat and mass transfer model for HDH systems, the effect of feed and condensing water inlet temperatures and their flow rates, the effect of total dry air circulation rate, and the effect of amount of air extraction are studied on the built setup. The numerical modeling helps identifying the operating conditions at which the system offers its maximum efficiency. Similarly, the experiments are conducted to find the optimum performance point (i.e., highest *GOR*) of the HDH system as a function of inlet temperatures and flow rates for both no extraction and with extraction cases. Highly saline brine (up to ~250,000 TDS) is used in the

experiments to monitor the performance as a function of brine quality and to investigate any potential maintenance/reliability challenges that they might cause.

The optimization problem is run for a variety of cases including having zero, one, or two extraction points on the desalination system to see what design approach we need to follow to reach high values of *GOR* with respect to the practical constraints (e.g., height limitation).

We use the pressure transducers, precision scales, turbine flow meters, and temperature readings to locate the operating points on the performance curves and calculate both *RR* and *GOR* values from the experimental runs. We analyze the obtained data to find the necessary parameters. For instance, we first convert the airflow measurements to dry airflow rates, by assuming the air is fully saturated, to find the water to dry air mass flow rate ratio (i.e., M_r). Equation (5.3) shows how we calculate the M_r

$$M_r = \dot{m}_{b.in}/\dot{m}_{da} \quad (5.3)$$

where $\dot{m}_{b,in}$ is the mass flowrate of the brine or the feed applied to the system and $\dot{m}_{da}$ is the masss flow rate of the dry air. Note that, unlike the wet airflow, the mass flow rate of dry air is consistent throughout the whole device.

We calculate rate of evaporation/condensation by comparing the inlet and outlet water mass flow rates (Eq. (5.4a)) as well as utilizing the saturated air assumption (Eq. (5.4b))

$$RR = \left(\dot{m}_{b,in} - \dot{m}_{b,out}\right)/\dot{m}_{b,in} \quad (5.4a)$$

$$RR = \left(\dot{m}_{da,hot}\left(\frac{1}{1-\phi_{hot}} - \frac{1}{1-\phi_{cold}}\right) + \left(\dot{m}_{da,cold} - \dot{m}_{da,hot}\right)\left(\frac{1}{1-\phi_{Ext}} - \frac{1}{1-\phi_{cold}}\right)\right)/\dot{m}_{b,in} \quad (5.4b),$$

where $\dot{m}_{b,out}$ is the masss flow rate of the condsnsate being discharged at the outlet of humidifier. Also, $\dot{m}_{da,hot}$ is the dry air mass flow rate exiting the humidifier and $\dot{m}_{da,cold}$ refers to the dry air exiting the dehumidifier. Also, ϕ_{hot}, ϕ_{Ext}, and ϕ_{cold} represent the saturation mass ratios (or absolute humidity ratios) at the humidifier outlet, extraction point, and dehumidifier outlet, respectively. Obviously, when there is no air extraction, dry air mass flow rate is constant everywhere and the second term in Eq. (5.4b) becomes zero.

By having the *RR* and the outlet dehumidifier water temperature, one can easily calculate the *GOR* based on Eq. (5.5).

$$GOR = RR \times h_{fg} / \left(C_{p,b} \times \left(T_b - T_{DH,o} \right) \right) \qquad (5.5)$$

Here, $C_{p,b}$ is the specific heat of brine at the averaged temperature, T_b is the brine inlet temperature and $T_{DH,O}$ is the temperature of hot water from dehumidifier outlet. Note that we use this simplified form for presenting the *GOR* where we are assuming that a perfect heat exchanger (100% effectiveness) is used to preheat the new brine with the hot water being discharged from the dehumidifier. However, Eq. (5.6) shows a more general form for calculating the *GOR* when the effectiveness (η) of the preheating heat exchanger is less than 100% and T_i is the initial (new) brine temperature.

$$GOR = RR \times h_{fg} / \left(C_{p,b} \times \left(T_b - \eta \left(T_{DH,o} - T_i \right) - T_i \right) \right) \qquad (6)$$

We use Eq. (5.5) to plot and compare experimental results as a function of the operating parameters. But we later demonstrate and discuss the effect of heat exchanger effectiveness on the overall performance of the device using Eq. (5.6).

5.2.5 Air-side Pressure Drop in Multi-String Heat/Mass Exchangers

A key consideration in an HDH system, aside from the thermal efficiency and water recovery, is the rate of electricity consumption consumed by fans and pumps during operation. By knowing this, one can calculate electrical consumption per unit produced water which contributes to overall water production cost. Since the water flows by its own weight in multi-string exchangers (i.e., gravity driven), we focus more on developing a model that predicts air-side pressure drop to find out how much power is needed to provide the desired circulation air flow. The air-side pressure drop $\frac{dP}{dz}$ consists of three major components: the frictional pressure drop $\left(\frac{dP}{dz}\right)_f$, the pressure drop due to gravity $\left(\frac{dP}{dz}\right)_g$, i.e. hydrostatic, and the pressure drop due to the momentum change $\left(\frac{dP}{dz}\right)_m$ as shown in Eq. (5.7). Air momentum changes since we have expansion/compression due to evaporation/condensation (Eq. (5.8)).

$$\frac{dP}{dz} = \left(\frac{dP}{dz}\right)_f + \left(\frac{dP}{dz}\right)_g + \left(\frac{dP}{dz}\right)_m \tag{5.7}$$

$$\left(\frac{dP}{dz}\right)_m = \left(\frac{\dot{m}}{A_c}\right)^2 \left(\frac{1}{\rho_m} + \frac{1}{\rho_w}\right)\frac{d\omega}{dz} \tag{5.8}$$

In the above equations, *A*c represents the cross-section area for the air stream, ρ_w is the density of water, and ω is the humidity ratio.

The frictional pressure drop for laminar flows along the strings can be calculated using Eqs. (5.9) and (5.10), in terms of the friction factor f_L [179].

$$f_L Re\left(\frac{D_f}{D_h}\right) = \frac{8\sigma^2}{2(1-\sigma)-\ln(1-\sigma)-0.5(1-\sigma)^2-1.5} \tag{5.9}$$

$$\left(\frac{dP}{dz}\right)_f = \frac{2f_L\rho_m V_{air}}{D_h} \tag{5.10}$$

Here, $Re = \rho_m V D_h/\mu$ where V and μ are the relative air stream velocity and viscosity, respectively. Also, D_h and D_f are the hydraulic diameter and the average liquid film diameter calculated from Nusselt solution, respectively [104]. Parameter σ represents the fraction of the total cross section available to the air flow.

5.3 Numerical analysis, performance prediction, and experimental data

5.3.1 Balancing an HDH desalination System

Many studies in the literature on heat exchangers address the flow condition at which a given device performs at its best, or in other words, minimizes the exergy (recoverable energy) loss. This study is crucial for any thermodynamic cycle such as HDH systems since heat (or energy) recovery plays a significant role in the overall efficiency of the system. It has been proven that if a heat exchanger working in a thermodynamic cycle runs at the heat capacity rate ratio (*HCR*) of one, heat recovery in the cycle becomes maximum. In this condition, the heat exchanger is considered to be "balanced". Similarly, for a heat/mass exchanger device, a general expression, called modified *HCR*, is defined to quantify the exchange between the streams:

$$HCR = \frac{\triangle \dot{H}_{max.C}}{\triangle \dot{H}_{max.H}}, \qquad (5.11)$$

where $\triangle \dot{H}_{max}$ represents the maximum rate of enthalpy change that can possibly happen in the exchanger for each (hot (H) or cold (C)) stream. By having *HCR* = 1 for the heat and mass exchanger, the amount of heat recovery becomes maximum in the thermodynamic cycle [180], [181]. However, we also note that, since mass flow rates and heat capacity rates are not constant for the streams as they pass through the system, it is not possible to maintain the *HCR* = 1

condition at all locations in the device. Therefore, we need to somehow adjust the flow rates, for example by extracting or injecting moist air from/into the exchangers, to keep the *HCR* closer to one at all locations. Theoretically, by applying an infinite number of injections/extractions we can fully balance an exchanger which, of course, is not realistic. However, thermodynamic analysis shows that, even a few numbers of extraction/injections can substantially increase the overall efficiency of an HDH system.

Similar to the effectiveness defined in the literature for heat exchangers, an energy-based effectiveness can be defined for heat and mass exchangers. Equation (5.12) shows the relation for effectiveness of heat and mass exchangers which is defined as the ratio of change in total enthalpy rate ($\triangle \dot{H}$) to the maximum possible change in total enthalpy rate ($\triangle \dot{H}_{max}$) [142]. The maximum possible change in total enthalpy rate can be found from Eq. (5.13). The definition given in Eq. (5.12), however, does not give a meaningful result for a humidifier as the streams can never reach the terminal temperatures, even for humidifiers with infinitely large area. Hence, other relations have been proposed in the literature to overcome this issue [43].

$$\varepsilon = \frac{\triangle \dot{H}}{\triangle \dot{H}_{max}} \qquad (5.12)$$

$$\triangle \dot{H}_{max} = \min (\triangle \dot{H}_{max.C}.\ \triangle \dot{H}_{max.H}) \qquad (5.13)$$

From thermodynamics point of view, McGovern et al. [45] proposed that it is advantageous to normalize enthalpy rates by the amount of dry air flowing through the system (h^*). Hence, the effectiveness can be presented as in Eq. (5.14).

$$\varepsilon = \frac{\triangle h^*}{\triangle h^* + \Psi} \qquad (5.14)$$

Ψ in Eq. (5.14) is called the "enthalpy pinch" and is defined as the minimum loss in enthalpy rate due to a finite device size at any point in the exchanger device. Equation (5.15) shows the mathematical description.

$$\Psi = min_{local}(\triangle h^*_{max} - \triangle h^*) \qquad (5.15)$$

We use the Ψ expression, despite using physical dimensions directly, in order to express the size of the device (i.e., the transfer area) in our primary thermodynamics' calculations. In this respect, as Ψ approaches zero, the device size becomes nominally infinity. Equation (5.16) shows the relation between the slope of temperature-normalized enthalpy curves and the mass flow rate ratio [181]. Considering constant specific heat for water and assuming a linear temperature-enthalpy relation for the water stream, one can obtain the mass flow rate ratio from the temperature-enthalpy diagram:

$$\text{slope} = \frac{dT_w}{dh^*} = \frac{1}{M_r C_{p.w}} \qquad (5.16)$$

where the mass flow rate ratio, M_r, is the ratio of the mass flow rate of water to that of dry air.

As discussed earlier, one useful way to enhance the thermal efficiency of HDH systems is to minimize the entropy generated within the cycle per unit water produced. Equation (5.17) can be used for both humidifiers and dehumidifiers to calculate the amount of entropy generated in each device. $\dot{m}_w$ is the mass flow rate of water/brine, $\dot{m}_{air}$ is the mass flow rate of moist air, s_w is the entropy of water/brine, s_{air} is the entropy of moist air, and subscripts *in* and *out* denote inlet and outlet conditions. The overall entropy generated, therefore, can be calculated from Eq. (5.18), where subscripts *H*, *DH*, and *heater* denote humidifier, dehumidifier, and the heat source,

respectively.

$$\dot{S}_{gen} = \dot{m}_{w,out} s_{w,out} - \dot{m}_{w,in} s_{w,in} + \dot{m}_{air,out} s_{air,out} - \dot{m}_{air,in} s_{air,in} \quad (5.17)$$

$$\dot{S}_{gen,tot} = \dot{S}_{gen,H} + \dot{S}_{gen,DH} + \dot{S}_{gen,heater} \quad (5.18)$$

Previous studies have utilized entropy generation minimization to find the optimum operating point for an HDH system as well as proving the positive effect of adding extractions/injections in such systems [43], [180], [182].

Figure 5.7 shows the temperature-enthalpy diagram for a system having enthalpy pinch of 15 kJ/kg working with zero (a), one (b), and two (c) extractions/injections. The cold-water stream enters the dehumidifier at 20^{o} C and the hot brine stream enters the humidifier at 90^{o} C. The slope of the water line in the temperature-enthalpy diagram can be used to evaluate the mass flow rate ratio at any given point in the device. By comparing the curves in Figure 5.7, we note the flow adjustment created by the intermediate connection points and the resulting *GOR* enhancement due to further reducing the total specific entropy produced in the system.

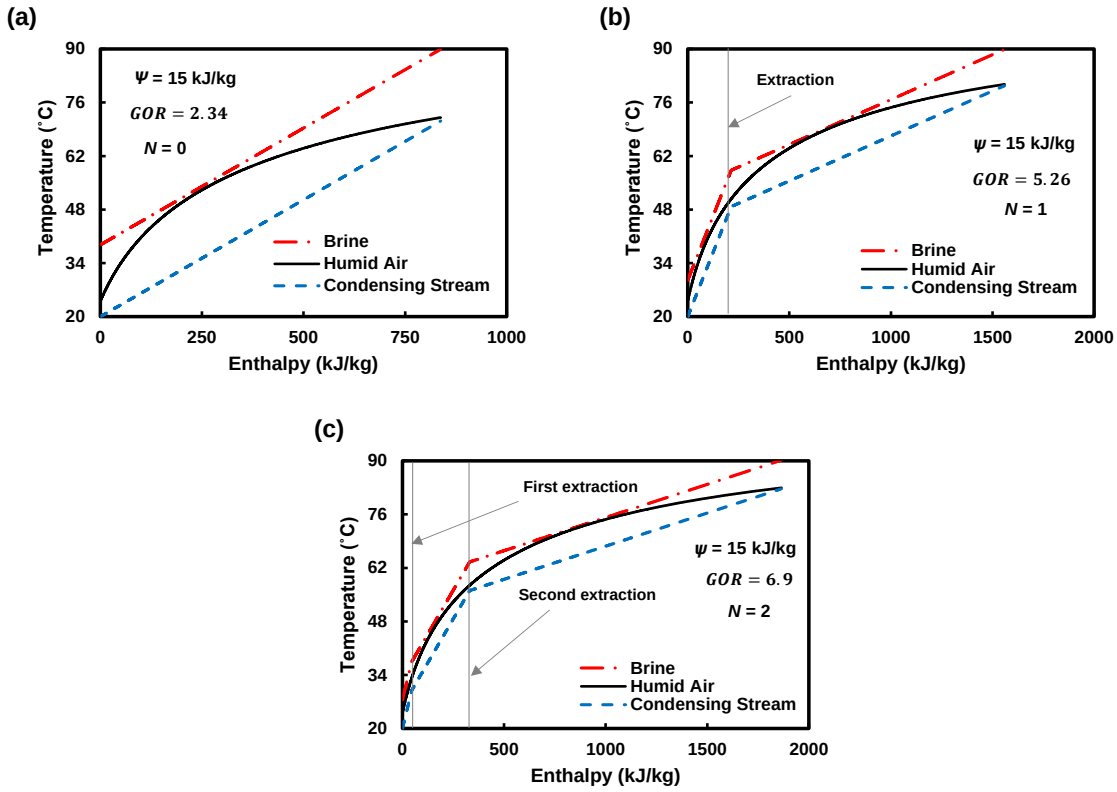

Figure 5.7: Temperature-Enthalpy diagram for a thermodynamically balanced HDH system with an enthalpy pinch (Ψ) of 15 kJ/kg with zero (a), one (b), and two (c) extractions/injections.

Figure 5.8 shows *GOR* variation for HDH systems working at the same temperature range of 90-20 ℃ but having different enthalpy pinches and number of extractions/injections. At relatively high values of enthalpy pinch ($\Psi > 15$ kJ/kg), higher number of extractions does not necessarily lead to a better performance. On the other hand, for a fixed temperature range, as the enthalpy pinch decreases, the size of device must increase. We also note that, from experimental point of view, adding more extractions will introduce more complexity to the system which might not seem reasonable considering the small percentage of enhancement after adding subsequent sections. Therefore, these important factors need to be considered during designing HDH systems.

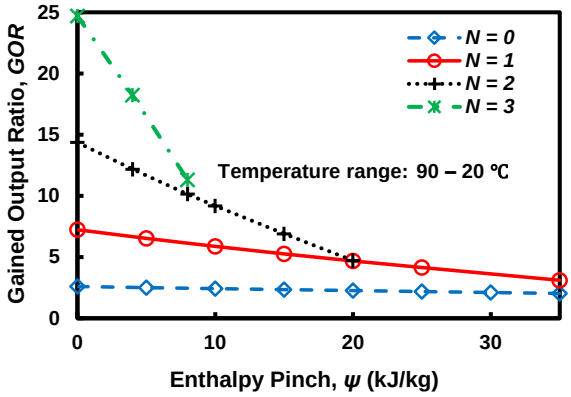

Figure 5.8: *GOR* of balanced systems as a functions of enthalpy pinch for different number of extractions (*N*). The inlet brine temperature and the inlet condensing water temperature for all cases are the same (90 and 20 ˚C, respectively).

5.3.2 Heat and Mass transfer model for multi-string exchangers

Although thermodynamics give us some general insight on how to improve the performance of HDH systems, we still need to develop a numerical model that is specific to the multi-string design to calculate details needed for building an actual desalination system. Moreover, thermodynamic parameters such as enthalpy pinch and exchanger effectiveness do not give any information on the operation parameters that need to be set on an actual device to give the desired outcome. We, therefore, build a 1-D heat/mass transfer model implemented in MATLAB for our multi-string design to further specify physical and flow parameters that give better performance with respect to the flow and other physical parameters. Because the air stream in a CAOW HDH system undergoes a closed loop, we assume that the air is saturated at all locations in the system, and its moisture level is only a function of the temperature. We have verified this assumption during our experiments on the scaled multi-string exchangers. Hence, we calculate the amount of water vapor being carried by the air from its temperature distribution. Figure 5.9 shows the discretized domain for our heat/mass transfer model. Equations (5.19-23) are used throughout the domain to find the temperature distribution and amount of mass transfer. Here, $\dot{m}$

is the mass flow rate, g_m is the mass transfer conductance, g_h is the heat transfer conductance, dA is the water-air contact area for an element, ϕ is the saturation mass ratio (i.e. gr of water vapor / gr of total air), h is the enthalpy, h_{fg} is the enthalpy of vaporization and q_{conv} represents the amount of convection heat transfer. Subscripts L, g, amd n refer to liquid stream, air stream, and number of the corresponding element, respectively. We estimate the heat transfer conductance using the heat and mass transfer analogy (Eq. (5. 24)) where Lewis number ($Le = \rho DCp/k$) is a dimensionless number defined as the ratio of the mass diffusivity to the thermal diffusivity where ρ is density, D is the diffusion coefficient, and k is the thermal conductivity. Note that these equations are used for both humidifier and dehumidifier. Equations (5.19) & (5.20) are for air and water mass balance, and Eqs. (5.21) & (5.22) are for air and water energy balance. Although the equations used guarantee mass and energy conservation at each element, we also check the conservations for each exchanger and the overall HDH setup as well. In addition to that, we make sure inlet and outlet temperatures match their corresponding points on the other setup since we assume no temperature drop when the air stream is flowing from a device to the other one. As noted from the indexing, we use an explicit scheme for discretizing and solving the equations where we run adequate iterations until the maximum change in any parameter is less than 0.01% with respect to its previous value.

$$\dot{m}_{L.n} = \dot{m}_{L.n+1} + g_m * dA * (\phi_{L,n+1} - \phi_{g,n+1}) \quad (5.19)$$

$$\dot{m}_{g.n} = \dot{m}_{g.n+1} + g_m * dA * (\phi_{L,n+1} - \phi_{g,n+1}) \quad (5.20)$$

$$\dot{m}_{L.n} * h_{L,n} = \dot{m}_{L.n+1} * h_{L.n+1} + dA * (q_{conv.n+1} + g_m * (\phi_{L,n+1} - \phi_{g,n+1}) * h_{fg,n+1}) \quad (5.21)$$

$$\dot{m}_{g.n} * h_{g.n} = \dot{m}_{g.n+1} * h_{g.n+1} + dA * (q_{conv.n+1} + g_m * (\phi_{L.n+1} - \phi_{g.n+1}) * h_{fg.n+1}) \quad (5.22)$$

$$q_{conv.n+1} = g_h * (T_{L.n+1} - T_{g.n+1}) \quad (5.23)$$

$$\frac{g_m}{g_h} = (Le)^{\frac{2}{3}} \quad (5.24)$$

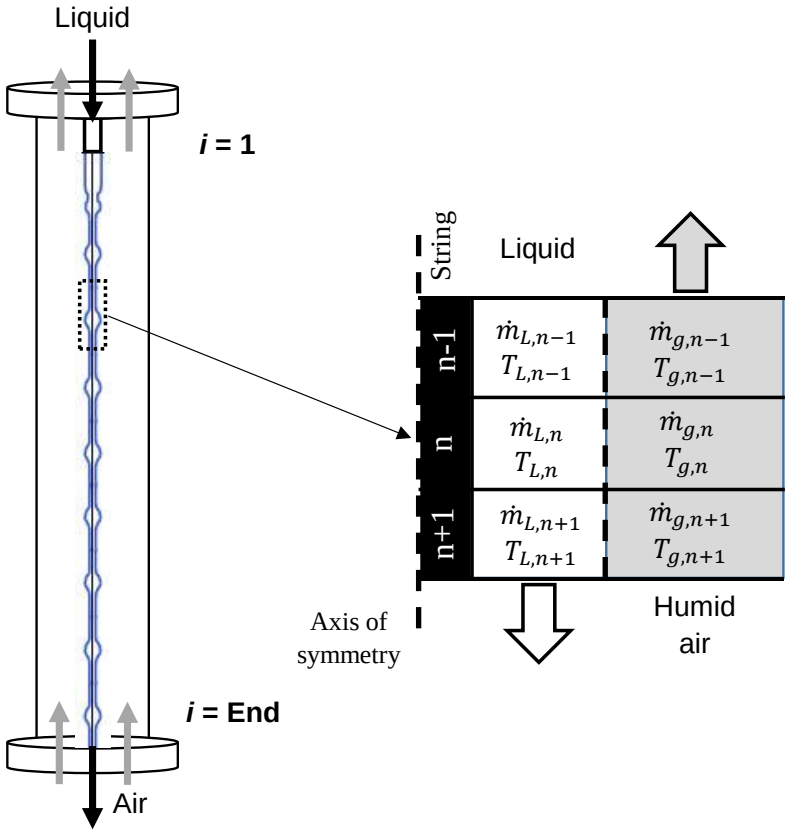

Figure 5.9: Discretized physical and computational domain for the 1D heat and mass transfer model.

Figure 5.10 (a) shows the experimental setup we used for model validation and characterizing the performance of a scaled (~1 meter tall) multi-string exchanger. Curves shown in 5.11 (b) and (c) are from two sample cases that demonstrate the promising performance of the model for predicting the temperature profile in the exchanger while operating as a humidifier (b) or a dehumidifier (c).

Figure 5.11 shows linear curve-fits to the resulting measured experimental mass transfer conductance rates for both humidification and dehumidification processes. Horizontal axis represents superficial air velocity, and each line is for a specific mass flow rate per string (or cell). In our numerical analysis, we incorporate the effect of air velocity change on the heat/mass transfer rates because of change in the volumetric flow rate due to continuous humidification/dehumidification along the exchangers.

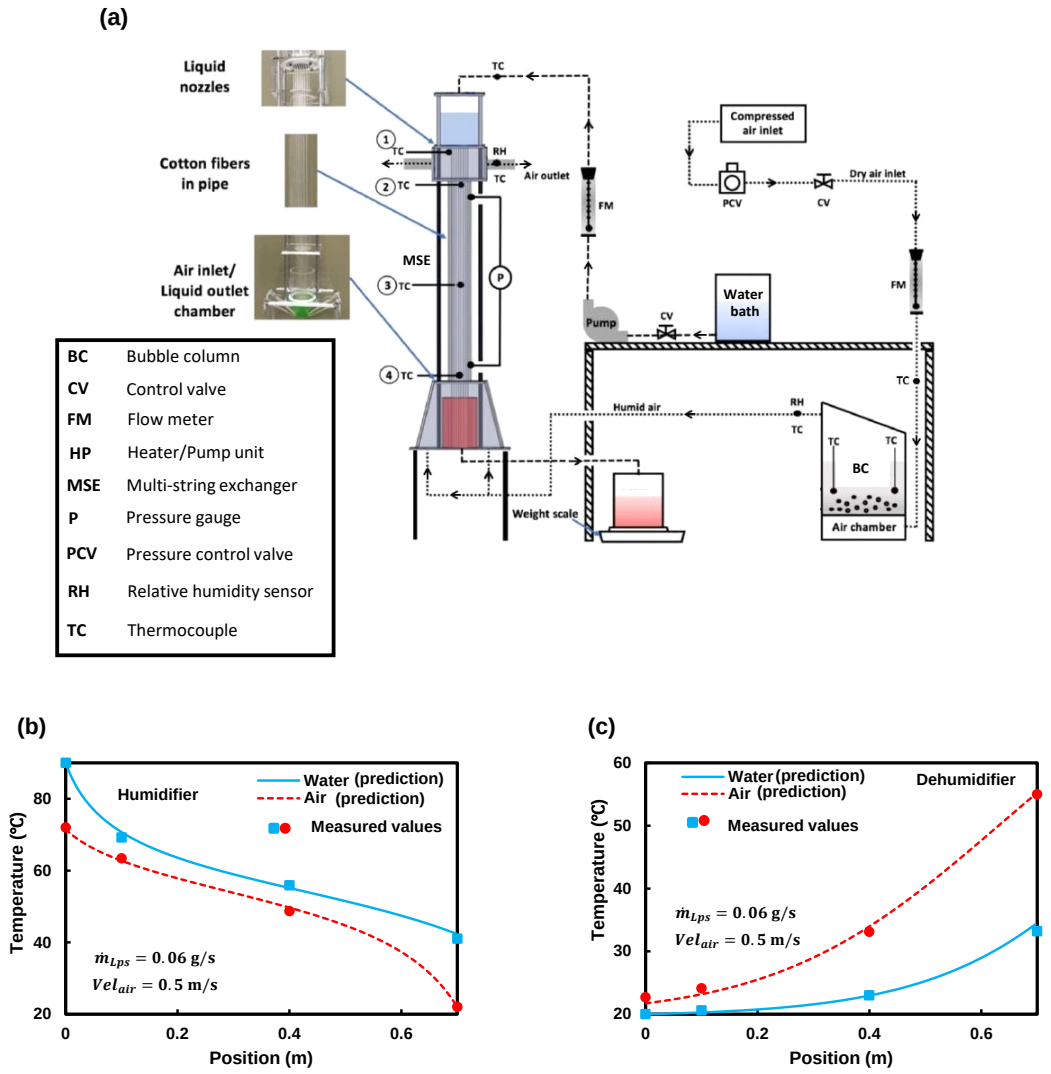

Figure 5.10: (a) Experimental setup used for model validation and characterizing the performance of a scaled multi-string exchanger for both humidification and dehumidification applications. (b) and (c) show sample temperature profiles while the exchanger is used as a humidifier and a dehumidifier, respectively.

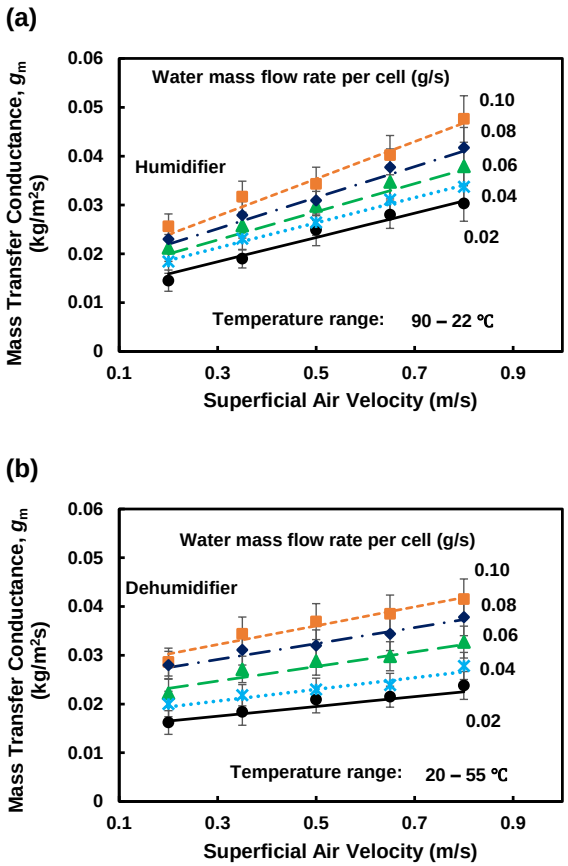

Figure 5.11: Linear curve-fits to experimentally measured mass transfer conductance in (a) humidifier and (b) dehumidifier as a function of superficial air velocity for different mass flow rates per string. Maximum uncertainty is 0.002 kg/(m^{2}s).

5.3.3 Performance prediction for the multi-string HDH desalination system, zero extraction case (N = 0)

After conducting some preliminary experimental analyses and considering the space limitations, we decided to build an experimental setup that supports a single extraction airline. Table 5.1 shows the dimensions of the setup we built for this project. The discussions given in the following sections discuss results from a comprehensive numerical analysis on the performance of the HDH device as a function of both air and water flow parameters. Using the simplified 1-D model introduced earlier, energy and mass conservation equations are solved for all the elements present in the desalination system to find out how the system would perform as a

function of the physical parameters that are initially assigned. We assume perfect mixing condition at the injection point when the extraction is enabled. All the subsequent sections show our performance prediction results on a setup with dimensions shown in Table 5.1 while processing a brine stream at sea level salinity (~35 g/ (kg water)). The latent heat and the specific enthalpy of the saline water can be calculated from:

$$h_{fg,sw} = h_{fg,w}\,(1 - S), \tag{5.25}$$

and

$$h_{sw} = h_w - S \times (a_1 + a_2\,S + a_3\,S^2 + a_4 S^3 + a_5\,t + a_6\,t^2 + a_7\,t^3 + a_8\,S\,t + a_9\,S^2\,t + a_{10}\,S\,t^2). \tag{5.26}$$

The values of a_i coefficients can be found from [163]. $h_{fg,sw}$ and $h_{fg,w}$ denote the latent heat of the brine and the pure water in J/kg, respectively. Similarly, h_{sw} and h_w are the enthalpy of the brine and the pure water, respectively, in J/kg. S is the salinity in kg/kg, and t is the temperature in °C. The vapor pressure of the brine is estimated using Raoult's correlation:

$$\frac{P_{v,w}}{P_{v,sw}} = 1 + 0.57357 \times \left(\frac{S}{1-S}\right), \tag{5.27}$$

where $P_{v,w}$ and $P_{v,sw}$ represent the vapor pressure of pure water and saline water, respectively.

In the following discussions, at first, the effect of the mass flow rate ratio (M_r, Eq. (5.3)), that represents how fast the airflow is recirculating through the system, on the overall performance of the HDH device is demonstrated. Next, the effect of air extraction is shown by varying the extraction flow rate while keeping the overall M_r at a constant level.

Table 5.1: The multi-string HDH system prototype with single extraction

Parameter	Amount	Unit
Humidifier height ($L_{H.1}$ (top), $L_{H.2}$ (bottom))	1.79 (0.73, 1.06)	m
Dehumidifier height ($L_{DH.1}$(top), $L_{DH.2}$(bottom))	2.09 (1.06, 1.03)	m
Cross-sectional diameter of exchanger	7.62	cm
Number of strings	148	#
Water mass flow rate per string	0.06	g/s

Figure 5.12 shows how the *GOR* and *RR* change with the top brine temperature and the overall water to dry air mass flowrate ratio (M_r) in the setup with no extractions (N = 0). Although the maximum *GOR* increases by ~16% as the top brine temperature goes down from 90 ˚C to 60 ˚C, the *RR* decreases by ~45% at the same operating points. Also, the figure shows a clear peak for each curve that addresses the so-called "balanced" state in the system giving the best thermal efficiency. These results are consistent with thermodynamics analysis as well as data reported by previous works [183]. Note that the performance is primarily dependent on the ratio of the air and water streams (i.e., M_r) and changing the flow rates, while keeping the ratio at a constant value, would impose a negligible effect. The other point can be realized from Figure 5.12 is that each *GOR* curve has a sharper peak compared to its respective *RR* curve. This is because of the fact that *GOR* depends on both water recovery (*RR*) and heat recovery ($T_{DH,o}$ in Eq. (5.55)) and due to the significant effect of latent heat on the heat transfer between the air and water streams in each exchanger, the numerator and the denominator in *GOR*'s relation (Eq. (5.5)) respectively become maximum and minimum at the same time, resulting in a sharp peak in *GOR* curves. In other words, the more evaporation/condensation we get, the more heat we can

recover which ultimately results in more efficient desalination, i.e., higher *GOR*. This relation, however, holds when no heat is wasted and all the heat from condensation is transferred to the condensing water stream. Hence, in the presence of heat loss, maximum *GOR* and maximum *RR* might not become coincident.

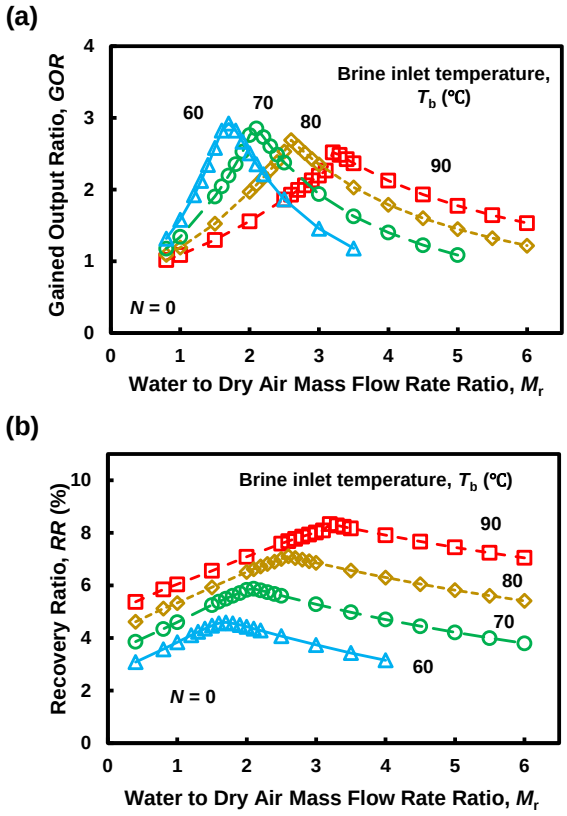

Figure 5.12: Effect of water to dry air mass flow rate ratio (M_r) and brine inlet temperature (T_b) on the (a) *GOR* and (b) *RR* of the Multi-string HDH system when no extraction is applied (i.e., $N = 0$).

Previously, researchers showed the importance of entropy generation minimization in order to reach the peak *GOR* for a given HDH system [43]. Those analysis, however, were characterized by the heat capacity rate ratio in the dehumidifier rather than controllable parameters such as the airflow circulation rate. Here, in Fig. 5.13 (a), we show the normalized

entropy generation as a function of M_r for the case T_b = 80 ℃. The peak *GOR* happens at the point where the normalized entropy generation becomes minimized. Similarly, Fig. 5.13 (b) demonstrates that maximum *GOR* and minimum normalized entropy generation essentially happen at the same operating point where the value of heat capacity rate ratio in the dehumidifier equals one. This indeed shows the importance of flow conditions on the device performance. If we keep every parameter at a constant level and only change the rate of airflow circulation, we reach the maximum *GOR* at a single operating point where it corresponds to the dehumidifier's balanced state. This, again, is because more entropy is produced in the dehumidifier compared to the humidifier due to the relatively large entropy generation during condensation in the presence of non-condensable gases.

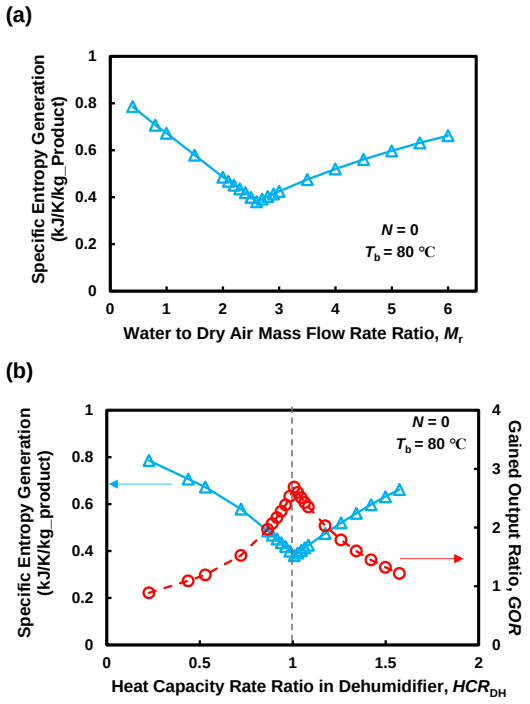

Figure 5.13: Effect of (a) water to dry air mass flow rate ratio (M_r) and (b) heat capacity rate ratio in dehumidifier on the normalized entropy generation and *GOR* of the Multi-string HDH system when N = 0 and T_b = 80 ℃.

5.3.4 Performance prediction for the multi-string HDH desalination system, single extraction case (N = 1)

Figure 5.14 (a) and (b) show the performance of the system after adding an extraction line, in terms of *GOR* and *RR*, as a function of airflow extraction rates for different overall airflow circulation rates (M_r) while T_b is fixed at 90 ℃. This figure clearly shows the effect of amount of dry air extraction rate on the performance. Moreover, by comparing Fig. 5.14 to Fig. 5.12 one can find that the overall dry air circulation rate at the optimum operating point has increased by adding the extraction line. This indeed is consistent with our previous thermodynamic analysis where we realized that changing the airflow within different sections of the system changes the state of the whole HDH system with respect to its balanced condition.

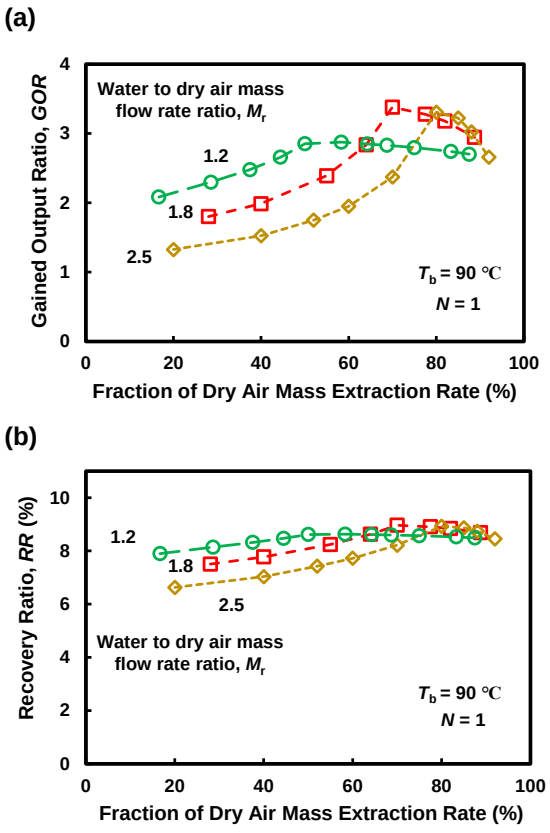

Figure 5.14: Effect of overall water to dry air mass flow rate ratio (M_r) and percent of dry air mass extraction rate on the (a) *GOR*, and (b) *RR* of the Multi-string HDH system when single extraction is applied (i.e., N = 1) and T_b is fixed at 90 ℃.

We previously saw the critical effect of balancing the dehumidifier for achieving the maximum *GOR* in the HDH system. We also realize that by adding an intermediate line for the airflow, the dehumidifier is basically operating via two stages. Our analysis shows that balancing the bottom stage dehumidifier, where it deals with the hotter airflow, is more critical and maximum *GOR* happens when HCR_{DH_bot} gets very close to unity. Figure 5.15 (a) shows how the normalized entropy generation and *GOR* change with varying the amount of extracted dry air while the overall dry air flowrate and inlet brine temperature are held constant. Figure 5.15 (b) shows the relation between the heat capacity rate ratios in each stage of the dehumidifier for the same system discussed in Fig. 5.15 (a). As mentioned earlier, balancing the bottom stage dehumidifier for given inlet conditions, results in achieving the peak performance.

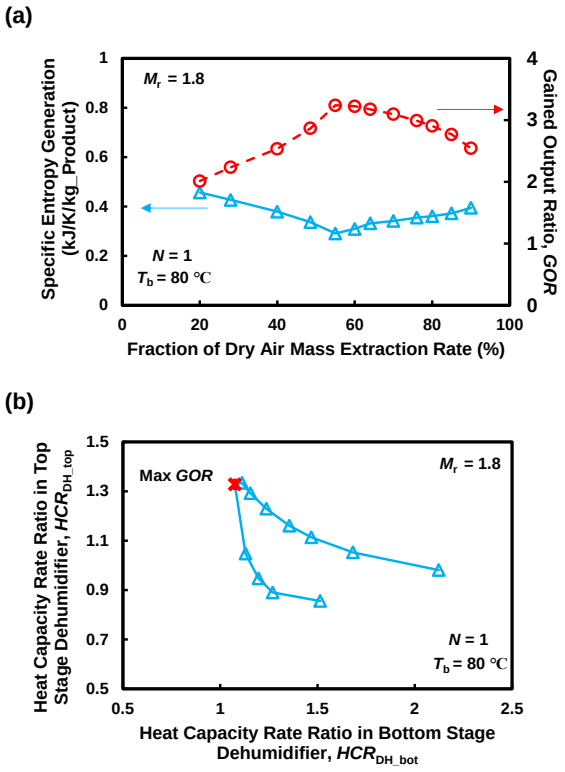

Figure 5.15: (a) Effect of dry air mass extraction rate on the *GOR* and normalized entropy generation for given conditions of M_r = 1.8 and T_b = 80 °C. (b) Effect of balancing dehumidifier bottom stage on achieving peak *GOR*.

5.3.5 Effect of brine salinity, zero & single extraction cases (N = 0 & 1)

Figure 5.16 shows the effect of brine salinity on the multi-string desalination device for both no extraction (first row) and single extraction (second row) cases. As discussed in the numerical modeling section, we incorporate the effect of salinity on the brine's vapor pressure in the humidifier. By comparing the two cases in Fig. 5.16, we can see that increasing brine salinity has a stronger effect on the single extraction cases. The main reason is that, by changing the brine salinity, the optimum operating point that gives the best performance for the given system changes and hence, maximum *GOR* happens at a different M_r.

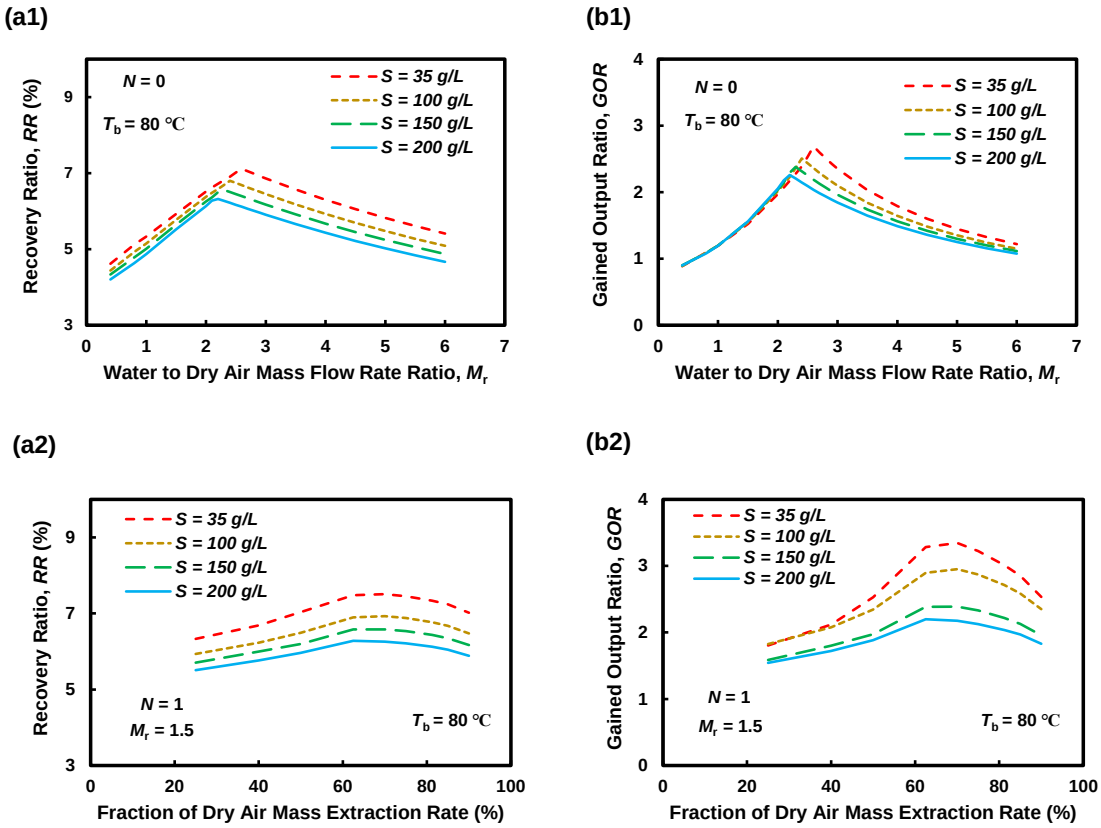

Figure 5.16: Effect of brine salinity on (a) *RR*, and (b) *GOR* of the Multi-string HDH system when there is no extraction line (first row) and when single extraction is applied (second row). T_b is fixed at 80 ℃. For the single extraction results we have M_r = 1.5.

5.3.6 Experimental results, zero extraction case (N = 0)

Figure 5.17 compares the experimental *GOR* (a), *RR* (b), and normalized entropy generation (c) values obtained for T_b = 80 ˚C and N = 0 with the predictions from the numerical analysis. As noted, *RR* is measured using both methods introduced earlier. Similarly, Fig. 5.17 (d) and (e) compare results at different inlet brine temperatures. Maximum *GOR* increases and maximum *RR* decreases as we lower the inlet brine temperature which is consistent with the predictions from our prior numerical analysis. The maximum *GOR* and *RR* we reach are 2.3 and 6.6 % which happen at T_b = 60 ℃ and T_b = 80 ℃, respectively. We see 20-25% difference between the peak performance from the experiments and the predicted values. This is due to heat loss to the ambient and non-uniformity in the airflow which results in having lower levels of water recovery and of heat recovery in our experiments compared to the predicted values. We later discuss these factors in more detail.

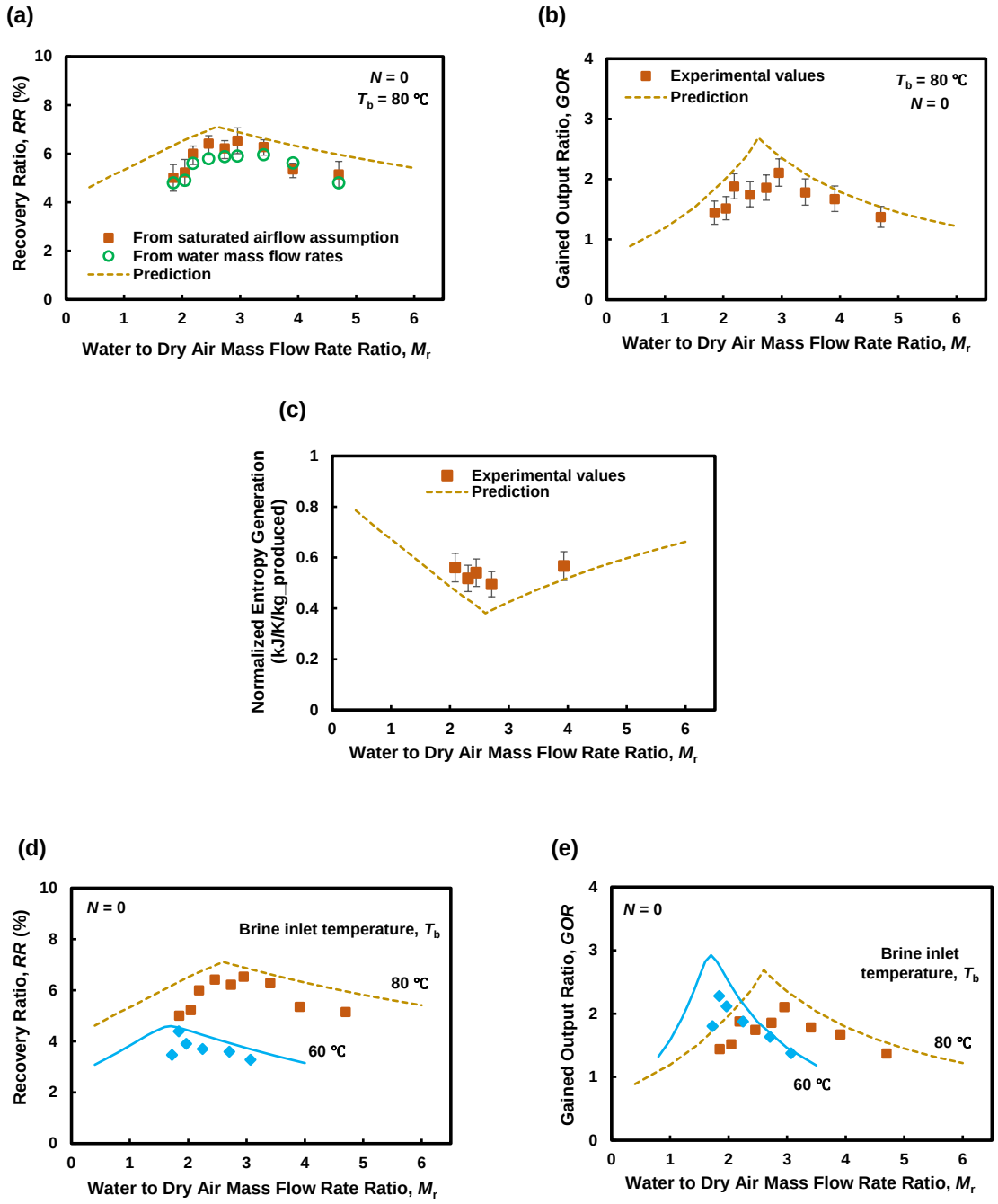

Figure 5.17: (a) *RR*, (b) *GOR*, and (c) normalized entropy generation of the constructed Multi-string HDH device with no extraction (i.e., $N = 0$) for $T_b = 80$ °C. (d) Comparing *RR*, and (e) comparing *GOR* for inlet brine temperatures of $T_b = 80$ °C, and 60 °C. Uncertainties are not shown in (d) and (e).

Figure 5.18 shows the temperature profile of air and water streams for three different operating points of M_r = 2.2 (low *M*r), M_r = 2.9 (intermediate M_r, maximum *GOR*), and M_r = 4.0 (high *M*r) when T_b is at 80 ˚C. Note that the prediction lines are using both inlet air and water temperatures as their boundary values for predicting the whole profile. From this figure, it can be inferred that, unlike the humidifier, the dehumidifier is not quite following the predictions hence resulting in degrading performance. Comparing inlet dehumidifier and outlet humidifier temperatures, we see the contribution of temperature drop in the connecting tubes on the total heat loss from the system to the ambient. Also, by looking at the trend in the prediction lines one can see that at high and low M_r values, the temperature difference becomes very small in a significant portion of the dehumidifier which means that not all the available heat and mass transfer area is being used in a proper way. In other words, this means that the dehumidifier is not being used at its full potential and the resulting temperature range, in fact, could be reproduced with an alternate exchanger with a smaller size. On the other hand, the intermediate M_r is giving the best performance since we are taking advantage of the most part of the dehumidifier. This result is consistent with previous discussions in the literature where it has been claimed that the best performance is obtained when the variance of the driving force (i.e., the stream-to-stream temperature difference) becomes minimum.

There are a few factors contributing to the experimental results deviating from the numerical predictions which we found after investigating the device in more details. As shown and discussed earlier, we characterized the performance of exchangers based on our experimental analysis on a scaled setup. We, however, used those analysis to predict the performance of the HDH setup having a much larger size. Furthermore, the temperature range that the air stream experiences in the prototype has become bigger compared to the scaled setup, which means the

effect of free convection has become more significant. This is an important point to note for the dehumidifier since the mainstream airflow and the free convection effect work in opposite directions causing some non-uniformities in the airflow. The negative effect of string misalignment on both waterflow and airflow is another reason contributing to the performance degradation. As the device size/height increases, it becomes more challenging to keep the strings straight and aligned. This is mainly because each string needs to get under higher tension and cotton strings may not withstand those levels of stress (i.e., tightness). We, however, can overcome these challenges by switching to plastic type strings and re-characterizing the performance of multi-string exchangers by conducting a comprehensive experimental study on those larger scale setups. By using plastic strings we will also be able to reduce the string pitch, down to ~4mm, which can help reducing the non-uniformity in the airflow and giving results that are closer to the prediction values.

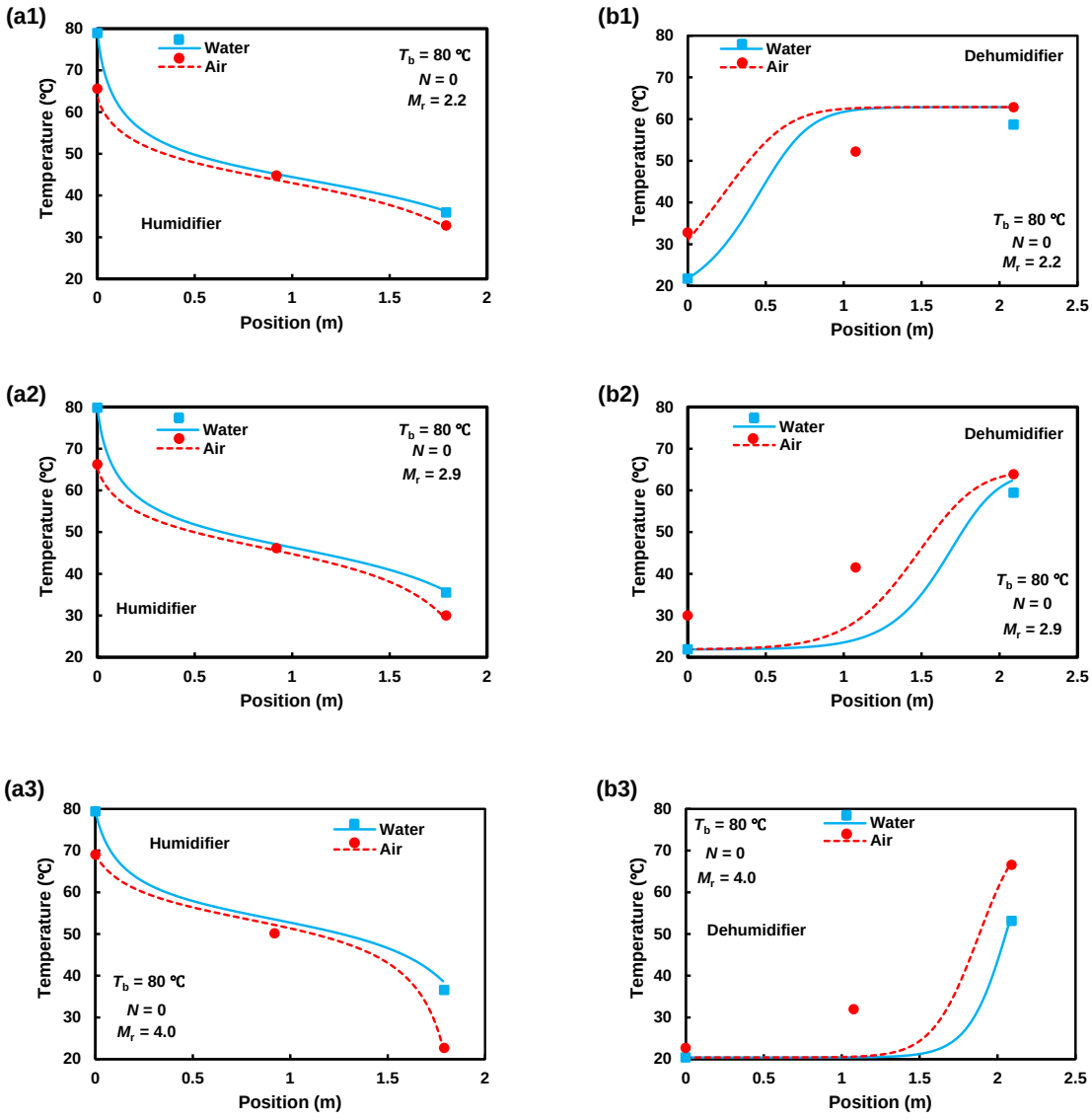

Figure 5.18: Temperature as a function of location for air and water streams in (a) humidifier and (b) dehumidifier for the case T_b = 80 ˚C, N = 0, and three M_r values of 2.2, 2.9, and 4.0. Solid symbols show the measured values, and the lines are obtained from the numerical modeling based on the streams inlet conditions, i.e., mass flow rates and temperatures.

5.3.7 Experimental results, single extraction case (N = 1)

Figure 5.19 shows result we obtain while enabling the extraction airline. The maximum *GOR* and *RR* we reach are 2.9 and 7.5. We observe ~26% and ~14% enhancement in both *GOR* and *RR*, respectively, compared to the no-extraction case. In addition to the problem with the heat loss to the ambient, non-perfect mixing of the air streams contribute to the deviation from the

predictions.

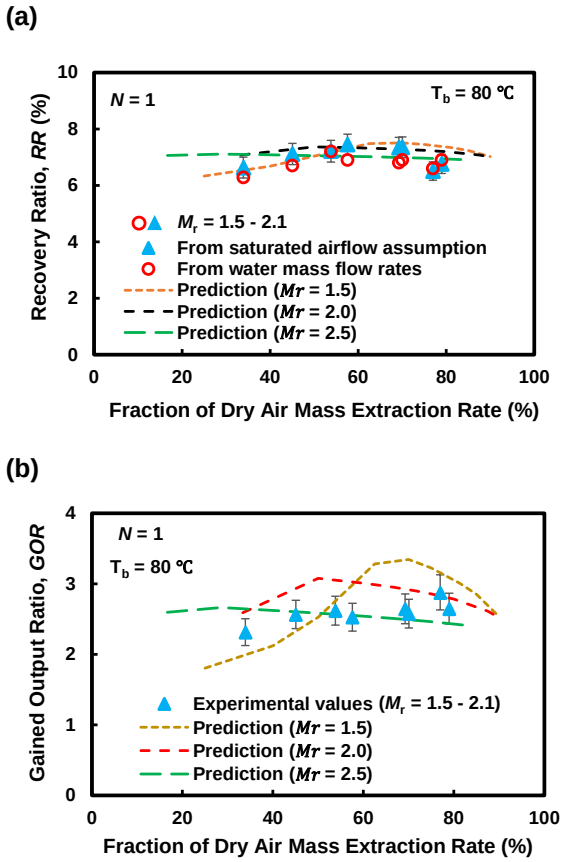

Figure 5.19: Experimental results (symbols) showing (a) *RR*, and (b) *GOR* as a function of air extraction from the intermediate point while the water mass flowrate to overall air mass flow circulation rate is within 1.5 to 2.1, and T_b is at 80 ℃. Dashed line shows the results from numerical prediction for M_r = 1.5.

5.3.8 Air-side pressure drop in multi-string heat/mass exchangers

Figure 5.20 shows the pressure drop due to friction, $(dP/dz)_f$, in a multi-string exchanger with three different pitches, 10 mm, 7 mm, and 5 mm. Symbols show the pressure drops measured from our experiments and the lines show predictions obtained from Eqs. (5.17) and (5.18). Although the results represent data for inlet water flow rate per cell of 0.06 g/s, the change in water flow rate even by factor of 2 has a negligible effect on the pressure drop.

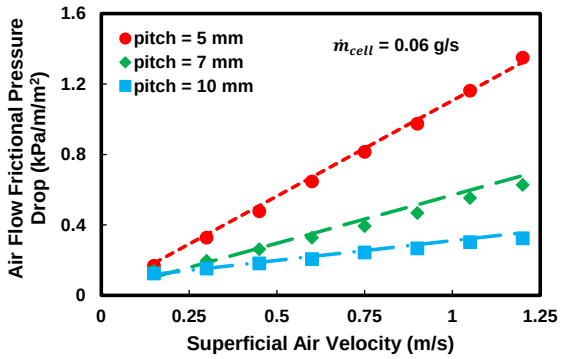

Figure 5.20: Pressure drop due to friction, $(dp/dz)_f$ per unit cross-section ($1/m^2$) per unit length (1/m) in a multi-string exchanger with three different pitches, 10 mm, 7 mm, and 5 mm. Symbols show the pressure drops measured from our experiments and the lines show predictions obtained from Eqs. (7) and (8). Water flow rate per cell is 0.06 g/s.

5.3.9 Effect of heat recovery on the overall performance

We already discussed the importance of heat recovery in an HDH system to maintain its thermal efficiency at a reasonable level. This, however, needs careful attention as we need to add another part (i.e., a heat exchanger) to preheat the new brine using the hot freshwater stream exiting the dehumidifier (refer to Fig. 5.23). Figure 5.21 shows how the *GOR* changes as a function of the effectiveness of the defined heat exchanger assuming the new brine is at 20 °C (T_i in Eq. (5.6)). Note that *RR* remains at a constant level as long as the temperature range and the applied flow rates do not change.

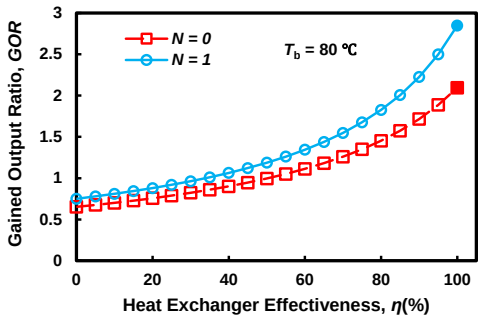

Figure 5.21: Effect of heat exchanger effectiveness on *GOR* of the multi-string HDH system for both no extraction and single extraction scenarios. Note that the lines with hollow symbols show projections based on the experimental values obtained in this project.

5.3.10 Effect of brine salinity on the overall performance

Figure 5.22 shows how *RR* and *GOR* change with brine salinity for the single extraction cases. This plot confirms that our prototype is capable of maintaining its performance within 23% of the peak *GOR* value even when a highly-saline brine stream at 100 gr /(kg water) salinity is fed to the system. We further validated our results by measuring the conductivity/concentration of the initial brine and the concentrated brine and calculating the resulting evaporation.

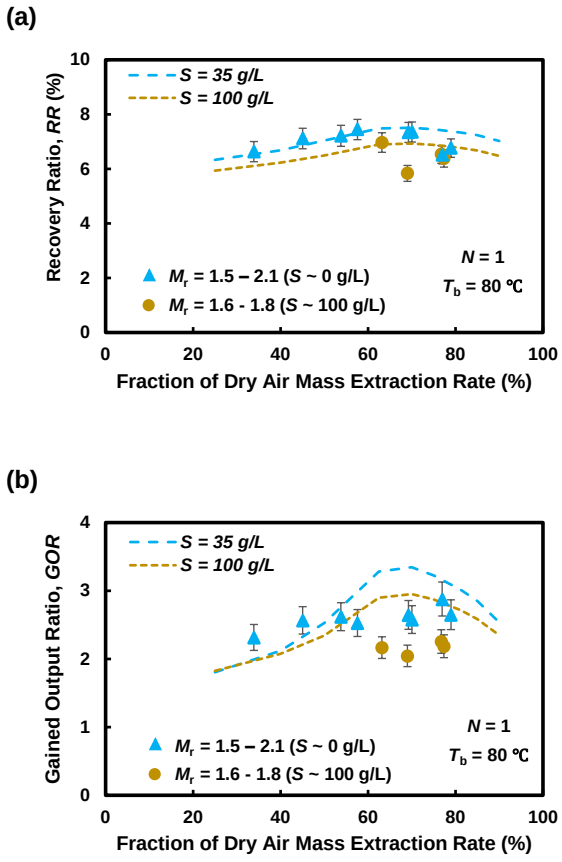

Figure 5.22: Effect of Brine salinity on (a) *RR* and (b) *GOR* of the multi-string HDH system for single extraction cases. Dashed lines show the predictions, and symbols are experimental values.

5.3.11 Balancing an HDH desalination System Optimization study

According to the previous thermodynamics discussion and aiming at achieving a *GOR* value of 7 or higher, we conduct and report the optimization study for an HDH system having two intermediate air extractions from the humidifier. During the optimization study, we consider the brine inlet temperature to be at 90 ˚C, the condensing water temperature to be at 20 ˚C, and the brine stream being fed to the system to be at sea level salinity (~ 35 g/ (kg water)). We therefore deal with six sub-sections where heat and mass transfer equations should be solved for each section separately. However, all these sub-sections are connected by their boundary values. For instance, the inlet temperature of the water stream at the mid-section of each device should be equal to the water temperature coming from the top-section. Using the simplified 1-D model introduced earlier, energy and mass conservation equations are solved for all the elements present in the desalination system in order to find out how the system would perform as a function of the physical parameters that are initially assigned. In this optimization model, we are considering two intermediate air stream extractions from humidifier where the extracted air streams join the dehumidifier main air stream at two intermediate injection points. Furthermore, perfect mixing condition is assumed at the injection points.

The assigned/given parameters are the pitch between the strings, brine inlet flow rate and temperature ($\dot{m}_{b.in}$, T_b), and dehumidifier water inlet flow rate and temperature ($\dot{m}_{cond.in}$, T_{cond}). It should be noted that, however, these values are assigned to a single cell (i.e., isolated string) in the humidifier and dehumidifier. Hence, for calculating the overall throughput of the desalination system, the total number of cells (i.e., strings) should be assigned.

A schematic of the desalination device showing the given and optimized parameters is presented in Fig. 5.23. Parameters highlighted in yellow are the optimization parameters which are the location of humid air extractions ($L_{H.1}$, $L_{H.2}$, $L_{H.3}$), the location of humid air injections ($L_{DH.1}$, $L_{DH.2}$, $L_{DH.3}$), and the amount of dry air mass flow rate in each section ($\dot{m}_{da.1}$, $\dot{m}_{da.2}$, $\dot{m}_{da.3}$) of humidifier/dehumidifier. Note that we have considered a total length of 3.5 meters for both devices. Figure 5.24 shows the flowchart of the optimization scheme.

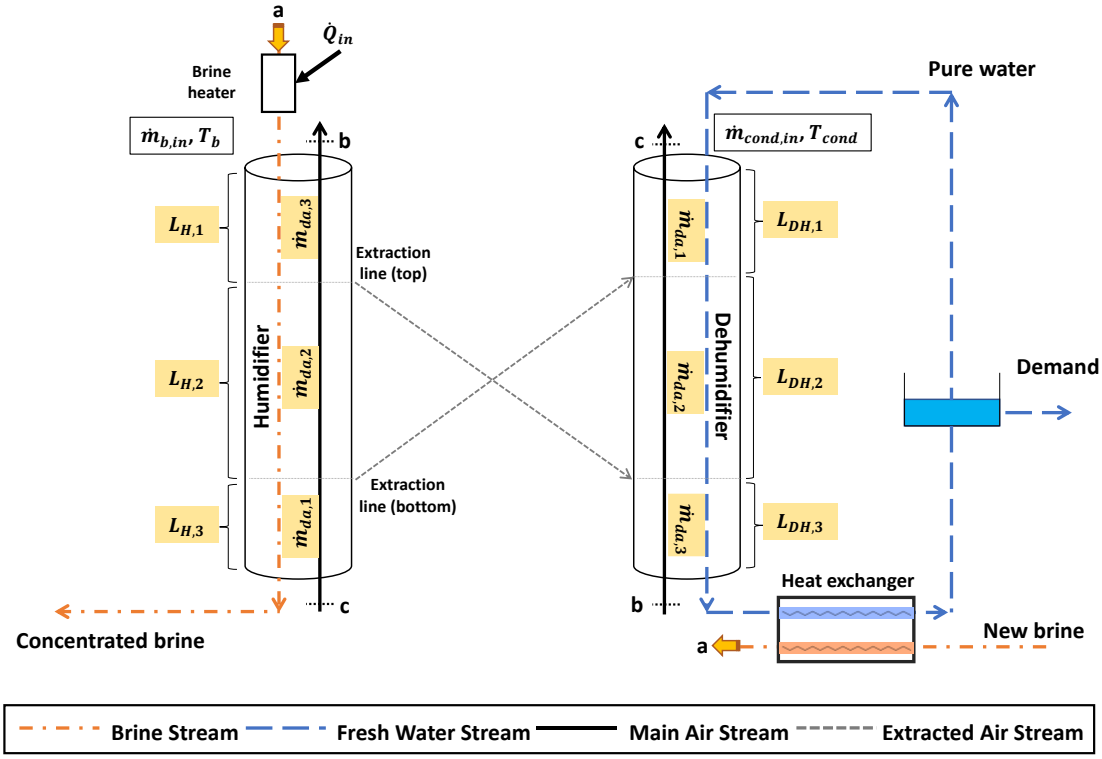

Figure 5.23: Multi-string HDH desalination system and the related optimization parameters. Same alphabets address the connecting points. Parameters highlighted in yellow are unknown during each optimization run.

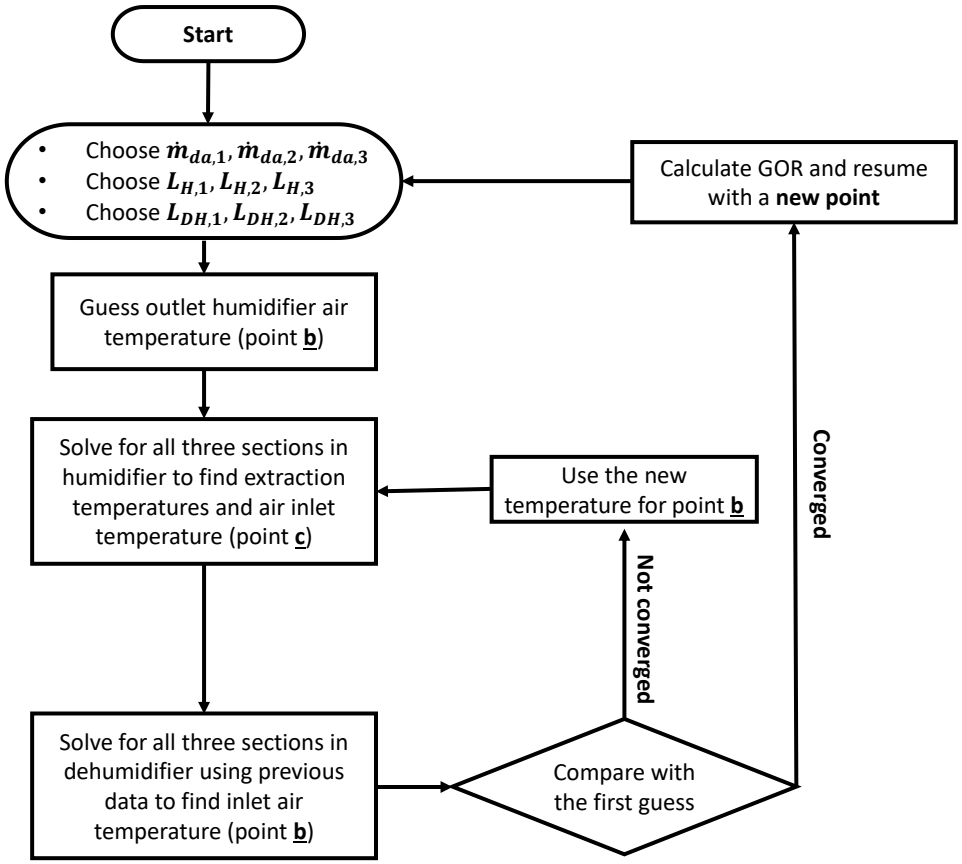

Figure 5.24: Flowchart of the optimization process. Points mentioned here refer to Figure 23.

We use the pattern search method to find the optimal design under the given set of constraints. Table 2 shows the parameters of the optimized system with a *GOR* of 7.5 and a recovery ratio of about 9.5% while taking advantage of two intermediate connections between the humidifier and the dehumidifier. Our proposed system has 3.5 meters tall humidifier and dehumidifier, and the length of each section is 0.5 m, 1.25 m, and 1.75 m from top to bottom for humidifier and from bottom to top for the dehumidifier. For this system we find optimum overall and intermediate M_r values of 1.3 and 3.5. Also, we realize applying 10% higher brine mass flow rate with respect to the water stream enhances the device's performance. Figure 5.25 shows the

performance of the system described in terms of *GOR*, *RR*, and entropy generation. Note that the overall and intermediate dry air mass flow rate values are considered to stay constant, but the dry air flow rate passing the top section of the humidifier changes as we change the amount of extraction. Also, by comparing the results with similar plots for zero and single-extraction cases (Fig. 5.11, Fig. 5.13), one can notice that adding another extraction line has lowered the normalized entropy generation rate which confirms our earlier statement that lowering the entropy generation is crucial for getting higher *GOR*.

Table 5.2: The optimized multi-string HDH system with two extractions

Parameter	Amount	Unit
Humidifier height ($L_{H.1}$, $L_{H.2}$, $L_{H.3}$)	3.5 (05, 1.25, 1.75)	m
Dehumidifier height ($L_{DH.1}$, $L_{DH.2}$, $L_{DH.3}$)	3.5 (1.75, 1.25, 0.5)	m
$T_{brine,in}$	90	℃
$T_{cond,in}$	20	℃
$M_{r,1} = \dot{m}_b/\dot{m}_{da.1}$	1.3	ratio
$M_{r,2} = \dot{m}_b/\dot{m}_{da.2}$	3.5	ratio
$M_{r,3} = \dot{m}_b/\dot{m}_{da.3}$	14.0	ratio

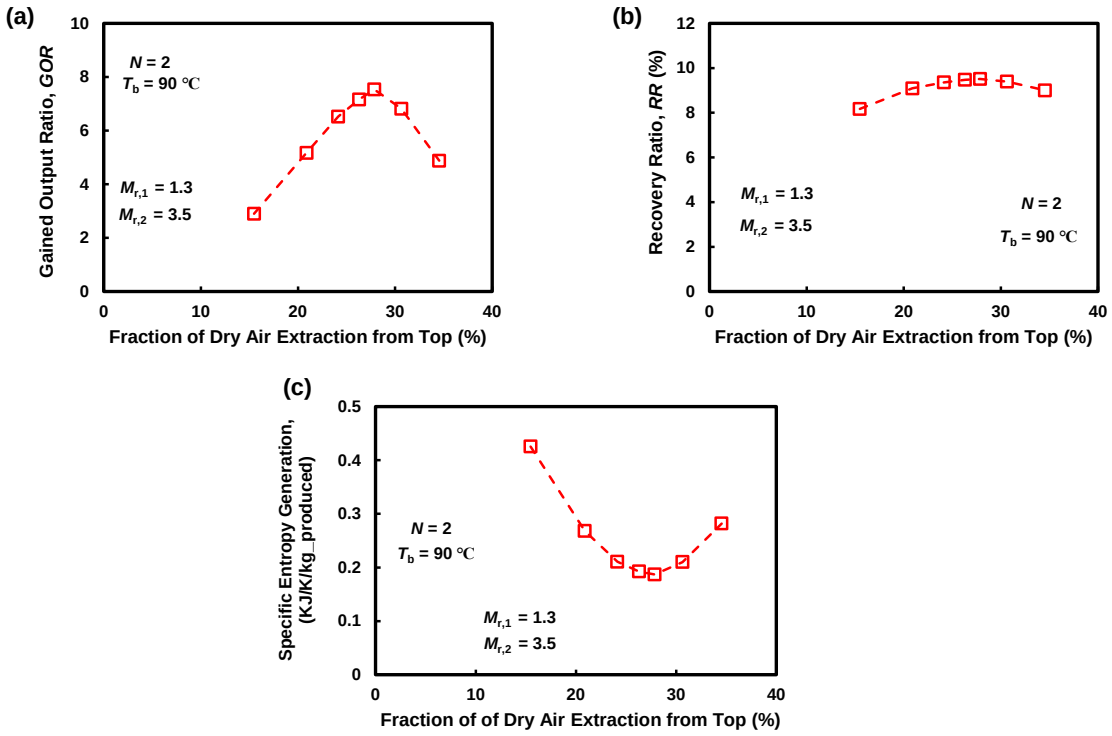

Figure 5.25: (a) *GOR*, (b) *RR*, and (c) normalized entropy generation of the proposed Multi-string HDH system with two intermediate extraction lines (i.e., $N = 2$) while $T_b = 90$ ℃, $M_{r,1} = 1.3$, $M_{r,2} = 3.5$, and brine to water mass flow rate ratio is 1.10.

5.3.12 Reliability study

In parallel to our numerical design study, we also designed and built a scaled device to help examine the effects of high-temperature and high-salinity water on the reliability of polymer strings. We used a nearly saturated (~250 g-NaCl / kg-water) synthetic NaCl-water solution as the feed water. Figure 5.26 shows the device constructed for the reliability study. A small pump is used to recirculate the saline water and an inline heater to control the water temperature. Preliminary experiments were performed to verify long-term (>2 weeks) operation of the pump, sealing, and temperature control. We used our observations and analysis on the reliability device to develop more promising approach for the prototype fabrication. We did not see any significant impact on the water follow while recirculating the hyper saline brine in the device. However,

pressure drop increased with time at the distributing nozzles resulting in higher water level in the top reservoir for providing same amount of flow rate. This problem was easily addressed by switching the hypersaline water with clean water to wash the contaminated nozzles. Another solution to this problem is using pressurized air to wipe out any contamination from the nozzles.

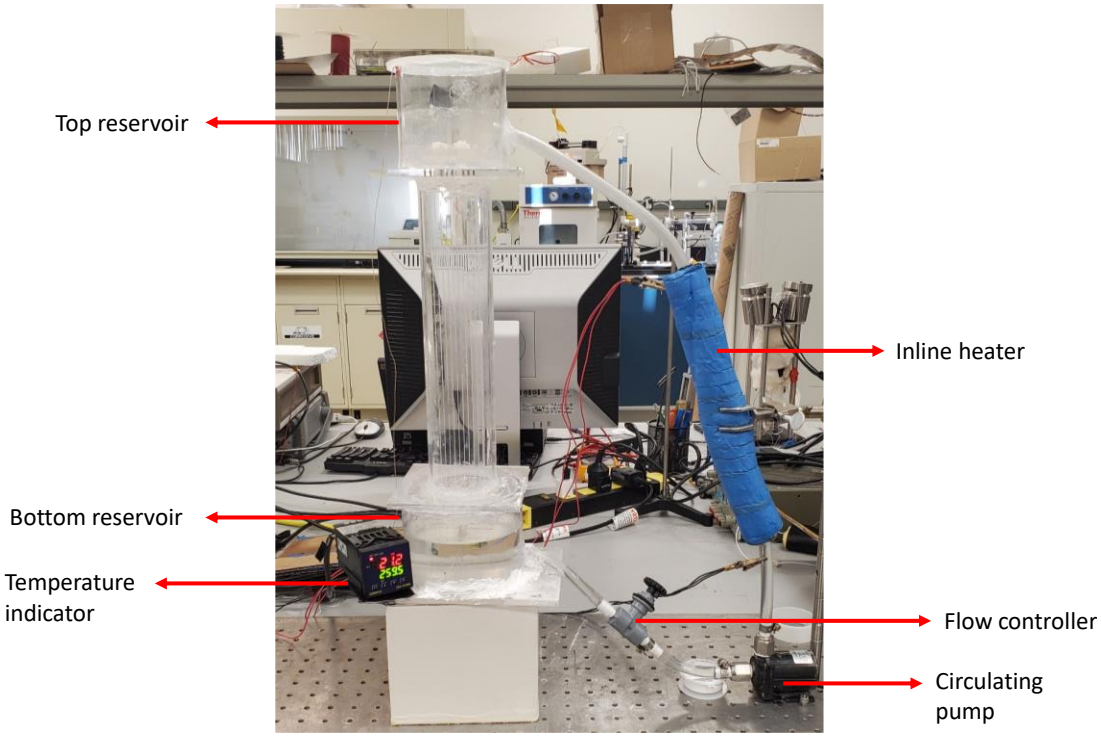

Figure 5.26: Scaled version of the multi-string exchanger for reliability study.

5.4 Summary

We present both numerical and experimental studies on an HDH desalination setup that works with novel string-based exchangers. The unique configuration of our exchangers enables high mass exchange rates per device volume which results in enhanced exchanger effectiveness and its highly porous structure allows air circulation at low electrical consumption rates. Our prototype reaches a *GOR* of 2.9 and an *RR* of 7.5% while providing fresh water at a rate of ~60

L/day. Considering the electrical consumption rate, this performance corresponds to an *SEEC* of ~2 kWh/m^3 which look promising compared to previous desalination prototypes, both thermally and non-thermally driven. Furthermore, as we discussed in the optimization section, there is still room for improvement and very high values (>7) of *GOR* can be achieved in a single-stage by utilizing larger devices (~3.5 meters-tall) that support two extraction air lines between the humidifier and the dehumidifier.

Table 5.3 provides a comparison from different aspects between the present work and other similar desalination prototypes studied by various research groups around the world. Based on the data shown, our design provides much more purified water compared to other efficient devices at the same exchanger size by nearly 2.7-fold. Note that, compared to the other works presented in this table, our device also offers a higher *GOR* in a single-stage single-pass configuration while running only on its own (i.e., not integrated with any other systems).

Also, the multi-string platform offers much lower pressure drop due to its highly porous structure (97.5% porosity) and can tolerate brackish waters with very high level of salinity while demanding a low-level maintenance. These ultimately result in producing fresh water at lower costs.

Table 5.3: Performance comparison among thermal desalination systems and the presented multi-string HDH system. All results are from experimental studies.

Desalination system type	Cylindrical Fresnel lens driven (HDH) [156]	Heat pump driven (HDH) [27]	Solar driven (HDH) [184]	Porous ball humidifiers (HDH) [155]	Multi-stage solar still [162]	Spiral wound membrane distillation [185]	4-stage vacuum membrane distillation [186]	Multi-String HDH (present work)
Temperature range (°C)	51-16	40-27.5	118-40	85-25	72-25	80-20	60-25	80-20
Air side pressure drop (Pa/m)	-----	------	-------	------	-----	------	------	6
Maximum *GOR*	2.1	4.07[1]	2.3	2.65	3.85[2]	2.53	2.79	**2.9**[3]
Maximum water recovery (%)	-----	4.9	-------	9.1	-----	4.6	40	7.5
Water production per humidifier volume ($m^3/day/m^3$)	------	2.36	0.16	1.0	2.77	1.09	------	**7.3**
Maximum salinity tolerance (gr/kg water)	-----	2.44	------	------	35	35	35	**>250**[4]
SEEC (kWh/m^3)	-----	312	------	------	-----	------	------	~2
Packing porosity (%)	78	------	------	------	------	80	-------	**97.5**
Humidifier packing specific area (m^2/m^3)	350	400	------	------	200	-----	-------	150

[1] This value is for the integrated system. The *GOR* value for the stand-alone HDH system has not been reported.
[2] This value is reported over the total 10-stage device which corresponds to ~0.4 *GOR* per stage.
[3] This value is for a stand-alone single-stage single-pass desalination system.
[4] This value comes from our reliability study.

Chapter 6

Summary and future work recommendations

6.1 Summary

This dissertation presents research on the characteristics and applications of wetting liquids flowing down thin vertical fibers and their interaction with small nozzles. Through a combined experimental and numerical study, we uncovered the crucial impact of nozzle geometry and liquid properties on the dynamics and statics of capillary-driven rise, an area largely overlooked in previous studies. Our proposed regime maps and analytical models accurately predict different capillary-driven flow regimes, evolution of droplet meniscus on a cylindrical nozzle, and their highest wetting height for any given case. Furthermore, our investigation on the effect of heat and/or mass exchange on flow regime of train of beads on a fiber demonstrated that stream-wise liquid property change can contribute to regime transition for a liquid film flowing on a thin vertical fiber. We proposed simplified mathematical modeling capable of predicting the flow regime transitions at relatively low computational cost.

We also made significant strides in the area of desalination, adapting our multi-string exchangers for a humidification-dehumidification approach to desalinating hypersaline water. Our fundamental thermodynamics analysis and simplified heat and mass transfer model for string-based exchangers allowed us to specify physical design parameters and ideal working conditions of the thermal desalination system. Our optimized design exhibited comparable

thermal efficiency and recovery rates compared to previous designs while producing higher water vapor per device volume at significantly low electrical consumption rates. Overall, our research has important implications for both the field of fluid mechanics and the sustainable management of water resources.

6.2 Future work recommendations

6.2.1 A comprehensive study on the effect of fiber thickness and nozzle size on heat/mass transfer

We have already performed a combination of experimental, numerical, and theoretical modeling study to quantify the amount of heat and/or mass transfer between the liquid films flowing down a thin fiber and a passing gas stream. The results showed increasing the liquid and/or the counter-flow gas stream velocity generally enhances the heat/mass exchanges at the interface. We also realize that using a different fiber and/or nozzle size changes both bead shapes and the train of beads characteristics (i.e., bead spacing, bead velocity, etc.). However, a comprehensive study is still needed to find an optimized fiber/nozzle size for a given liquid-gas combination and their respective flow rates to maximize the exchange rates. Such finding enables researchers in the field to better understand the necessary design considerations for string-based exchangers and to help with efficiently optimizing the multi-string design for various applications.

6.2.2 A double-extraction Humidification-Dehumidification desalination system using string-based heat/mass exchangers

As discussed in chapter 5, our multi-string HDH desalination system prototype, compared to the existing designs, exhibits superior performance in terms of evaporation/condensation rates per volume of the device with significantly lower air-stream pressure drop. We propose an enhanced version of the system we built which takes advantage of larger surface area and two intermediate extraction/injection lines to offer a much higher thermal efficiency and throughput, i.e., *GOR* ~ 7.5 and *RR* ~ 10%. This study would build upon the numerical prediction in this dissertation to experimentally examine the performance of the proposed desalination system. Although there are many numerical investigations in the literature on HDH systems with multiple interconnecting channels, this would potentially be the first experimental study on an HDH system that takes advantage of two extractions/injections to further enhance the *GOR* of an HDH desalination system.

References

[1] A. Sadeghpour, Z. Zeng, H. Ji, N. D. Ebrahimi, A. L. Bertozzi, and Y. S. Ju, "Water vapor capturing using an array of traveling liquid beads for desalination and water treatment," *Science Advances*, vol. 5, no. 4, 2019.

[2] A. Sadeghpour *et al.*, "Experimental study of a string-based counterflow wet electrostatic precipitator for collection of fine and ultrafine particles," *null*, pp. 1–15, Jan. 2021, doi: 10.1080/10962247.2020.1869627.

[3] Z. Zeng, A. Sadeghpour, and Y. S. Ju, "Thermohydraulic characteristics of a multi-string direct-contact heat exchanger," *International Journal of Heat and Mass Transfer*, vol. 126, pp. 536–544, 2018.

[4] Z. Zeng, A. Sadeghpour, and Y. S. Ju, "A highly effective multi-string humidifier with a low gas stream pressure drop for desalination," *Desalination*, vol. 449, pp. 92–100, Jan. 2019, doi: 10.1016/j.desal.2018.10.017.

[5] E. Sedighi, Z. Zeng, A. Sadeghpour, H. Ji, Y. S. Ju, and A. L. Bertozzi, "Capillary-Driven Rise of Well-Wetting Liquid on the Outer Surface of Cylindrical Nozzles," *Langmuir*, vol. 37, no. 35, pp. 10413–10423, Sep. 2021, doi: 10.1021/acs.langmuir.1c01096.

[6] H. Ji, C. Falcon, E. Sedighi, A. Sadeghpour, Y. S. Ju, and A. L. Bertozzi, "Thermally-driven coalescence in thin liquid film flowing down a fibre," *Journal of Fluid Mechanics*, vol. 916, Jun. 2021, doi: 10.1017/jfm.2021.198.

[7] B. Ambravaneswaran, H. J. Subramani, S. D. Phillips, and O. A. Basaran, "Dripping-Jetting Transitions in a Dripping Faucet," *Phys. Rev. Lett.*, vol. 93, no. 3, p. 034501, Jul. 2004, doi: 10.1103/PhysRevLett.93.034501.

[8] H. J. Subramani, H. K. Yeoh, R. Suryo, Q. Xu, B. Ambravaneswaran, and O. A. Basaran, "Simplicity and complexity in a dripping faucet," *Physics of Fluids*, vol. 18, no. 3, p. 032106, Mar.

2006, doi: 10.1063/1.2185111.

[9] M. Rubio-Rubio, P. Taconet, and A. Sevilla, “Dripping dynamics and transitions at high Bond numbers,” *International Journal of Multiphase Flow*, vol. 104, pp. 206–213, Jul. 2018, doi: 10.1016/j.ijmultiphaseflow.2018.02.017.

[10] W. Huang *et al.*, “Nozzle tip wetting in gasoline direct injection injector and its link with nozzle internal flow,” *International Journal of Engine Research*, vol. 21, no. 2, pp. 340–351, Feb. 2020, doi: 10.1177/1468087419869774.

[11] J. Hélie, N. Lamarque, J.-L. Fremaux, P. Serrecchia, M. Khosravi, and O. Berkemeier, “The process of tip wetting at the spray injection end,” *International Journal of Engine Research*, vol. 22, no. 1, pp. 125–139, Jan. 2021, doi: 10.1177/1468087419840842.

[12] Z. Zeng, A. Sadeghpour, G. Warrier, and Y. S. Ju, “Experimental study of heat transfer between thin liquid films flowing down a vertical string in the Rayleigh-Plateau instability regime and a counterflowing gas stream,” *International Journal of Heat and Mass Transfer*, vol. 108, Part A, pp. 830–840, May 2017, doi: 10.1016/j.ijheatmasstransfer.2016.12.066.

[13] Z. Zeng, A. Sadeghpour, and Y. S. Ju, “Thermohydraulic characteristics of a multi-string direct-contact heat exchanger,” *International Journal of Heat and Mass Transfer*, vol. 126, pp. 536–544, Nov. 2018, doi: 10.1016/j.ijheatmasstransfer.2018.05.060.

[14] B. Chang, G. Nave, and S. Jung, “Drop formation from a wettable nozzle,” *Communications in Nonlinear Science and Numerical Simulation*, vol. 17, no. 5, pp. 2045–2051, May 2012, doi: 10.1016/j.cnsns.2011.08.023.

[15] I. L. Kliakhandler, S. H. Davis, and S. G. Bankoff, “Viscous beads on vertical fibre,” *Journal of Fluid Mechanics*, vol. 429, pp. 381–390, Feb. 2001, doi: 10.1017/S0022112000003268.

[16] A. Sadeghpour, Z. Zeng, and Y. S. Ju, “Effects of Nozzle Geometry on the Fluid Dynamics of Thin Liquid Films Flowing down Vertical Strings in the Rayleigh–Plateau Regime,” *Langmuir*, vol. 33, no. 25, pp. 6292–6299, Jun. 2017, doi: 10.1021/acs.langmuir.7b01277.

[17] C. T. Gabbard and J. B. Bostwick, “Scaling analysis of the Plateau–Rayleigh instability in thin

film flow down a fiber," *Exp Fluids*, vol. 62, no. 7, p. 141, Jun. 2021, doi: 10.1007/s00348-021-03234-3.

[18] R. Liu, Z. Ding, and X. Chen, "The effect of thermocapillarity on the dynamics of an exterior coating film flow down a fibre subject to an axial temperature gradient," *International Journal of Heat and Mass Transfer*, vol. 123, pp. 718–727, Aug. 2018, doi: 10.1016/j.ijheatmasstransfer.2018.03.023.

[19] K. Hattori, M. Ishikawa, and Y. H. Mori, "Strings of liquid beads for gas-liquid contact operations," *AIChE Journal*, vol. 40, no. 12, pp. 1983–1992, 1994, doi: 10.1002/aic.690401209.

[20] H. Chinju, K. Uchiyama, and Y. H. Mori, "'String-of-beads' flow of liquids on vertical wires for gas absorption," *AIChE Journal*, vol. 46, no. 5, pp. 937–945, 2000, doi: 10.1002/aic.690460508.

[21] H. Migita, K. Soga, and Y. H. Mori, "Gas absorption in a wetted-wire column," *AIChE Journal*, vol. 51, no. 8, pp. 2190–2198, 2005, doi: 10.1002/aic.10483.

[22] T. Nozaki, N. Kaji, and Y. H. Mori, "Heat Transfer to a Liquid Flowing Down Vertical Wires Hanging in a Hot Gas Stream: an Experimental Study of a New Means of Thermal Energy Recovery," presented at the International Heat Transfer Conference 11, 1998. doi: 10.1615/IHTC11.2160.

[23] F. Alnaimat, M. Ziauddin, and B. Mathew, "A review of recent advances in humidification and dehumidification desalination technologies using solar energy," *Desalination*, vol. 499, p. 114860, Feb. 2021, doi: 10.1016/j.desal.2020.114860.

[24] H. Sharon and K. S. Reddy, "A review of solar energy driven desalination technologies," *Renewable and Sustainable Energy Reviews*, vol. 41, pp. 1080–1118, Jan. 2015, doi: 10.1016/j.rser.2014.09.002.

[25] M. Eyvaz and E. Yüksel, *Desalination and Water Treatment*. BoD – Books on Demand, 2018.

[26] P. N. Govindan, S. Lam, and J. M. G. St, "Humidification-dehumidification desalination systems and methods," CA2986577A1, Nov. 24, 2016 [Online]. Available: https://patents.google.com/patent/CA2986577A1/en

[27] D. U. Lawal and N. A. A. Qasem, “Humidification-dehumidification desalination systems driven by thermal-based renewable and low-grade energy sources: A critical review,” *Renewable and Sustainable Energy Reviews*, vol. 125, p. 109817, Jun. 2020, doi: 10.1016/j.rser.2020.109817.

[28] M. Shatat and S. B. Riffat, “Water desalination technologies utilizing conventional and renewable energy sources,” *Int J Low-Carbon Tech*, vol. 9, no. 1, pp. 1–19, Mar. 2014, doi: 10.1093/ijlct/cts025.

[29] K. P. Lee, T. C. Arnot, and D. Mattia, “A review of reverse osmosis membrane materials for desalination—Development to date and future potential,” *Journal of Membrane Science*, vol. 370, no. 1, pp. 1–22, Mar. 2011, doi: 10.1016/j.memsci.2010.12.036.

[30] G. Kang and Y. Cao, “Development of antifouling reverse osmosis membranes for water treatment: A review,” *Water Research*, vol. 46, no. 3, pp. 584–600, Mar. 2012, doi: 10.1016/j.watres.2011.11.041.

[31] M. Qasim, M. Badrelzaman, N. N. Darwish, N. A. Darwish, and N. Hilal, “Reverse osmosis desalination: A state-of-the-art review,” *Desalination*, vol. 459, pp. 59–104, Jun. 2019, doi: 10.1016/j.desal.2019.02.008.

[32] J. Kucera, *Reverse Osmosis: Industrial Processes and Applications*. John Wiley & Sons, 2015.

[33] L. F. Greenlee, D. F. Lawler, B. D. Freeman, B. Marrot, and P. Moulin, “Reverse osmosis desalination: Water sources, technology, and today’s challenges,” *Water Research*, vol. 43, no. 9, pp. 2317–2348, May 2009, doi: 10.1016/j.watres.2009.03.010.

[34] K. Park, J. Kim, D. R. Yang, and S. Hong, “Towards a low-energy seawater reverse osmosis desalination plant: A review and theoretical analysis for future directions,” *Journal of Membrane Science*, vol. 595, p. 117607, Feb. 2020, doi: 10.1016/j.memsci.2019.117607.

[35] E. J. Okampo and N. Nwulu, “Optimisation of renewable energy powered reverse osmosis desalination systems: A state-of-the-art review,” *Renewable and Sustainable Energy Reviews*, vol. 140, p. 110712, Apr. 2021, doi: 10.1016/j.rser.2021.110712.

[36] S. Burn *et al.*, “Desalination techniques — A review of the opportunities for desalination in

agriculture," *Desalination*, vol. 364, pp. 2–16, May 2015, doi: 10.1016/j.desal.2015.01.041.

[37] M. Prajapati *et al.*, "Geothermal-solar integrated groundwater desalination system: Current status and future perspective," *Groundwater for Sustainable Development*, vol. 12, p. 100506, Feb. 2021, doi: 10.1016/j.gsd.2020.100506.

[38] M. Alsehli, "Experimental Validation of a Solar Powered Multistage Flash Desalination Unit with Alternate Storage Tanks," *Water*, vol. 13, no. 16, Art. no. 16, Jan. 2021, doi: 10.3390/w13162143.

[39] A. Giwa, N. Akther, A. A. Housani, S. Haris, and S. W. Hasan, "Recent advances in humidification dehumidification (HDH) desalination processes: Improved designs and productivity," *Renewable and Sustainable Energy Reviews*, vol. 57, pp. 929–944, May 2016, doi: 10.1016/j.rser.2015.12.108.

[40] M. M. Farid, S. Parekh, J. R. Selman, and S. Al-Hallaj, "Solar desalination with a humidification-dehumidification cycle: mathematical modeling of the unit," *Desalination*, vol. 151, no. 2, pp. 153–164, Jan. 2003, doi: 10.1016/S0011-9164(02)00994-3.

[41] S. Parekh, M. M. Farid, J. R. Selman, and S. Al-hallaj, "Solar desalination with a humidification-dehumidification technique — a comprehensive technical review," *Desalination*, vol. 160, no. 2, pp. 167–186, Jan. 2004, doi: 10.1016/S0011-9164(04)90007-0.

[42] A. E. Kabeel, M. H. Hamed, Z. M. Omara, and S. W. Sharshir, "Experimental study of a humidification-dehumidification solar technique by natural and forced air circulation," *Energy*, vol. 68, pp. 218–228, Apr. 2014, doi: 10.1016/j.energy.2014.02.094.

[43] K. M. Chehayeb, G. P. Narayan, S. M. Zubair, and J. H. Lienhard V, "Thermodynamic balancing of a fixed-size two-stage humidification dehumidification desalination system," *Desalination*, vol. 369, pp. 125–139, Aug. 2015, doi: 10.1016/j.desal.2015.04.021.

[44] K. M. Chehayeb, G. Prakash Narayan, S. M. Zubair, and J. H. Lienhard V, "Use of multiple extractions and injections to thermodynamically balance the humidification dehumidification desalination system," *International Journal of Heat and Mass Transfer*, vol. 68, pp. 422–434, Jan. 2014, doi: 10.1016/j.ijheatmasstransfer.2013.09.025.

[45] R. K. McGovern, G. P. Thiel, G. Prakash Narayan, S. M. Zubair, and J. H. Lienhard, "Performance limits of zero and single extraction humidification-dehumidification desalination systems," *Applied Energy*, vol. 102, pp. 1081–1090, Feb. 2013, doi: 10.1016/j.apenergy.2012.06.025.

[46] J. Eggers, "Nonlinear dynamics and breakup of free-surface flows," *Rev. Mod. Phys.*, vol. 69, no. 3, pp. 865–930, Jul. 1997, doi: 10.1103/RevModPhys.69.865.

[47] O. A. Basaran, "Small-scale free surface flows with breakup: Drop formation and emerging applications," *AIChE Journal*, vol. 48, no. 9, pp. 1842–1848, 2002, doi: 10.1002/aic.690480902.

[48] P. Coullet, L. Mahadevan, and C. S. Riera, "Hydrodynamical models for the chaotic dripping faucet," *Journal of Fluid Mechanics*, vol. 526, pp. 1–17, Mar. 2005, doi: 10.1017/S0022112004002307.

[49] A. Taur, P. Doshi, and H. K. Yeoh, "Dripping dynamics of Newtonian liquids from a tilted nozzle," *European Journal of Mechanics - B/Fluids*, vol. 51, pp. 8–15, May 2015, doi: 10.1016/j.euromechflu.2014.12.004.

[50] J. Dinic and V. Sharma, "Computational analysis of self-similar capillary-driven thinning and pinch-off dynamics during dripping using the volume-of-fluid method," *Physics of Fluids*, vol. 31, no. 2, p. 021211, Jan. 2019, doi: 10.1063/1.5061715.

[51] A. Sack and T. Pöschel, "Dripping faucet in extreme spatial and temporal resolution," *American Journal of Physics*, vol. 85, no. 9, pp. 649–654, Aug. 2017, doi: 10.1119/1.4979657.

[52] T. N. Nogueira, F. a. C. Pereira, J. Procopio, and J. C. Sartorelli, "Dripping faucet dynamics in a nonuniform electric field," *Chaos*, vol. 28, no. 11, p. 113101, Nov. 2018, doi: 10.1063/1.5040757.

[53] P.-H. Tsai and A.-B. Wang, "Classification and Prediction of Dripping Drop Size for a Wide Range of Nozzles by Wetting Diameter," *Langmuir*, vol. 35, no. 13, pp. 4763–4775, Apr. 2019, doi: 10.1021/acs.langmuir.8b04228.

[54] D. Gardini, M. Blosi, C. Zanelli, and M. Dondi, "Ceramic Ink-Jet Printing for Digital Decoration: Physical Constraints for Ink Design," *Journal of Nanoscience and Nanotechnology*, vol. 15, no. 5,

pp. 3552–3561, May 2015, doi: 10.1166/jnn.2015.9857.

[55] M. Rosello, S. Sur, B. Barbet, and J. P. Rothstein, “Dripping-onto-substrate capillary breakup extensional rheometry of low-viscosity printing inks,” *Journal of Non-Newtonian Fluid Mechanics*, vol. 266, pp. 160–170, Apr. 2019, doi: 10.1016/j.jnnfm.2019.03.006.

[56] S. Phillips, R. Leighton, N. Smith, and R. Tuchreio, “Ink-jet printer comprising a structure to eliminate ink dripping,” US8070277B2, Dec. 06, 2011 Accessed: Jul. 09, 2019. [Online]. Available: https://patents.google.com/patent/US8070277B2/en

[57] B.-J. de Gans and U. S. Schubert, “Inkjet Printing of Well-Defined Polymer Dots and Arrays,” *Langmuir*, vol. 20, no. 18, pp. 7789–7793, Aug. 2004, doi: 10.1021/la049469o.

[58] J. Sun *et al.*, “Patterning a Superhydrophobic Area on a Facile Fabricated Superhydrophilic Layer Based on an Inkjet-Printed Water-Soluble Polymer Template,” *Langmuir*, vol. 36, no. 33, pp. 9952–9959, Aug. 2020, doi: 10.1021/acs.langmuir.0c01769.

[59] A. V. Bazilevsky, A. L. Yarin, and C. M. Megaridis, “Co-electrospinning of Core−Shell Fibers Using a Single-Nozzle Technique,” *Langmuir*, vol. 23, no. 5, pp. 2311–2314, Feb. 2007, doi: 10.1021/la063194q.

[60] S. Takamatsu, T. Imai, T. Yamashita, T. Kobayashi, K. Miyake, and T. Itoh, “Flexible fabric keyboard with conductive polymer-coated fibers,” in *2011 IEEE SENSORS*, Oct. 2011, pp. 659–662. doi: 10.1109/ICSENS.2011.6127391.

[61] A. Bidoret, E. Martins, B. P. De Smet, and D. Poncelet, “Cell Microencapsulation: Dripping Methods,” in *Cell Microencapsulation: Methods and Protocols*, E. C. Opara, Ed. New York, NY: Springer New York, 2017, pp. 43–55. doi: 10.1007/978-1-4939-6364-5_3.

[62] J. Xie and C.-H. Wang, “Electrospray in the dripping mode for cell microencapsulation,” *Journal of Colloid and Interface Science*, vol. 312, no. 2, pp. 247–255, Aug. 2007, doi: 10.1016/j.jcis.2007.04.023.

[63] P. W. Chen, G. Cadisch, and A. R. Studart, “Encapsulation of Aliphatic Amines Using Microfluidics,” *Langmuir*, vol. 30, no. 9, pp. 2346–2350, Mar. 2014, doi: 10.1021/la500037d.

[64] B. G. De Geest, J. P. Urbanski, T. Thorsen, J. Demeester, and S. C. De Smedt, “Synthesis of Monodisperse Biodegradable Microgels in Microfluidic Devices,” *Langmuir*, vol. 21, no. 23, pp. 10275–10279, Nov. 2005, doi: 10.1021/la051527y.

[65] Y. Zhao, M. T. Carvajal, Y.-Y. Won, and M. T. Harris, “Preparation of Calcium Alginate Microgel Beads in an Electrodispersion Reactor Using an Internal Source of Calcium Carbonate Nanoparticles,” *Langmuir*, vol. 23, no. 25, pp. 12489–12496, Dec. 2007, doi: 10.1021/la701795y.

[66] D. W. Bousfield, R. Keunings, G. Marrucci, and M. M. Denn, “Nonlinear analysis of the surface tension driven breakup of viscoelastic filaments,” *Journal of Non-Newtonian Fluid Mechanics*, vol. 21, no. 1, pp. 79–97, Jan. 1986, doi: 10.1016/0377-0257(86)80064-7.

[67] S. D. R. Wilson, “The slow dripping of a viscous fluid,” *Journal of Fluid Mechanics*, vol. 190, pp. 561–570, May 1988, doi: 10.1017/S0022112088001454.

[68] J. Eggers and T. F. Dupont, “Drop formation in a one-dimensional approximation of the Navier–Stokes equation,” *Journal of Fluid Mechanics*, vol. 262, pp. 205–221, Oct. 1994, doi: 10.1017/S0022112094000480.

[69] X. Zhang and O. A. Basaran, “An experimental study of dynamics of drop formation,” *Physics of Fluids*, vol. 7, no. 6, pp. 1184–1203, Jun. 1995, doi: 10.1063/1.868577.

[70] J. R. Richards, A. N. Beris, and A. M. Lenhoff, “Drop formation in liquid–liquid systems before and after jetting,” *Physics of Fluids*, vol. 7, no. 11, pp. 2617–2630, Nov. 1995, doi: 10.1063/1.868710.

[71] D. F. Zhang and H. A. Stone, “Drop formation in viscous flows at a vertical capillary tube,” *Physics of Fluids*, vol. 9, no. 8, pp. 2234–2242, Aug. 1997, doi: 10.1063/1.869346.

[72] E. D. Wilkes, S. D. Phillips, and O. A. Basaran, “Computational and experimental analysis of dynamics of drop formation,” *Physics of Fluids*, vol. 11, no. 12, pp. 3577–3598, Dec. 1999, doi: 10.1063/1.870224.

[73] X. Zhang, “Dynamics of Growth and Breakup of Viscous Pendant Drops into Air,” *Journal of Colloid and Interface Science*, vol. 212, no. 1, pp. 107–122, Apr. 1999, doi:

10.1006/jcis.1998.6047.

[74] X. Zhang, “Dynamics of drop formation in viscous flows,” *Chemical Engineering Science*, vol. 54, no. 12, pp. 1759–1774, Jun. 1999, doi: 10.1016/S0009-2509(99)00027-5.

[75] B. Ambravaneswaran, S. D. Phillips, and O. A. Basaran, “Theoretical Analysis of a Dripping Faucet,” *Phys. Rev. Lett.*, vol. 85, no. 25, pp. 5332–5335, Dec. 2000, doi: 10.1103/PhysRevLett.85.5332.

[76] K. Kiyono and N. Fuchikami, “Dripping faucet dynamics by an improved mass-spring model,” *Journal of the Physical Society of Japan*, vol. 68, no. 10, pp. 3259–3270, 1999.

[77] A. D’Innocenzo, F. Paladini, and L. Renna, “Effects of geometrical parameters on dripping from cylindrical nozzles,” *Physica A: Statistical Mechanics and its Applications*, vol. 338, no. 1, pp. 272–276, Jul. 2004, doi: 10.1016/j.physa.2004.02.051.

[78] A. D’Innocenzo, F. Paladini, and L. Renna, “Experimental study of dripping dynamics,” *Phys. Rev. E*, vol. 65, no. 5, p. 056208, Apr. 2002, doi: 10.1103/PhysRevE.65.056208.

[79] E. I. Franses, O. A. Basaran, and C.-H. Chang, “Techniques to measure dynamic surface tension,” *Current Opinion in Colloid & Interface Science*, vol. 1, no. 2, pp. 296–303, Apr. 1996, doi: 10.1016/S1359-0294(96)80018-5.

[80] O. E. Yildirim, Q. Xu, and O. A. Basaran, “Analysis of the drop weight method,” *Physics of Fluids*, vol. 17, no. 6, p. 062107, Jun. 2005, doi: 10.1063/1.1938227.

[81] S. V. Patankar, *Numerical Heat Transfer and Fluid Flow*. Boca Raton: CRC Press, 2018. doi: 10.1201/9781482234213.

[82] H. K. Versteeg and W. Malalasekera, *An introduction to computational fluid dynamics: the finite volume method*, 2nd ed. Pearson education, 2007.

[83] ANSYS, Inc, *ANSYS Fluent Theory Guide*, 15.0. 2013. Accessed: Jun. 14, 2021. [Online]. Available: http://www.pmt.usp.br/academic/martoran/notasmodelosgrad/ANSYS%20Fluent%20Theory%20Guide%2015.pdf

[84] J. U. Brackbill, D. B. Kothe, and C. Zemach, “A continuum method for modeling surface tension,” *Journal of Computational Physics*, vol. 100, no. 2, pp. 335–354, Jun. 1992, doi: 10.1016/0021-9991(92)90240-Y.

[85] “Pure Silicone Fluids - Clearco Products.” http://www.clearcoproducts.com/pure-silicone-fluid.html

[86] “Rhodorsil® Oils.” https://www.silitech.ch/upload/complement_info_fournisseur_d/32.pdf

[87] C. A. Schneider, W. S. Rasband, and K. W. Eliceiri, “NIH Image to ImageJ: 25 years of image analysis,” *Nature Methods*, vol. 9, no. 7, Art. no. 7, Jul. 2012, doi: 10.1038/nmeth.2089.

[88] F. Jasinski, A. Alkhater, S. C. Thickett, R. H. Brinkhuis, and P. B. Zetterlund, “Estimation of Copolymer/Water Interfacial Tensions Using Pendant Drop Tensiometry,” *Langmuir*, vol. 34, no. 23, pp. 6835–6843, Jun. 2018, doi: 10.1021/acs.langmuir.8b00554.

[89] S.-Y. Lin and H.-F. Hwang, “Measurement of Low Interfacial Tension by Pendant Drop Digitization,” *Langmuir*, vol. 10, no. 12, pp. 4703–4709, Dec. 1994, doi: 10.1021/la00024a052.

[90] X. Wang, X. Peng, Y. Duan, and B. Wang, “Dynamics of Spreading of Liquid on Solid Surface,” *Chinese Journal of Chemical Engineering*, vol. 15, no. 5, pp. 730–737, Oct. 2007, doi: 10.1016/S1004-9541(07)60154-2.

[91] D. A. White and J. A. Tallmadge, “Static menisci on the outside of cylinders,” *Journal of Fluid Mechanics*, vol. 23, no. 2, pp. 325–335, Oct. 1965, doi: 10.1017/S0022112065001398.

[92] C. Duprat, C. Ruyer-Quil, S. Kalliadasis, and F. Giorgiutti-Dauphiné, “Absolute and Convective Instabilities of a Viscous Film Flowing Down a Vertical Fiber,” *Phys. Rev. Lett.*, vol. 98, no. 24, p. 244502, Jun. 2007, doi: 10.1103/PhysRevLett.98.244502.

[93] C. Ruyer-Quil and S. Kalliadasis, “Wavy regimes of film flow down a fiber,” *Phys. Rev. E*, vol. 85, no. 4, p. 046302, Apr. 2012, doi: 10.1103/PhysRevE.85.046302.

[94] H. Ji, C. Falcon, A. Sadeghpour, Z. Zeng, Y. S. Ju, and A. L. Bertozzi, “Dynamics of thin liquid films on vertical cylindrical fibres,” *Journal of Fluid Mechanics*, vol. 865, pp. 303–327, 2019.

[95] T. Nozaki, N. Kaji, and Y. H. Mod, “Heat Transfer to a Liquid Flowing Down Vertical Wires

Hanging in a Hot Gas Stream: an Experimental Study of a New Means of Thermal Energy Recovery," *HEAT TRANSFER*, vol. 6, pp. 63–68, 1998.

[96] Z. Zeng, A. Sadeghpour, G. Warrier, and Y. S. Ju, "Experimental study of heat transfer between thin liquid films flowing down a vertical string in the Rayleigh-Plateau instability regime and a counterflowing gas stream," *International Journal of Heat and Mass Transfer*, vol. 108, pp. 830–840, 2017.

[97] A. L. Frenkel, "Nonlinear Theory of Strongly Undulating Thin Films Flowing Down Vertical Cylinders," *EPL*, vol. 18, no. 7, p. 583, Apr. 1992, doi: 10.1209/0295-5075/18/7/003.

[98] H. CHANG and E. DEMEKHIN, "Mechanism for drop formation on a coated vertical fibre," *Journal of Fluid Mechanics*, vol. 380, pp. 233–255, 1999, doi: 10.1017/S0022112098003632.

[99] S. Kalliadasis and H.-C. Chang, "Drop formation during coating of vertical fibres," *Journal of Fluid Mechanics*, vol. 261, pp. 135–168, Feb. 1994, doi: 10.1017/S0022112094000297.

[100] R. V. Craster and O. K. Matar, "On viscous beads flowing down a vertical fibre," *Journal of Fluid Mechanics*, vol. 553, pp. 85–105, Apr. 2006, doi: 10.1017/S0022112006008706.

[101] H. Ji, R. Taranets, and M. Chugunova, "On travelling wave solutions of a model of a liquid film flowing down a fibre," *European Journal of Applied Mathematics*, vol. 33, no. 5, pp. 864–893, Oct. 2022, doi: 10.1017/S0956792521000255.

[102] Yu. Ya. Trifonov, "Steady-state traveling waves on the surface of a viscous liquid film falling down on vertical wires and tubes," *AIChE Journal*, vol. 38, no. 6, pp. 821–834, Jun. 1992, doi: 10.1002/aic.690380604.

[103] C. Ruyer-Quil, P. Treveleyan, F. Giorgiutti-Dauphiné, C. Duprat, and S. Kalliadasis, "Modelling film flows down a fibre," *Journal of Fluid Mechanics*, vol. 603, pp. 431–462, May 2008, doi: 10.1017/S0022112008001225.

[104] C. Duprat, C. Ruyer-Quil, and F. Giorgiutti-Dauphiné, "Spatial evolution of a film flowing down a fiber," *Physics of Fluids*, vol. 21, no. 4, p. 042109, Apr. 2009, doi: 10.1063/1.3119811.

[105] H. Ji, A. Sadeghpour, Y. S. Ju, and A. L. Bertozzi, "Modelling film flows down a fibre influenced

by nozzle geometry," *Journal of Fluid Mechanics*, vol. 901, p. R6, Oct. 2020, doi: 10.1017/jfm.2020.605.

[106] Yu. O. Kabova, V. V. Kuznetsov, and O. A. Kabov, "Temperature dependent viscosity and surface tension effects on deformations of non-isothermal falling liquid film," *International Journal of Heat and Mass Transfer*, vol. 55, no. 4, pp. 1271–1278, Jan. 2012, doi: 10.1016/j.ijheatmasstransfer.2011.09.020.

[107] C. Ruyer-Quil, B. Scheid, S. Kalliadasis, M. G. Velarde, and R. K. Zeytounian, "Thermocapillary long waves in a liquid film flow. Part 1. Low-dimensional formulation," *Journal of Fluid Mechanics*, vol. 538, pp. 199–222, Sep. 2005, doi: 10.1017/S0022112005005422.

[108] O. Haimovich and A. Oron, "Nonlinear dynamics of a thin nonisothermal liquid film on an axially oscillating cylindrical surface," *Phys. Rev. E*, vol. 84, no. 6, p. 061605, Dec. 2011, doi: 10.1103/PhysRevE.84.061605.

[109] R. Liu, Z. Ding, and Z. Zhu, "Thermocapillary effect on the absolute and convective instabilities of film flows down a fibre," *International Journal of Heat and Mass Transfer*, vol. 112, pp. 918–925, Sep. 2017, doi: 10.1016/j.ijheatmasstransfer.2017.05.030.

[110] Z. Ding and T. N. Wong, "Three-dimensional dynamics of thin liquid films on vertical cylinders with Marangoni effect," *Physics of Fluids*, vol. 29, no. 1, p. 011701, Jan. 2017, doi: 10.1063/1.4974076.

[111] Z. Ding, R. Liu, T. N. Wong, and C. Yang, "Absolute instability induced by Marangoni effect in thin liquid film flows on vertical cylindrical surfaces," *Chemical Engineering Science*, vol. 177, pp. 261–269, Feb. 2018, doi: 10.1016/j.ces.2017.11.039.

[112] R. Liu, X. Chen, and X. Wang, "Effects of thermocapillarity on the dynamics of an exterior coating flow of a self-rewetting fluid," *International Journal of Heat and Mass Transfer*, vol. 136, pp. 692–701, Jun. 2019, doi: 10.1016/j.ijheatmasstransfer.2019.03.049.

[113] L. Dong, X. Li, and R. Liu, "Effect of Thermocapillary on Absolute and Convective Instability of Film Flow of Self-Rewetting Fluid," *Microgravity Sci. Technol.*, vol. 32, no. 3, pp. 415–422, Jun.

2020, doi: 10.1007/s12217-019-09778-8.

[114] W. Batson, Y. Agnon, and A. Oron, “Thermocapillary modulation of self-rewetting films,” *Journal of Fluid Mechanics*, vol. 819, pp. 562–591, May 2017, doi: 10.1017/jfm.2017.191.

[115] Z. Ding, Z. Liu, R. Liu, and C. Yang, “Breakup of ultra-thin liquid films on vertical fiber enhanced by Marangoni effect,” *Chemical Engineering Science*, vol. 199, pp. 342–348, May 2019, doi: 10.1016/j.ces.2018.12.058.

[116] H. Ji and T. P. Witelski, “Finite-time thin film rupture driven by modified evaporative loss,” *Physica D: Nonlinear Phenomena*, vol. 342, pp. 1–15, Mar. 2017, doi: 10.1016/j.physd.2016.10.002.

[117] R. I. Issa, A. D. Gosman, and A. P. Watkins, “The computation of compressible and incompressible recirculating flows by a non-iterative implicit scheme,” *Journal of Computational Physics*, vol. 62, no. 1, pp. 66–82, Jan. 1986, doi: 10.1016/0021-9991(86)90100-2.

[118] S. Whitaker, “Forced convection heat transfer correlations for flow in pipes, past flat plates, single cylinders, single spheres, and for flow in packed beds and tube bundles.,” *AIChE Journal*, vol. 18, pp. 361–371, 1972.

[119] A. F. Mills, *Basic Heat and Mass Transfer*. Prentice Hall, 1999.

[120] E. W. Washburn, “The Dynamics of Capillary Flow,” *Phys. Rev.*, vol. 17, no. 3, pp. 273–283, Mar. 1921, doi: 10.1103/PhysRev.17.273.

[121] “Silicone fluid dm-fluid performance test results, Shin-Etsu Silicone.”

[122] P. G. de Gennes, “Wetting: statics and dynamics,” *Rev. Mod. Phys.*, vol. 57, no. 3, pp. 827–863, Jul. 1985, doi: 10.1103/RevModPhys.57.827.

[123] B. Scheid, N. Kofman, and W. Rohlfs, “Critical inclination for absolute/convective instability transition in inverted falling films,” *Physics of Fluids*, vol. 28, no. 4, p. 044107, Apr. 2016, doi: 10.1063/1.4946827.

[124] D. Quéré, “Thin Films Flowing on Vertical Fibers,” *EPL*, vol. 13, no. 8, p. 721, Dec. 1990, doi: 10.1209/0295-5075/13/8/009.

[125] J. D. Berry, M. J. Neeson, R. R. Dagastine, D. Y. C. Chan, and R. F. Tabor, “Measurement of surface and interfacial tension using pendant drop tensiometry,” *Journal of Colloid and Interface Science*, vol. 454, pp. 226–237, Sep. 2015, doi: 10.1016/j.jcis.2015.05.012.

[126] F. A. Morrison, *An Introduction to Fluid Mechanics*. Cambridge University Press, 2013.

[127] J. Pantelic, E. Teitelbaum, M. Bozlar, S. Kim, and F. Meggers, “Development of moisture absorber based on hydrophilic nonporous membrane mass exchanger and alkoxylated siloxane liquid desiccant,” *Energy and Buildings*, vol. 160, pp. 34–43, Feb. 2018, doi: 10.1016/j.enbuild.2017.10.093.

[128] R. Kumar and A. K. Asati, “Experimental study on performance of celdek packed liquid desiccant dehumidifier,” *Heat Mass Transfer*, vol. 52, no. 9, pp. 1821–1832, Sep. 2016, doi: 10.1007/s00231-015-1704-2.

[129] M. Ijas ahmed and L. Gangadhara kiran kumar, “Dehumidification performance of liquid desiccant system with aqueous-CaCl2 solution in a humid climatic condition,” *Materials Today: Proceedings*, vol. 46, pp. 9977–9982, Jan. 2021, doi: 10.1016/j.matpr.2021.03.398.

[130] B. K. Naik and P. Muthukumar, “Experimental investigation and parametric studies on structured packing chamber based liquid desiccant dehumidification and regeneration systems,” *Building and Environment*, vol. 149, pp. 330–348, Feb. 2019, doi: 10.1016/j.buildenv.2018.12.028.

[131] S. Bouzenada, A. N. Kaabi, L. Frainkin, T. Salmon, and A. Léonard, “Experimental Comparative Study on Lithium Chloride and Calcium Chloride Desiccants,” *Procedia Computer Science*, vol. 83, pp. 718–725, Jan. 2016, doi: 10.1016/j.procs.2016.04.159.

[132] F. J. Solorio and M. Sen, “Linear stability of a cylindrical falling film,” *Journal of Fluid Mechanics*, vol. 183, pp. 365–377, Oct. 1987, doi: 10.1017/S0022112087002672.

[133] M. J. Miksis and S. H. Davis, “Slip over rough and coated surfaces,” *Journal of Fluid Mechanics*, vol. 273, pp. 125–139, Aug. 1994, doi: 10.1017/S0022112094001874.

[134] A. D. Khawaji, I. K. Kutubkhanah, and J.-M. Wie, “Advances in seawater desalination technologies,” *Desalination*, vol. 221, no. 1, pp. 47–69, Mar. 2008, doi:

10.1016/j.desal.2007.01.067.

[135] I. S. Al-Mutaz, “A comparative study of RO and MSF desalination plants,” *Desalination*, vol. 106, no. 1, pp. 99–106, Aug. 1996, doi: 10.1016/S0011-9164(96)00097-5.

[136] M. Nair and D. Kumar, “Water desalination and challenges: The Middle East perspective: a review,” *Desalination and Water Treatment*, vol. 51, no. 10–12, pp. 2030–2040, Feb. 2013, doi: 10.1080/19443994.2013.734483.

[137] M. W. Shahzad, M. Burhan, L. Ang, and K. C. Ng, “Energy-water-environment nexus underpinning future desalination sustainability,” *Desalination*, vol. 413, pp. 52–64, Jul. 2017, doi: 10.1016/j.desal.2017.03.009.

[138] B. Milow and E. Zarza, “Advanced MED solar desalination plants. Configurations, costs, future — seven years of experience at the Plataforma Solar de Almeria (Spain),” *Desalination*, vol. 108, no. 1, pp. 51–58, Feb. 1997, doi: 10.1016/S0011-9164(97)00008-8.

[139] S. Al-Hallaj, M. M. Farid, and A. Rahman Tamimi, “Solar desalination with a humidification-dehumidification cycle: performance of the unit,” *Desalination*, vol. 120, no. 3, pp. 273–280, Dec. 1998, doi: 10.1016/S0011-9164(98)00224-0.

[140] M. H. Hamed, A. E. Kabeel, Z. M. Omara, and S. W. Sharshir, “Mathematical and experimental investigation of a solar humidification–dehumidification desalination unit,” *Desalination*, vol. 358, pp. 9–17, Feb. 2015, doi: 10.1016/j.desal.2014.12.005.

[141] A. S. A. Mohamed, M. S. Ahmed, and Abanob. G. Shahdy, “Theoretical and experimental study of a seawater desalination system based on humidification-dehumidification technique,” *Renewable Energy*, vol. 152, pp. 823–834, Jun. 2020, doi: 10.1016/j.renene.2020.01.116.

[142] G. Prakash Narayan, M. G. St. John, S. M. Zubair, and J. H. Lienhard V, “Thermal design of the humidification dehumidification desalination system: An experimental investigation,” *International Journal of Heat and Mass Transfer*, vol. 58, no. 1–2, pp. 740–748, Mar. 2013, doi: 10.1016/j.ijheatmasstransfer.2012.11.035.

[143] M. I. Zubair, F. A. Al-Sulaiman, M. A. Antar, S. A. Al-Dini, and N. I. Ibrahim, “Performance and

cost assessment of solar driven humidification dehumidification desalination system," *Energy Conversion and Management*, vol. 132, pp. 28–39, Jan. 2017, doi: 10.1016/j.enconman.2016.10.005.

[144] M. H. Sharqawy, M. A. Antar, S. M. Zubair, and A. M. Elbashir, "Optimum thermal design of humidification dehumidification desalination systems," *Desalination*, vol. 349, pp. 10–21, Sep. 2014, doi: 10.1016/j.desal.2014.06.016.

[145] H. Müller-Holst, "Mehrfacheffekt-Feuchtluftdestillation bei Umgebungsdruck," Technische Universität München, 2002. Accessed: Nov. 25, 2021. [Online]. Available: https://mediatum.ub.tum.de/601861

[146] H. Muller-Holst, "Solar thermal desalination using the multiple effect humidification (MEH)-method," in *Solar Desalination for the 21st Century*, Dordrecht, 2007, pp. 215–225. doi: 10.1007/978-1-4020-5508-9_16.

[147] K. Garg, S. K. Das, and H. Tyagi, "Thermal design of a humidification-dehumidification desalination cycle consisting of packed-bed humidifier and finned-tube dehumidifier," *International Journal of Heat and Mass Transfer*, vol. 183, p. 122153, Feb. 2022, doi: 10.1016/j.ijheatmasstransfer.2021.122153.

[148] Y. Zhang, C. Zhu, H. Zhang, W. Zheng, S. You, and Y. Zhen, "Experimental study of a humidification-dehumidification desalination system with heat pump unit," *Desalination*, vol. 442, pp. 108–117, Sep. 2018, doi: 10.1016/j.desal.2018.05.020.

[149] Z. Wang *et al.*, "Pathways and challenges for efficient solar-thermal desalination," *Science Advances*, vol. 5, no. 7, p. eaax0763, Jul. 2019, doi: 10.1126/sciadv.aax0763.

[150] S. A. Ashrafizadeh and M. Amidpour, "Exergy analysis of humidification–dehumidification desalination systems using driving forces concept," *Desalination*, vol. 285, pp. 108–116, Jan. 2012, doi: 10.1016/j.desal.2011.09.041.

[151] E. Z. Mahdizade and M. Ameri, "Thermodynamic investigation of a semi-open air, humidification dehumidification desalination system using air and water heaters," *Desalination*, vol. 428, pp.

182–198, Feb. 2018, doi: 10.1016/j.desal.2017.11.032.

[152] S. Mohammadzade Negharchi, A. Najafi, A. Abbas Nejad, and N. Ghadimi, “Determination of the optimal model for solar humidification dehumidification desalination cycle with extraction and injection,” *Desalination*, vol. 506, p. 114984, Jun. 2021, doi: 10.1016/j.desal.2021.114984.

[153] S. M. Elmutasim, M. A. Ahmed, M. A. Antar, P. Gandhidasan, and S. M. Zubair, “Design strategies of conventional and modified closed-air open-water humidification dehumidification systems,” *Desalination*, vol. 435, pp. 114–127, Jun. 2018, doi: 10.1016/j.desal.2017.11.011.

[154] H. Müller-Holst, M. Engelhardt, and W. Schölkopf, “Small-scale thermal seawater desalination simulation and optimization of system design,” *Desalination*, vol. 122, no. 2, pp. 255–262, Jul. 1999, doi: 10.1016/S0011-9164(99)00046-6.

[155] G. Wu, H. Zheng, H. Kang, Y. Yang, P. Cheng, and Z. Chang, “Experimental investigation of a multi-effect isothermal heat with tandem solar desalination system based on humidification–dehumidification processes,” *Desalination*, vol. 378, pp. 100–107, Jan. 2016, doi: 10.1016/j.desal.2015.09.024.

[156] G. Wu, H. Zheng, X. Ma, C. Kutlu, and Y. Su, “Experimental investigation of a multi-stage humidification-dehumidification desalination system heated directly by a cylindrical Fresnel lens solar concentrator,” *Energy Conversion and Management*, vol. 143, pp. 241–251, Jul. 2017, doi: 10.1016/j.enconman.2017.04.011.

[157] Z. Rahimi-Ahar, M. S. Hatamipour, and Y. Ghalavand, “Experimental investigation of a solar vacuum humidification-dehumidification (VHDH) desalination system,” *Desalination*, vol. 437, pp. 73–80, Jul. 2018, doi: 10.1016/j.desal.2018.03.002.

[158] R. H. Xiong, S. C. Wang, L. X. Xie, Z. Wang, and P. L. Li, “Experimental investigation of a baffled shell and tube desalination column using the humidification-dehumidification process,” *Desalination*, vol. 180, no. 1, pp. 253–261, Aug. 2005, doi: 10.1016/j.desal.2005.01.007.

[159] M. Sievers and J. H. L. V, “Design of Flat-Plate Dehumidifiers for Humidification–Dehumidification Desalination Systems,” *Heat Transfer Engineering*, vol. 34, no. 7, pp. 543–561,

Jan. 2013, doi: 10.1080/01457632.2013.730355.

[160] J. F. Klausner, Y. Li, and R. Mei, “Evaporative heat and mass transfer for the diffusion driven desalination process,” *Heat Mass Transfer*, vol. 42, no. 6, p. 528, May 2005, doi: 10.1007/s00231-005-0649-2.

[161] W. F. He, L. Huang, J. R. Xia, W. P. Zhu, D. Han, and Y. K. Wu, “Parametric analysis of a humidification dehumidification desalination system using a direct-contact dehumidifier,” *International Journal of Thermal Sciences*, vol. 120, pp. 31–40, Oct. 2017, doi: 10.1016/j.ijthermalsci.2017.05.027.

[162] Z. Xu *et al.*, “Ultrahigh-efficiency desalination via a thermally-localized multistage solar still,” *Energy & Environmental Science*, vol. 13, no. 3, pp. 830–839, 2020, doi: 10.1039/C9EE04122B.

[163] Z. Zeng, A. Sadeghpour, and Y. S. Ju, “A highly effective multi-string humidifier with a low gas stream pressure drop for desalination,” *Desalination*, vol. 449, pp. 92–100, 2019.

[164] G. P. Narayan, M. H. Sharqawy, S. Lam, S. K. Das, and J. H. Lienhard, “Bubble columns for condensation at high concentrations of noncondensable gas: Heat-transfer model and experiments,” *AIChE J*, vol. 59, no. 5, pp. 1780–1790, May 2013, doi: 10.1002/aic.13944.

[165] T. Rajaseenivasan, R. K. Shanmugam, V. M. Hareesh, and K. Srithar, “Combined probation of bubble column humidification dehumidification desalination system using solar collectors,” *Energy*, vol. 116, pp. 459–469, Dec. 2016, doi: 10.1016/j.energy.2016.09.127.

[166] S. A. El-Agouz, “A new process of desalination by air passing through seawater based on humidification–dehumidification process,” *Energy*, vol. 35, no. 12, pp. 5108–5114, Dec. 2010, doi: 10.1016/j.energy.2010.08.005.

[167] A. Khalil, S. A. El-Agouz, Y. A. F. El-Samadony, and A. Abdo, “Solar water desalination using an air bubble column humidifier,” *Desalination*, vol. 372, pp. 7–16, Sep. 2015, doi: 10.1016/j.desal.2015.06.010.

[168] K. Hattori, M. Ishikawa, and Y. H. Mori, “Strings of liquid beads for gas-liquid contact operations,” *AIChE J.*, vol. 40, no. 12, pp. 1983–1992, 1994, doi: 10.1002/aic.690401209.

[169] H. Chinju, K. Uchiyama, and Y. H. Mori, "'String-of-beads' flow of liquids on vertical wires for gas absorption," *AIChE journal*, vol. 46, no. 5, pp. 937–945, 2000.

[170] K. Uchiyama, H. Migita, R. Ohmura, and Y. H. Mori, "Gas absorption into 'string-of-beads' liquid flow with chemical reaction: application to carbon dioxide separation," *International Journal of Heat and Mass Transfer*, vol. 46, no. 3, pp. 457–468, Jan. 2003, doi: 10.1016/S0017-9310(02)00301-0.

[171] H. Migita, K. Soga, and Y. H. Mori, "Gas absorption in a wetted-wire column," *AIChE J.*, vol. 51, no. 8, pp. 2190–2198, Aug. 2005, doi: 10.1002/aic.10483.

[172] S. G. Pakdehi and S. Taheri, "Separation of Hydrazine from Air by Wetted Wire Column," *Chem. Eng. Technol.*, vol. 33, no. 10, pp. 1687–1694, Oct. 2010, doi: 10.1002/ceat.201000070.

[173] S. M. Hosseini, R. Alizadeh, E. Fatehifar, and A. Alizadehdakhel, "Simulation of gas absorption into string-of-beads liquid flow with chemical reaction," *Heat Mass Transfer*, vol. 50, no. 10, pp. 1393–1403, Apr. 2014, doi: 10.1007/s00231-014-1343-z.

[174] S. A. Galledari, R. Alizadeh, E. Fatehifar, and E. Soroush, "Simulation of carbon dioxide absorption by monoethanolamine solution in wetted-wire column," *Chemical Engineering and Processing: Process Intensification*, vol. 102, pp. 59–69, 2016.

[175] R. A. Seban and A. Faghri, "Evaporation and heating with turbulent falling liquid films," *Journal of Heat Transfer*, vol. 98, no. 2, pp. 315–318, 1976.

[176] J. A. Shmerler and I. Mudawwar, "Local heat transfer coefficient in wavy free-falling turbulent liquid films undergoing uniform sensible heating," *International journal of heat and mass transfer*, vol. 31, no. 1, pp. 67–77, 1988.

[177] S.-M. Yih and J.-L. Liu, "Prediction of heat transfer in turbulent falling liquid films with or without interfacial shear," *AIChE journal*, vol. 29, no. 6, pp. 903–909, 1983.

[178] J. A. Shmerler and I. Mudawwar, "Local evaporative heat transfer coefficient in turbulent free-falling liquid films," *International journal of heat and mass transfer*, vol. 31, no. 4, pp. 731–742, 1988.

[179] E. M. Sparrow and A. L. Loeffler, “Longitudinal laminar flow between cylinders arranged in regular array,” *AIChE Journal*, vol. 5, no. 3, pp. 325–330, 1959, doi: 10.1002/aic.690050315.

[180] G. Prakash Narayan, J. H. Lienhard, and S. M. Zubair, “Entropy generation minimization of combined heat and mass transfer devices,” *International Journal of Thermal Sciences*, vol. 49, no. 10, pp. 2057–2066, Oct. 2010, doi: 10.1016/j.ijthermalsci.2010.04.024.

[181] G. P. Narayan, K. M. Chehayeb, R. K. McGovern, G. P. Thiel, and S. M. Zubair, “Thermodynamic balancing of the humidification dehumidification desalination system by mass extraction and injection,” *International Journal of Heat and Mass Transfer*, vol. 57, no. 2, pp. 756–770, 2013.

[182] K. H. Mistry, J. H. Lienhard, and S. M. Zubair, “Effect of entropy generation on the performance of humidification-dehumidification desalination cycles,” *International Journal of Thermal Sciences*, vol. 49, no. 9, pp. 1837–1847, Sep. 2010, doi: 10.1016/j.ijthermalsci.2010.05.002.

[183] G. P. Narayan, M. H. Sharqawy, J. H. Lienhard V, and S. M. Zubair, “Thermodynamic analysis of humidification dehumidification desalination cycles,” *Desalination and Water Treatment*, vol. 16, no. 1–3, pp. 339–353, Apr. 2010, doi: 10.5004/dwt.2010.1078.

[184] G. Yuan, Z. Wang, H. Li, and X. Li, “Experimental study of a solar desalination system based on humidification–dehumidification process,” *Desalination*, vol. 277, no. 1, pp. 92–98, Aug. 2011, doi: 10.1016/j.desal.2011.04.002.

[185] A. Ruiz-Aguirre, J. A. Andrés-Mañas, J. M. Fernández-Sevilla, and G. Zaragoza, “Modeling and optimization of a commercial permeate gap spiral wound membrane distillation module for seawater desalination,” *Desalination*, vol. 419, pp. 160–168, Oct. 2017, doi: 10.1016/j.desal.2017.06.019.

[186] K. Zhao *et al.*, “Experimental study of the memsys vacuum-multi-effect-membrane-distillation (V-MEMD) module,” *Desalination*, vol. 323, pp. 150–160, Aug. 2013, doi: 10.1016/j.desal.2012.12.003.